Galaxy evolution in extreme environments, The impact of cluster mergers.

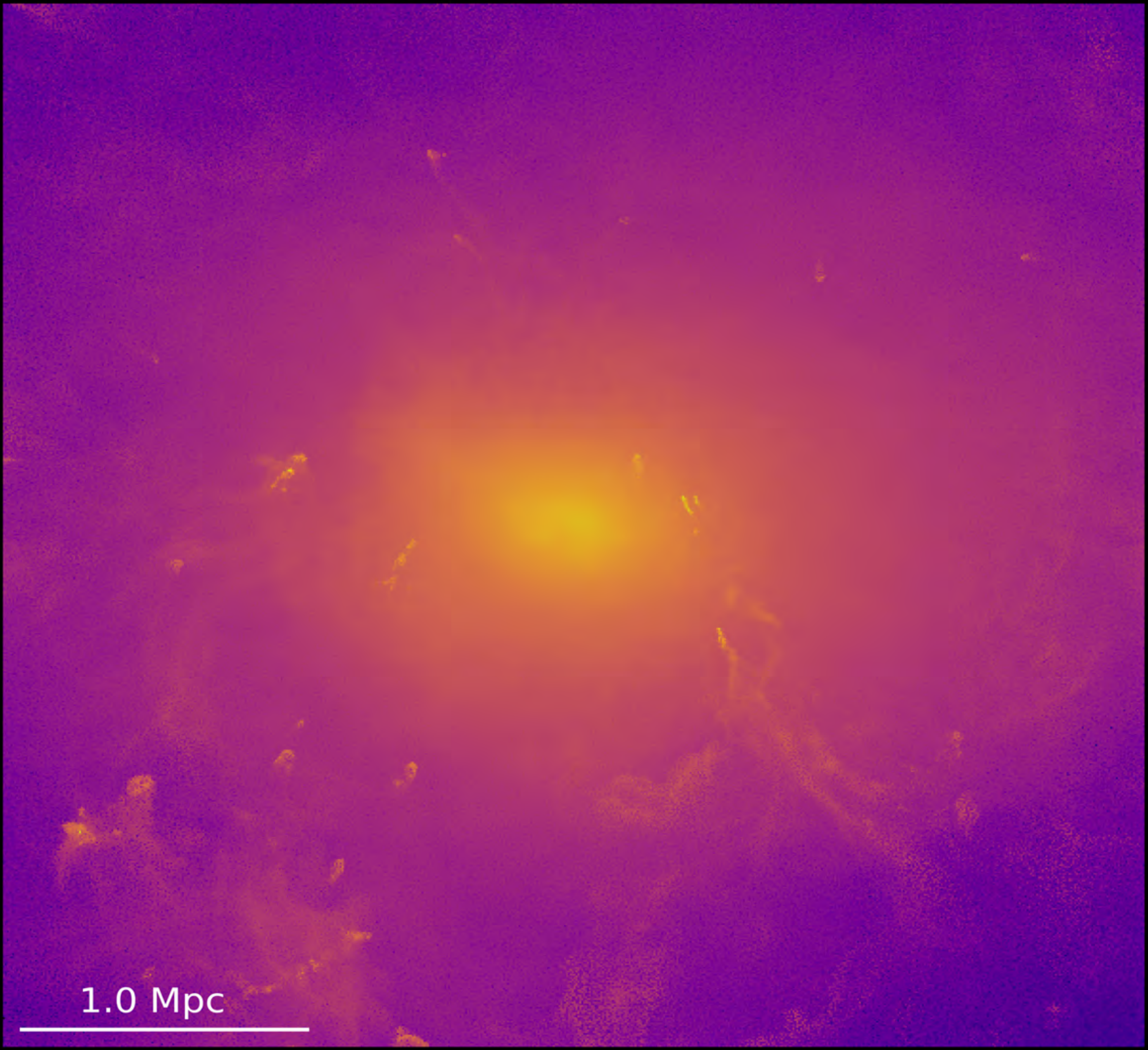

Franklin Aldás

Galaxy evolution in extreme environments, The impact of cluster mergers

Franklin Aldás

UNIVERSIDAD
DE LA SERENA
CHILE

Doctoral Thesis

To fulfil the requirements for the degree of Doctorate in Astronomy
at Universidad de La Serena by

Franklin Aldás

under the supervision of
Prof. Facundo Ariel Gómez, Universidad de La Serena,
and co-supervison of: Dr. Cristian Vega-Martínez, Universidad Central de Chile.

Defended on October 1st, 2024 before a committee composed of

Dr. Ricardo Demarco, Universidad de Concepción.
Dr. Alexandro Saro, University of Trieste, at the Observatory of Trieste.
Dr. Nelson David Padilla, Universidad Nacional de Córdoba.
Dr. Paulo Afrânio Lopes, Universidade Federal do Rio de Janeiro.

November, 2024.

Contents

Chapter 1

Introduction

1.1 Galaxy clusters

Galaxy clusters are the largest gravitationally bound structures in the Universe, containing hundreds or thousands of galaxies within their deep gravitational potential wells (Voit, 2005; Abell, 1958; Sarazin, 1986). The first evidence for the existence of galaxy clusters emerged in the 1930s, primarily through the work of Zwicky. While studying what was thought to be a ”nebula” (but was actually the Coma cluster), Zwicky used the virial theorem to estimate its mass from the velocities of its galaxies. He found that the estimated mass was 400 times greater than the total mass of the observable stars (Zwicky, 1933, 1937). This significant discrepancy led Zwicky to propose the existence of dark matter, an unseen substance that provides the additional gravitational force needed to account for the observed cluster structure. This discovery also marked the first evidence of galaxy clusters as massive, gravitationally bound systems composed of numerous galaxies. Later, the detection of the X-ray emission originated in the intracluster medium (ICM), which is a very hot plasma that fills the space between galaxies and emits through thermal Bremsstrahlung, gave us a deeper understanding of galaxy clusters (Sarazin, 1986). The observed properties of the intracluster medium (ICM) support the existence of dark matter. To maintain the gas gravitationally bound within the cluster at such high temperatures, the cluster must possess a significantly greater mass than what is visible. The first observation of X-ray emission from the ICM was made in the Coma cluster by Cavaliere et al. (1971), and Forman et al. (1972). Another valuable tool for studying and detecting galaxy clusters is the Sunyaev-Zel'dovich effect. This effect, which involves the distortion of the cosmic microwave background (CMB) by the scattering of photons as they pass through the ICM, has been used to discover and study new galaxy clusters across various redshifts (Sunyaev & Zeldovich, 1972; Carlstrom et al., 2002). As a result, galaxy clusters help us to understand the large-scale structure of the Universe, the distribution of dark matter, and the processes that drive galaxy formation and evolution. Observations across optical, X-ray, and microwave wavelengths offer a panchromatic view of their composition, dynamics, and their role in the cosmic web (Voit, 2005).

The formation of structures such as groups and clusters is understood within the framework of the Λ-CDM model, which proposes that the Universe began approximately 13.7 billion years ago, initially existing in an extremely hot and dense state with a uniform distribution of particles (Planck Collaboration, 2016, 2020). Then, this hot, dense plasma cooled over time, leading to the formation of light chemical elements and setting the stage for the formation of stars, galaxies, and galaxy groups and clusters. To explain the initial conditions of the Big Bang, it is necessary to introduce the theory of inflation, which suggests that a region of matter with negative pressure caused a gravitational repulsion, triggering an exponential expansion that lasted around 10^{-35} seconds. This expansion solved several problems in the standard Big Bang model, such as the horizon problem (explaining why distant regions of the Universe have the same temperature), the flatness problem (why the Universe appears geometrically flat), and the monopole problem (why we don't observe magnetic monopoles). Additionally, inflation stretched tiny quantum fluctuations to cosmic scales, seeding the formation of galaxies and large-scale structures. As inflation ended, the inflaton field decayed, releasing vast amounts of energy that heated the Universe and created a dense, hot ”primordial soup” of particles (Guth, 1981; Linde, 1982; Albrecht & Steinhardt, 1982). The inflationary model accurately predicted the power spectrum of temperature anisotropies in the CMB, a relic radiation from the early Universe first detected by Penzias & Wilson (1965). Recent measurements estimate the CMB temperature at $T = 2.725 \pm 0.001K$, with fluctuations of about

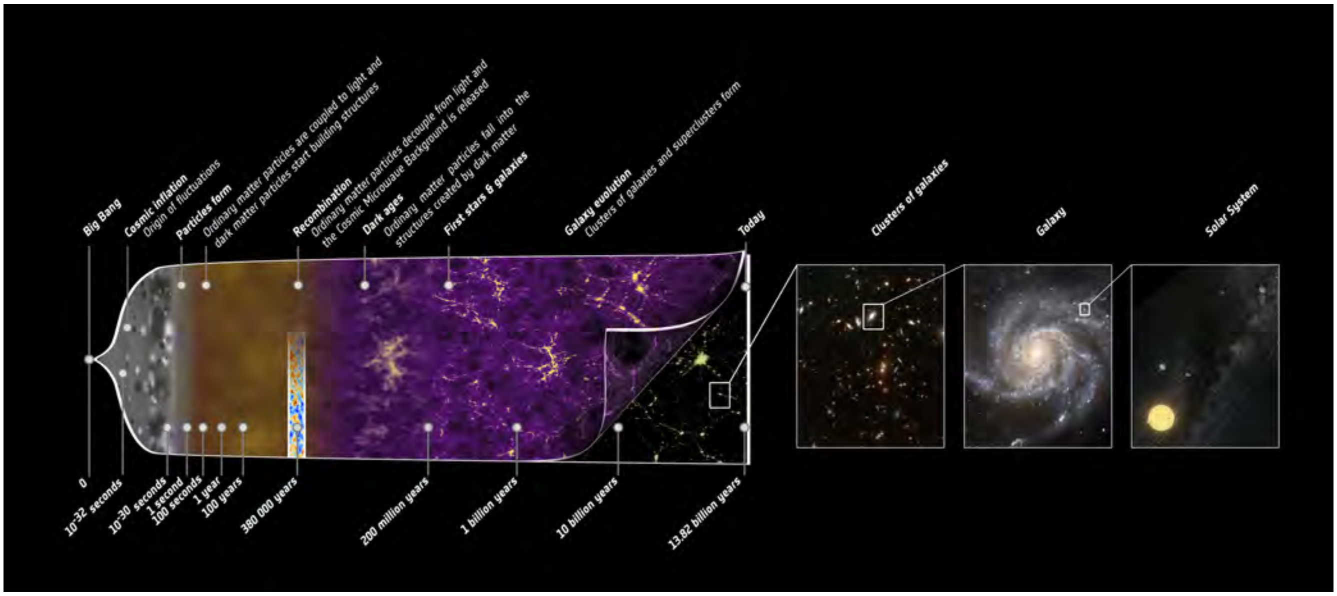

Figure 1.1.1: Timeline of the evolution of the Universe, highlighting key events from its early stages characterised by an almost uniform state with only small fluctuations. Driven by gravitational forces, these fluctuations eventually gave rise to the diverse cosmic structures we observe today, including stars and galaxies. Credits: ESA – C. Carreau

10^{-5} K, believed to be the result of quantum fluctuations during inflation. Figure 1.1.1 presents an illustration of the history of the Universe, tracing its evolution from an early phase of near uniformity to the formation of galaxy clusters and smaller structures observed today.

Within this context, the hierarchical model of structure formation proposes that the earliest structures formed are small dark matter haloes, which grow into larger systems through hierarchical mergers. Cold dark matter (CDM) can collapse more rapidly than baryonic matter due to the nature of its interactions. Unlike baryonic matter, which interacts with radiation and is influenced by electromagnetic forces, CDM only interacts through gravity. This allows it to decouple from the expansion and begin collapsing into gravitational wells much earlier. (Press & Schechter, 1974; Blumenthal et al., 1984). Baryons, present in lower proportions, evolve following the DM halos. Gas cools and collapses at the centres of the haloes, forming stars and giving rise to the observable galaxies. When haloes merge, the galaxies they contain start orbiting in the new common potential well, thus mutually interacting before they merge, originating larger structures such as galaxy groups and clusters (White & Rees, 1978; Springel, 2005). Early theoretical models demonstrated that such processes could form clusters like the Coma cluster (van Albada, 1961; Peebles & Yu, 1970). The hot gas observed in clusters is believed to result from gas heated by accretion shocks as it falls into the cluster (Gunn & Gott, 1972; Sunyaev & Zeldovich, 1972).

1.2 Standard Cosmological Model Λ-CDM

The standard cosmological model is based on the Cosmological Principle, which states that the Universe is statistically isotropic and homogeneous on sufficiently large scales, and it also assumes that General Relativity can describe the dynamics of the evolution of the Universe's geometry. Isotropy implies that there are no preferred directions in the Universe, while homogeneity means that the Universe is uniform in composition and structure at every location. In most cases, isotropy implies homogeneity, except if the observer were located at a special point, such as the centre of the Universe. Therefore, if the Universe is isotropic to all observers, it must also be homogeneous to all observers.

As shown in Weinberg (1972), and Rindler (1977), the Friedmann-Lemaître-Robertson-Walker (FLRW) metric is the most general metric that satisfies the cosmological principle. This metric uses comoving spherical coordinates (r, θ, ϕ), representing a system that expands with the universe. The FLWR metric is given by:

$$ds^2 = -c^2dt^2 + a^2(t)\left[\frac{dr^2}{1-kr^2} + r^2d\theta^2 + r^2sin^2\theta d\phi^2\right]$$

Where t is the cosmic time coordinate, $a(t)$ is the dimensionless time-dependent parameter scale factor representing the rate of expansion of the Universe, and k is the curvature parameter which determines the geometry of space: $k = 0$ for a flat universe, $k = +1$ for a closed universe with positive curvature, and $k = -1$ for an open universe with negative curvature.

Solving the Einstein equations for the FLRW metric and assuming that the Universe can be described as an ideal fluid, we obtain the Friedman equations given by:

$$\left(\frac{\dot{a}}{a}\right)^2 = \frac{8\pi G\rho}{3} + \frac{\Lambda}{3} - \frac{kc^2}{a^2} \tag{1.2.1}$$

and

$$\frac{\ddot{a}}{a} = -\frac{4\pi G}{3}(\rho + \frac{3p}{c^2}) + \frac{\Lambda}{3} \tag{1.2.2}$$

Here, G is the gravitational constant, ρ is the total energy density of the universe, including contributions from matter, and radiation, p is the pressure associated with the energy density ρ, and Λ is the cosmological constant, which accounts for dark energy and contributes to the accelerated expansion of the universe. The first Friedmann equation shows how the Hubble parameter, defined as $H(t) = \dot{a}/a$, depends on the total energy density and curvature of the Universe. If ρ is high, the expansion rate is faster; if ρ is low, the expansion rate is slower. The second Friedmann equation indicates whether the universe's expansion is accelerating or decelerating.

From equation (1.2.1), we can have the critical energy density (ρ_c) as the value of ρ at which the curvature k vanishes, and it is given by:

$$\rho_c = \frac{3H^2}{8\pi G} \tag{1.2.3}$$

A universe with a density higher than ρ_c will be spacially closed, and a universe with a density lower than ρ_c is spacially open. From the definition of the critical density, we can define some useful cosmological parameters such as the total matter density Ω_m, the baryon density Ω_b, the cosmological constant Ω_Λ, and the curvature constant Ω_k, defined as:

$$\Omega_b = \frac{\rho_b}{\rho_c}, \quad \Omega_m = \frac{\rho_m}{\rho_c}, \quad \Omega_\Lambda = \frac{\Lambda}{3H_0^2}, \quad \Omega_k = -\frac{kc^2}{a_0^2H_0^2}.$$

Where, ρ_m is the total mass content that includes dark and baryonic matter, while ρ_b only includes baryonic matter. H_0 and a_0 are the values of the Hubble parameter and scale factor measured at present time, i.e. at redshift $z = 0$. This theoretical framework is based on the three observational pillars of modern cosmology that are the evidence of the predictions from the Big Bang theory; these observations are the cosmic expansion, the observation of the Cosmic Microwave Radiation (CMB), and the Big Bang nucleosynthesis.

The discovery of cosmic expansion is one of the most significant findings in modern cosmology. In 1929, Edwin Hubble established a linear relationship between the redshift of distant galaxies and their distances, demonstrating that more distant galaxies recede faster than nearby ones (Hubble, 1929). This relationship relates the Hubble constant, H_0, which corresponds to the Hubble parameter at the present time, expressed mathematically as $H_0 = v/d$, where v is the velocity of the radial recession and d is the distance from us. This relationship provides evidence that the Universe is expanding (Hubble, 1929). The first estimation of the Hubble constant revealed a value of 530 km s^{-1} Mpc $^{-1}$ Hubble (1929), but modern studies such as the study of Cepheids and Supernovae Type Ia and Type II using the Hubble Space Telescope data give an estimate value for H_0 equal to 72 ± 8 km s^{-1} Mpc $^{-1}$ (Freedman et al., 2001), and 74.03 ± 1.82 (Riess et al., 2019).

The second observational pillar of modern cosmology is the observations of the CMB. Theoretical predictions of the CMB were made by Alpher and Herman in 1948, who estimated the temperature to be approximately 5 K, refining earlier work by Gamow (Alpher & Herman, 1948; Gamow, 1948). Dicke in 1946 had initially constrained the CMB temperature to be below 20 K based on radiometer measurements (Dicke, 1946). Penzias and Wilson achieved the first direct detection of CMB in 1965. They observed an excess in the noise temperature of their antenna, approximately 3.5 K higher than expected (Penzias & Wilson, 1965). This observation was later interpreted by Dicke et al. as evidence of the CMB, consistent with the theoretical expectations of a primordial radiation field (Dicke et al., 1965). Subsequent measurements have determined that the CMB

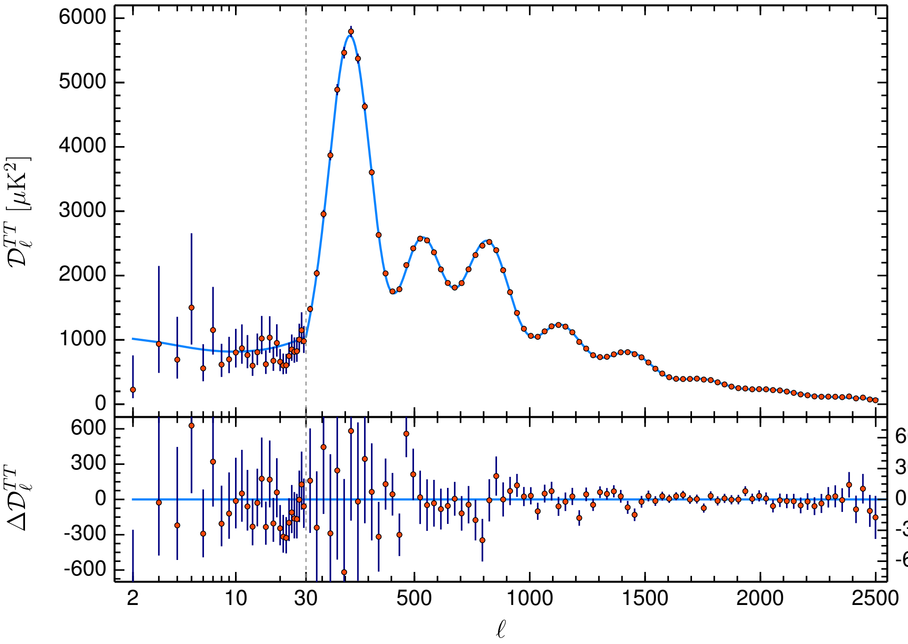

Figure 1.2.1: Top panel shows the power spectrum of the temperature anisotropies in the CMB. The vertical axis represents the power D_l^{TT}, measured in units of micro-Kelvin squared (μK^2), while the horizontal axis corresponds to the multipole moment l. The solid line represents the best-fit Λ-CDM model predictions. In the bottom panel, we have the residuals between the model and the measured power spectrum. Figure taken from Planck Collaboration (2020)

temperature is $T = 2.725 \pm 0.001$ K, and it has been confirmed that the radiation follows a black-body spectrum (Fixsen, 2009). Figure 1.2.1, taken from Planck Collaboration (2020), shows the power spectrum of the temperature anisotropies in the CMB including the observational error bars. The vertical axis represents the power D_l^{TT}, measured in units of micro-Kelvin squared (μK^2), while the horizontal axis corresponds to the multipole moment l, which is inversely related to the angular scale of the fluctuations. Higher values of l correspond to smaller angular scales. In solid line, the predicted power spectrum of best-fit Λ-CDM cosmology, which follows quite well with the CMB data. The CMB anisotropies allow us to derive values for the most important cosmological parameters that define and allow us to constrain the geometry of our Universe. The latest values for the cosmological parameters estimated by CMB observations are $H_0 = 67.66$ km s^{-1}, $\Omega_\Lambda = 0.689$ $\Omega_m = 0.31$, $\Omega_b = 0.048$, and $\Omega_k = 0.0007$, showing that the universe is spatially flat, and predominantly composed by dark energy and dark matter, with baryonic matter accounting less than 5% of the total matter-energy content of the Universe (Planck Collaboration, 2020).

The last observational pillar of modern cosmology is the Big Bang Nucleosynthesis (BBN). It refers to the process by which light elements were formed in the early Universe when it was hot and dense. Initially, the temperature was so high, around a few MeV, that nuclei could not form because high-energy photons would destroy any nuclei produced in the radiation-dominated environment. As the Universe cooled below the binding energies of different nuclei, light elements began to form. Theoretical calculations of primordial abundances, based on the conditions of the early Universe and relevant nuclear cross sections, predict the abundance of these light elements. Observations of light element abundances are consistent with these predictions, which supports the Big Bang model, except for the lithium abundance, a topic that remains not fully understood (Alpher et al., 1948; Steigman, 2007; Fields, 2011).

1.3 Formation and evolution of galaxy clusters

As mentioned previously, the hierarchical model, combined with the cold dark matter (CDM) cosmological paradigm, provides a robust framework for interpreting the multi-wavelength observations of clusters. In this scenario, all galaxies, particularly clusters, form through a series of mergers and accretions of smaller systems, a process that continues even in the present

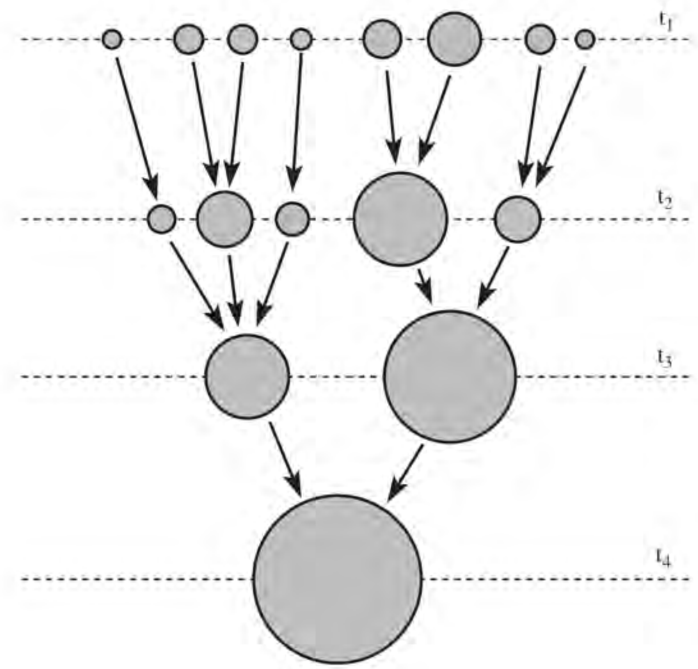

Figure 1.3.1: Scheme of hierarchical formation of the structures in the Universe. Small structures are accreted by larger ones to form galaxy groups and clusters. We can also see that galaxies can follow different paths to their final host; for example, galaxies on the left first fall into a group and then the group itself fall into the final structure, while the galaxy on the right falls straight from the field to the cluster. Figure taken from Mo et al. (2010)

epoch. The CDM drives the formation of structures because baryonic matter is initially prevented from collapsing due to its coupling with radiation in the early universe. Only after recombination, when the universe cools enough for neutral atoms to form, can baryonic matter fall into the gravitational wells (Press & Schechter, 1974; Blumenthal et al., 1984). This merging history can be tracked in cosmological simulations and stored in the form of merger trees. Figure 1.3.1, taken from Mo et al. (2010), presents a schematic merger tree depicting the merger history of a dark matter halo. It highlights progenitor halos at three distinct epochs following different merger paths to form a single halo by time t_4.

During the early stages of the evolution of the Universe, when density fluctuations are still small and gravitational interactions are weak enough, the growth of those fluctuations can be described by linear perturbation theory. However, when the fluctuations are large enough, the nonlinear effect becomes significant, leading to the collapse of overdense regions and the formation of bound structures like galaxies and clusters. Key processes in this structure building include the formation of stars and the collapse of gas within galaxies, which serve as fundamental building blocks for galaxy clusters. Meanwhile, in galaxy clusters, the nonlinear effect includes converting the kinetic energy gained by the infalling gas into thermal energy through adiabatic compression and the formation of shocks. As the gas settles into hydrostatic equilibrium (HE), its temperature approaches the virial temperature, corresponding to the cluster's mass. In the spherical collapse model described by Bertschinger (1985), supersonic accretion generates an expanding shock at the boundary between the hydrostatic gas and the cooler adiabatically compressed external medium. Moreover, other nonlinear effects, such as tidal forces and dynamical friction acting over galaxy members of clusters, further shaped the evolution of these structures, making the process highly complex and dependent on both dark matter and baryonic interactions. This nonlinear nature of cluster formation is essential for understanding the mass distribution, temperature profiles, and overall dynamics observed in galaxy groups and clusters today.

For this reason, numerical simulations are fundamental for the theoretical understanding of the formation and evolution of structures such as groups and clusters. Advances in computational power and the development of sophisticated numerical algorithms have allowed for detailed, three-dimensional simulations that capture both the dynamics of dark matter and the complex baryonic processes involved in groups and cluster formation. These simulations model the merger histories of clusters and the interaction of the ICM with galaxies and dark matter halo (Evrard, 1988; Kravtsov & Borgani, 2012).

Simulations, such as IllustrisTNG, have been successful in reproducing many observed properties of clusters, such as their density profiles, temperature distributions, and scaling relations. These models help to clarify the role of various physical processes, such as cooling, feedback from supernovae, and active galactic nuclei (AGN) feedback, in shaping the observed characteristics of clusters. Comparison of simulation results with observations is essential to refine our cluster formation models and to improve our understanding of the underlying physics (eg. Pillepich et al., 2018a,b; Springel et al., 2018; Donnari et al., 2019)

1.4 Galaxy population in dense environments.

Galaxies, are gravitationally bound systems comprised of baryonic material, primarily stars, gas, and dust, within the potential well of dark-matter halos. They show a wide range of distribution in colours and morphologies. Edwin Hubble first proposed a morphological classification of galaxies, based on optical observations in the blue band, that was only dependent on their appearance (Hubble, 1936). This classification separates galaxies into four main types: elliptical, spiral, and lenticular (Hubble, 1936). Elliptical galaxies display smooth, nearly elliptical isophotes and lack specific structural features such as spiral arms. Spiral galaxies feature prominent disk structures with well-defined spiral arms, further divided into normal and barred spirals based on the presence of a central bar. Lenticular galaxies, situated between elliptical and spiral galaxies, possess a disk and a bulge similar to spirals but lack spiral arms. Lastly, irregular galaxies do not adhere to any specific shape or structure and lack both a bulge and a disk. Historically, elliptical and lenticular galaxies are known as early-type galaxies, while spiral and irregular galaxies are known as late-type galaxies.

Since most of the light observed from a galaxy is emitted by its stars, the properties of galaxies, such as colour and metallicity, reflect the evolutionary processes of their stellar populations. Then, the colour of the galaxies provides insight into their star formation history, stellar populations, and overall composition. In this sense, the light of early-type galaxies is dominated by older stars, particularly red and low-mass stars, which are cooler and emit light primarily in the red and yellow parts of the spectrum. These stars are remnants of an earlier period of star formation, and since no new stars are forming, the overall light from the galaxy appears redder. On the contrary, the light of late-type galaxies has an important contribution of younger and hotter stars, including massive, short-lived blue stars (Conroy, 2013; Blanton & Moustakas, 2009). While the colour of a galaxy is largely determined by its stellar population age, metallicity also plays a crucial role. Higher metallicities tend to make stars redder and can increase dust extinction, which absorbs more blue light. As a result, two galaxies with similar colours can have different ages and levels of chemical enrichment, a phenomenon known as age-metallicity degeneracy (Worthey, 1994). However, this degeneracy is not strong enough to erase the broader trends seen in galaxy populations. The colour bimodality observed in galaxies remains a powerful tool for distinguishing between early-type and late-type galaxies. This bimodal distribution features a narrow red peak associated with early-type galaxies and a broader blue distribution for late-type galaxies. Despite the potential influence of age-metallicity degeneracy, the overall separation between red and blue galaxies is clear and persists across large galaxy samples. This bimodality is further reflected in the colour-magnitude diagram, where brighter galaxies tend to be redder, suggesting older and more metal-rich stellar populations than fainter galaxies (Baldry et al., 2004). An example of such bimodality in local galaxies is displayed in Figure 1.4.1.

One of the most fundamental properties of a galaxy is its luminosity. An important statistic of the galaxy distribution is, therefore, the luminosity function, $\phi(L)dL$, which describes the number density of galaxies with luminosities between L and $L+dL$. At the faint end, $\phi(L)dL$ seems to follow a power-law which truncates at the bright end, where the number density falls roughly exponentially. The galaxy luminosity function is commonly fitted by a Schechter function (Schechter, 1976) of the form:

$$\phi(L)dL = \phi^{*}\left(\frac{L}{L^{*}}\right)^{\alpha}\exp\left(-\frac{L}{L^{*}}\right)\frac{dL}{L^{*}}$$

Environmental factors significantly influence the luminosity function. Figure 1.4.2 compares the luminosity function for galaxies in the field in the right panel and galaxies in clusters in the left panel. The luminosity function in clusters shows a steeper faint-end slope and a more extended bright-end tail than their field counterparts. Also, while the shapes of luminosity functions for different morphological types remain similar across environments, the overall composite functions differ due to variations in the relative abundance of galaxy types. The increased presence of dwarf spheroidals in clusters contributes to the

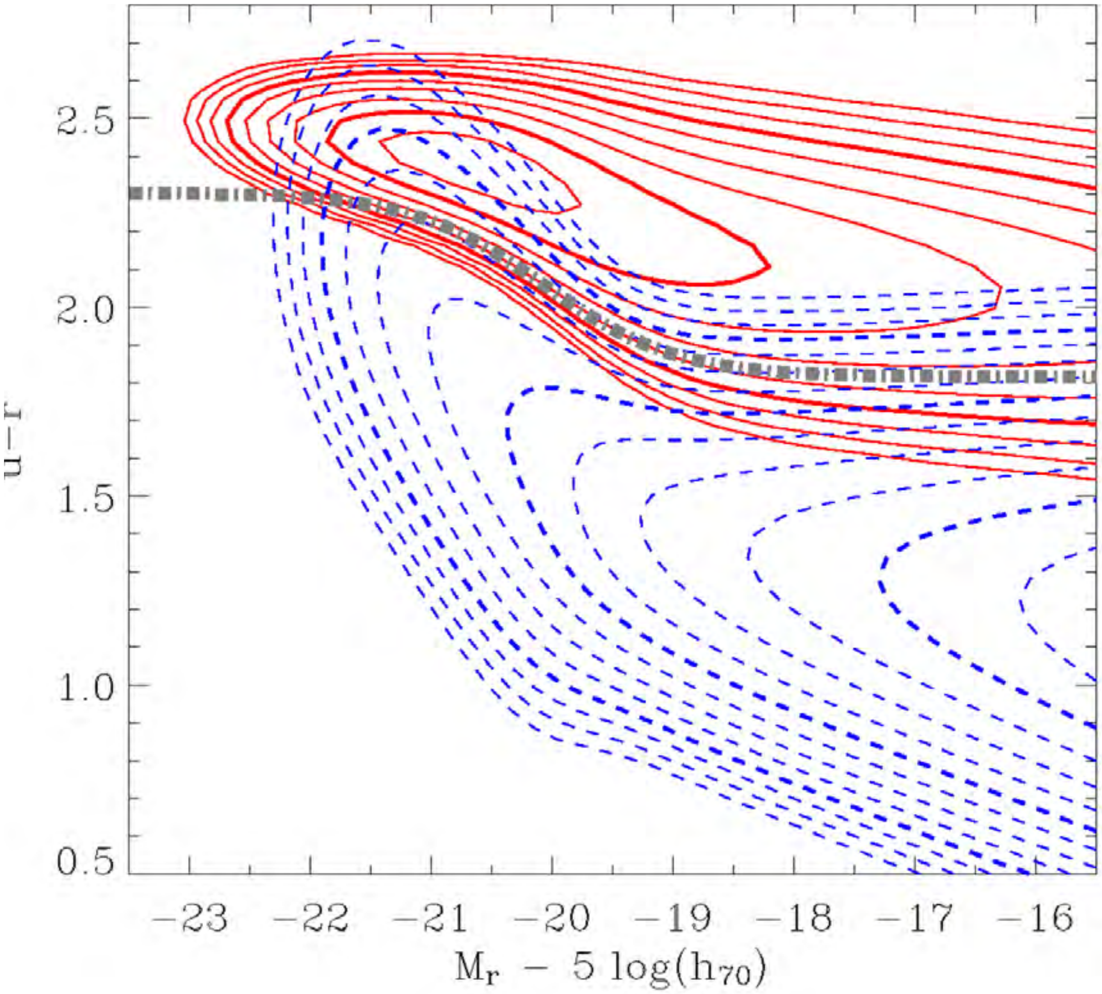

Figure 1.4.1: Illustration of the galaxy colour bimodality using a sample of galaxies observed with the Sloan Digital Sky Survey. This plot shows the presence of two galaxy populations, the red sequence and the blue cloud. Figure taken from Baldry et al. (2004).

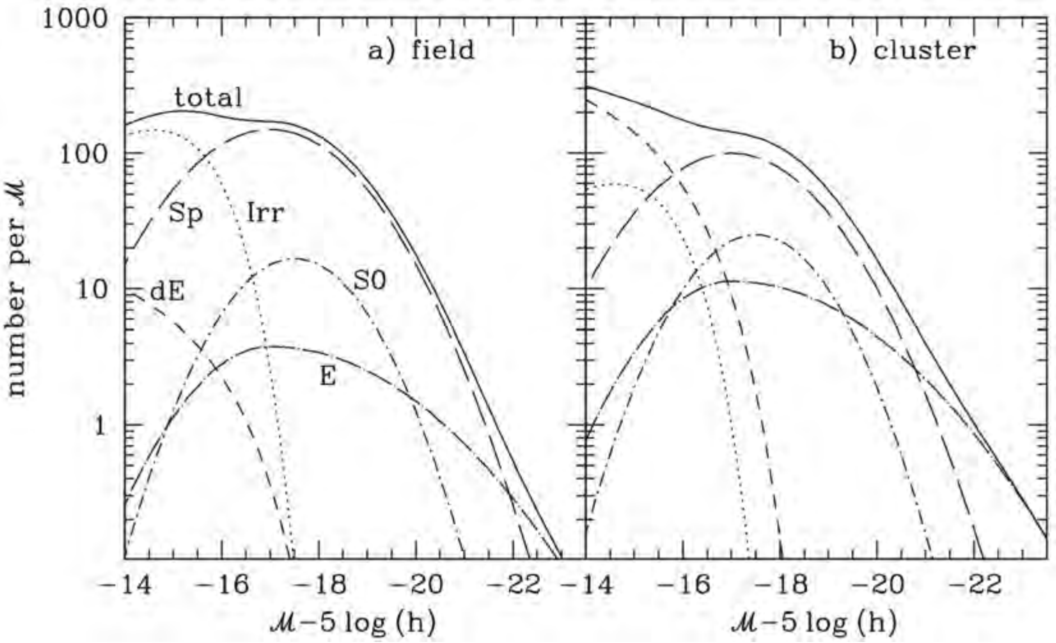

Figure 1.4.2: Luminosity function of galaxies shows differences between field and cluster environments, reflecting differences in galaxy populations. In the bright end of the luminosity function, elliptical galaxies are predominant, whereas spiral galaxies are more common in the intermediate luminosity range. At the faint end, irregular galaxies dominate the field, while dwarf elliptical galaxies are more prevalent in clusters. Figure taken from (Mo et al., 2010).

steeper faint-end slope, and the higher fraction of bright ellipticals explains the extended bright-end tail (Binggeli et al., 1988). Also, Dressler (1980) using a sample of 55 galaxy clusters and Saro et al. (2006) using cosmological simulations showed that the galaxy population not only varies depending on the environment but also changes depending on the cluster-centric distance. As shown in Figure 1.4.2 a significant fraction of the members inhabiting these clusters consist of elliptical and lenticular galaxies (Hubble, 1936; Dressler, 1980; Muzzin et al., 2012; Strazzullo et al., 2010; van der Burg et al., 2017). These early-type galaxies feature a well-defined linear relation between their colour and magnitude (Visvanathan & Sandage, 1977; Bower et al., 1992; Kodama & Arimoto, 1996), the so-called red sequence (RS). Such galaxies in the cluster RS have null or little ongoing star formation (Gladders & Yee, 2005; Gladders et al., 2007; De Propris et al., 2016), and their colour evolution can be remarkably well described by simple evolutionary models (Stanford et al., 1998). In fact, such models are so successful that they have been used to identify clusters (Gladders & Yee, 2000; Murphy et al., 2012; Bleem et al., 2015; Rykoff et al., 2016; Muzzin et al., 2012; Wilson et al., 2009) and to provide robust photometric redshifts up to $\sim$ 1.5 (e.g. Song et al., 2012; Bleem et al., 2015, 2020), with a precision better than $\sim 0.01 \times (1+z)$ up to z $\sim$ 1.0 (e.g. Rykoff et al., 2016; Klein et al., 2018, 2019).

While the slope and zero-point evolution of the RS describes the aging of galaxies' stars formed at z ~2 - 3 (at least up to z ~1.3, e.g., Mancone et al., 2010), the scatter provides information about its stellar population age diversity (Connor et al., 2019). Previous studies have shown that the scatter remains relatively constant up to z ~1 (e.g. Jaffé et al., 2011; Hennig et al., 2017). However, at $z \gtrsim 1.3$, the RS is found to be wider and bluer, indicating that at such redshift clusters are approaching their star formation epoch (Hilton et al., 2009; Papovich et al., 2010; Snyder et al., 2012). Furthermore, Brodwin et al. (2013) suggest that $z \sim 1.4$ could be where clusters star formation activity ends and the era of passive evolution begins.

1.5 Dynamical state of galaxy clusters

Galaxy clusters can be found in different dynamical states. In a relaxed cluster, the ICM is generally close to hydrostatic equilibrium. However, observations at different wavelengths suggest that a significant fraction of clusters, between 30% and 70%, are not fully virialised (Dressler & Shectman, 1988; Hou et al., 2012; Zhang et al., 2009; Andrade-Santos et al., 2017).

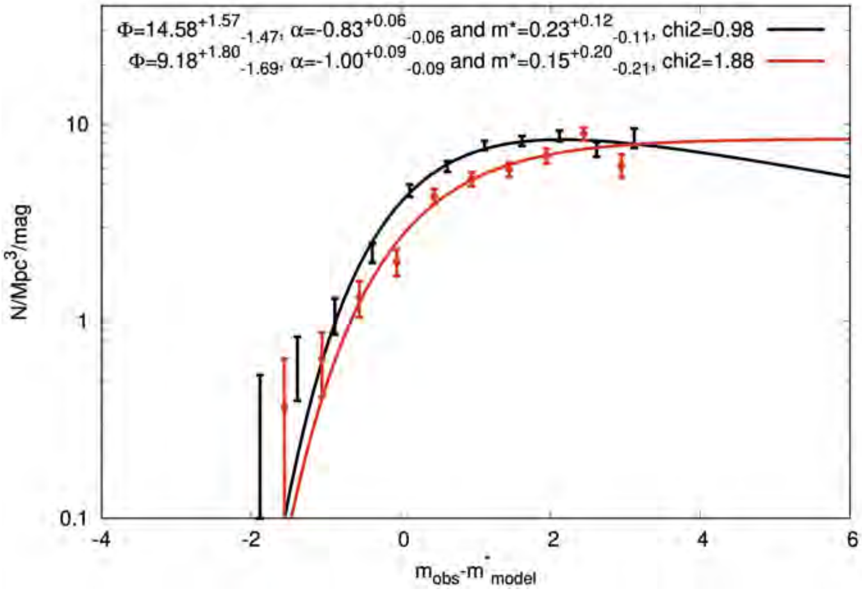

Figure 1.5.1: Differences in the luminosity function between relaxed and disturbed galaxy clusters in redshift between $0.1 < z < 0.9$ using DES observations. The luminosity function for the disturbed sample has a steeper α compared to the relaxed sample (Zenteno et al., 2020).

When two or more clusters of comparable mass undergo a merger process, this is referred to as a major merger. A major merger significantly impacts the properties of the clusters, such as their temperature, density, and distribution of dark matter. Such energetic cluster merging events can trigger and/or quench star formation in their galaxy members, thus affecting their observable properties such as colours. Previous works have studied the differences between the star formation rates of galaxies in disturbed clusters with respect to their relaxed counterparts. Yet, there is no agreement about whether a galaxy's star formation rate is stimulated or suppressed during large merger events. For example, both Pranger et al. (2014) through an analysis of the galaxy population in Abell 3921, and Kleiner et al. (2014) in A1750, found that mergers quench star formation. Shim et al. (2011) also studied the interacting cluster A2255, finding that the cluster merging process suppresses star formation and transforms galaxies into quiescent galaxies. However, other authors such as Ferrari et al. (2003), by a spectroscopic analysis of Abell 521, and Owers et al. (2012) by studying the cluster Abell 2744 (which is currently undergoing a major merger), found that the high-pressure merger environment triggers star formation. In support of this, Sobral et al. (2015) and Yoon & Im (2020) found that the star formation rate in the interacting clusters is around 20% higher than that observed in relaxed structures. Such findings are confirmed using Hα observations of disturbed and relaxed clusters at $z < 0.4$, finding a higher prevalence of Hα emitter galaxies in disturbed clusters within 2 Mpc from the cluster's centre than in relaxed clusters (Stroe et al., 2017; Stroe & Sobral, 2021). In the same way, Hou et al. (2012), studying groups of galaxies at intermediate redshifts ($z \sim 0.4$), showed that galaxies in groups with substructures present a significantly higher blue galaxy population compared to galaxy groups with no detected substructures. Finally, Zenteno et al. (2020) showed that there are differences in the luminosity functions between relaxed and disturbed clusters (See Figure 1.5.1). Indeed, in disturbed clusters the luminosity function exhibits a steeper faint-end slope, α, and a brighter characteristic magnitude, m^*, than relaxed clusters. These differences are primarily observed in clusters at redshifts $z > 0.6$, while at lower redshifts, the luminosity functions of disturbed and relaxed clusters are similar.

From an observational standpoint, the dynamic state of clusters has been quantified using data from different wavelengths. Radio-emitting clusters are often associated with disturbed clusters due to shocks during merging that can trigger the acceleration of charged particles and lead to synchrotron radiation (Brunetti et al., 2008). In contrast, those lacking radio emission are considered relaxed clusters (Brunetti et al., 2007, 2009; Feretti et al., 2012). The presence of a cool core in X-ray observations of clusters has also been used as an indicator of a relaxed state in these clusters. A shorter radiative cooling time in the cluster core than the cluster's age suggests that the cluster has likely attained a relaxed state (Bauer et al., 2005). This inference is grounded in the fact that X-rays emitted by the ICM induce a temperature drop in the innermost regions of galaxy clusters. This is because the X-ray emission from the intracluster medium (ICM) is proportional to the square of the gas density, which is higher in relaxed clusters due to gravitational collapse. In these clusters, the gas in the core has had time to settle and become denser, leading to enhanced radiative cooling and a drop in temperature in the central regions. In addition, some authors have investigated the dynamical state of galaxy clusters by examining morphological parameters of their X-ray emission, such as the asymmetry parameter (A_{phot}). This parameter quantifies the deviation of the photometric distribution within a specific annulus from a symmetric distribution (Nurgaliev et al., 2013, 2017). Another parameter commonly used is the centroid shift, which measures the offset between the position of the centroid of the X-rays surface brightness and the peak of the X-ray emission (Nurgaliev et al., 2017; Yuan et al., 2022; Campitiello et al., 2022). In this sense, Campitiello et al. (2022) defined a relaxation parameter (M) to produce a unique indicator of the dynamical state of the clusters as the combination of the centroid shift (separation between the X-ray peak and the centroid of the X-ray surface brightness), the concentration index, which measures the ratio of the surface brightness measured in two apertures (0.1 and 1 R_{500}), and the power ratio, which is based on the multipolar two-dimensional decomposition of the X-ray surface brightness.

1.6 Mergers of galaxy groups and clusters.

During the mergers, when galaxies, groups, and clusters orbit near other groups or clusters, those objects experience different processes capable of removing gas, dark matter, and even stars from the individual galaxies, modifying their star formation activity, and even changing their morphology. In this section, we discuss the main process that affects satellite galaxies.

1.6.1 Dynamical friction

Dynamical friction is a drag force that acts on a massive object (subject mass M_S) as it moves through a larger system composed of particles (field particles) of much lower mass ($m \ll M_S$). This force arises from two-body interactions, where the subject mass perturbs the distribution of the field particles, creating a gravitational wake behind it. The gravitational pull of this wake slows the object down, causing it to lose kinetic energy and momentum over time.
The energy and momentum loss due to dynamical friction can be described by *Chandrasekhar's formula* for the dynamical force F_{dyn} (Binney & Tremaine, 2008):

$$F_{\mathrm{dyn}} = -4\pi \left(\frac{GM_S}{v_S^2}\right)^2 \rho(< v_S) \ln(\Lambda) \frac{\mathbf{v}_S}{v_s}$$

where $v_s = |\mathbf{v}_S|$ is the velocity of the subject mass M_S, $\rho(< v_S)$ is the density of the field particles with speeds less than v_S, and $\ln(\Lambda)$ is the Coulomb logarithm which is a function of the impact parameter $\ln\Lambda \simeq \ln\left(\frac{b_{max}}{b_{90}}\right)$ (Binney & Tremaine, 2008). Dynamical friction induces the loss of energy and angular momentum for a relatively massive object orbiting within a host system as it transfers these quantities to the system's field particles. As a result, the orbit of the massive object gradually decays over time, bringing it closer to the centre of the host's potential well, thus enhancing tidal effects. Using the formula for the dynamical friction force and considering a subject mass falling from an initial orbit of radius r_i on a circular host of mass M_h, the time it takes to decay to zero radius can be estimated as:

$$t_{df} \approx \frac{1.17}{\ln(M_h/M_S)} \left(\frac{M_h}{M_S}\right) \frac{1}{10H(z)}$$

From the last formula, we can derive that for systems with $M_h/M_S \geq 15$, t_{df} is larger than the age of the Universe, meaning only more massive satellites tend to move toward the centre of a gravitational potential well, while lighter objects or particles remain more widely distributed Mo et al. (2010).

1.6.2 Ram-pressure stripping

Ram-pressure stripping (RPS) affects galaxies or groups as they move through the gaseous dense medium of a galaxy cluster and can be estimated as:

$$P_{ram} = \rho \times v^2$$

where ρ is the density of the medium and v is the velocity of the infalling structure relative to the medium (Gunn & Gott, 1972). The gaseous material from the infalling structure is removed when this pressure, exerted by the intracluster medium, overcomes the gravitational force holding the galaxy's gas in place (Maier et al., 2019; Roberts et al., 2019). The effectiveness of RPS increases with the mass of the host galaxy cluster (M_{200}) because more massive clusters have denser circumgalactic medium and higher relative velocities of infalling satellites. Furthermore, within a given cluster, RPS is more intense at a smaller clustercentric radius due to higher ambient densities and faster galaxy velocities deeper in the cluster's gravitational potential well.

For a satellite galaxy, RPS first strips away the less gravitationally bound gas, such as hot or diffuse gas, a phenomenon observed in the outer regions of galaxies and supported by both observations (Balogh & Morris, 2000) and semi-analytic models (Cole et al., 2000; Somerville et al., 2008; Ayromlou et al., 2019). Furthermore, the interaction between RPS and the satellite's gas can compress the gas at the leading edge of the infalling galaxies, potentially triggering short-lived periods of enhanced star formation (Dressler, 1980; Vulcani et al., 2018; Roberts et al., 2022) and increased AGN activity (Poggianti et al., 2017; Maier et al., 2022; Peluso et al., 2022). Feedback from such star formation and AGN activity might facilitate the RPS given that it lowers the binding energy of the ISM gas (Garling et al., 2024).

RPS is a key mechanism in the quenching of star formation in galaxies, particularly in dense environments like galaxy clusters. As a result of the RPS, the galaxy loses its gas, which is its primary material for star formation, significantly reducing its ability to form new stars. This explains why clusters often show a notable deficiency in gas-rich star-forming galaxies compared to less dense environments (Boselli & Gavazzi, 2006). With the removal of its interstellar medium, the affected spiral galaxy ceases star formation and may evolve into an S0 galaxy, which is characterised by a disk-like structure but without significant star-forming activity, while the majority of red disks were probably quenched by feedback from the active galactic nucleus (AGN) (Łokas & Mamon, 2003). This transformation through ram-pressure stripping provides a reasonable explanation for the higher fraction of S0 galaxies observed in clusters compared to the field (Dressler, 1980; Boselli et al., 2014).

1.6.3 Tidal Stripping

Tidal stripping is the other important process that produces mass loss and galaxy transformations inside a cluster. As galaxies orbit within a galaxy cluster's gravitational potential, they experience tidal forces that can strip stars, gas, and dark matter from their outer regions. Tidal stripping is particularly intense during close encounters with other galaxies or the cluster's core, where the gravitational forces can exceed the galaxies' internal binding forces. The stripped material often becomes part of the Intracluster Light (ICL), which is a diffuse, faint light that exists between galaxies within a galaxy cluster. This light is emitted by stars that are not bound to any individual galaxy but instead are scattered throughout the space between galaxies (Moore et al., 1999; Gnedin, 2003; Mastropietro et al., 2005).

Assuming a satellite galaxy falling slowly to the host structure, and having a spherically symmetric mass distribution, material outside the tidal radius (R_t) will be stripped from the satellite. This radius can be identified as the distance from the satellite centre at which the radial forces acting on it cancel. Under these assumptions, we can derive that this radius can be expressed as:

$$R_t \approx \frac{1}{\sqrt{2}} \frac{\sigma_{sat}}{\sigma_{halo}} r,$$

where σ_{sat}, and σ_{halo} are the velocity dispersion of the satellite and the halo, respectively, and r represents the distance from the central galaxy to the satellite. Moreover, tidal forces not only strip material, but also stir the galaxies' internal structure, potentially transforming their morphology. This process, known as tidal stirring, can disturb the disk structures of spiral galaxies, converting them into spheroidal shapes. This morphological transformation is closely linked to the morphology-density relation observed in galaxy clusters, where early-type galaxies (ellipticals and lenticulars) are predominantly found in dense cluster centres, while late-type galaxies (spirals) are more common in the outskirts (Dressler, 1980). This relation has been confirmed in numerous clusters, including the Coma Cluster, where elliptical galaxies exhibit a steeper density profile compared to spirals, indicating their greater susceptibility to tidal forces within the dense cluster environment (Łokas & Mamon, 2003). Tidal stripping and stirring thus play a crucial role in shaping the evolutionary pathways of galaxies within clusters, influencing their structure, dynamics, and distribution across the cluster environment.

1.6.4 Galaxy pre-processing

Galaxies currently residing in groups and clusters may have taken various pathways to become satellites. To simplify, the two primary scenarios are: i) a galaxy falls directly into the main branch of its host at $z = 0$ and remains there until the present time; we refer to this as falling as centrals. ii) a galaxy is accreted by a smaller subgroup at $z > 0$, which, given the hierarchical nature of structure formation, eventually merges into the main progenitor of a group or cluster at $z = 0$. These galaxies are referred to as falling as satellites or pre-processed. Then pre-processing refers to the phenomenon in which galaxies experience environmental quenching mechanisms before they are accreted into their current host cluster or group. Donnari et al. (2020) showed that at least half of the satellite galaxies with masses between 10^9 $\mathrm{M}_\odot$ and 10^{10} $\mathrm{M}_\odot$, which today are found in 10^{14} $\mathrm{M}_\odot$ clusters, have been satellites of other hosts. For this reason, pre-processed galaxies may have suffered galaxy-host interactions for a very long time. This suggests that their star formation was suppressed during earlier phases of group membership. The likelihood of a galaxy being quenched through pre-processing increases with the mass of the host; larger clusters are more likely to have pre-processed galaxies because their satellites have often undergone earlier stages of environmental quenching in smaller subgroups (Zabludoff et al., 1996; McGee et al., 2009; Bahé et al., 2019). The typical host mass in which environmental quenching occurs predominantly is $M_{200} = 10^{13} - 10^{14} M_\odot$ (Pallero et al., 2019). This reinforces the role of galaxy groups, rather than clusters, as building blocks in the hierarchical formation of cosmic structures. However, even after excluding satellites quenched by AGN feedback or through pre-processing, massive clusters are still more effective at quenching their members compared to lower mass hosts (Donnari et al., 2020; Pallero et al., 2022).

Reinforcing this, Pallero et al. (2022) using the EAGLE zoom-in simulations of galaxy clusters showed that, at low redshift, a large fraction of the present-day cluster galaxy population arrives at the cluster pre-processed, regardless of the cluster mass. However, at higher redshifts, most galaxies reach their quenching state in situ, independent of the cluster mass. The quenching mechanisms associated with pre-processing are diverse but primarily driven by RPS and tidal forces. These effects become more pronounced as galaxies enter increasingly dense environments, rapidly depleting their cold-gas reservoirs and leading to quenching galaxies. While pre-processing affects a broad range of galaxies, it tends to be more dominant in lower-mass galaxies that are particularly vulnerable to these environmental effects. Observationally, Lopes et al. (2023) analyzed a sample of 238 galaxy clusters and found that the fraction of star-forming galaxies in infalling groups exhibits a distinct cluster-centric behavior compared to galaxies that have fallen in as central members. They observed that, even in the more peripheral regions of the cluster, galaxies within infalling groups already show a reduced fraction of star-forming objects.

1.7 Galaxy Clusters self-similarity

Self-similarity scaling relations are mathematical relationships that describe how the physical properties of cosmological structures scale with each other in a universal manner. In galaxy clusters, these relations are based on the assumption that those objects, despite their differences in mass and size, exhibit a ”self-similar” behavior; i.e. if we consider two quantities, we can demonstrate that they are related to each other by a power law. One of the most important scaling relation in galaxy clusters is between the luminosity in X-rays L_X and the cluster mass M_{500}. Observing these wavelengths is particularly useful because the X-ray emission is proportional to the square of the hydrogen number density, minimising susceptibility to line-of-sight projection effects (Ramos-Ceja et al., 2019). The analysis of these X-ray emission provides critical information about the physical conditions within galaxy clusters, such as temperature, density, and metallicity profiles, which are key to understanding the thermodynamic state of the ICM and the assembly history of clusters (Voit, 2005; Sarazin, 1986). Galaxy clusters, despite differing in mass and size, follow a universal set of rules in their evolution and structure.

As previously discussed, the ICM, which constitutes the bulk of baryonic matter in clusters, is a hot, X-ray-emitting plasma that traces the cluster's gravitational potential. The gas in the clusters is heated to temperatures of 10^7 to 10^8 K by adiabatic compression and shocks during the collapse, reaching a state of hydrostatic equilibrium within the cluster's gravitational potential. As the gas becomes dense enough, it cools, potentially fuelling star formation and the growth of supermassive black holes (SMBHs) in massive cluster central galaxies. This cooling and subsequent formation of stars and SMBHs can trigger energetic feedback from supernovae (SNe) and active galactic nuclei (AGN), which can significantly influence the thermal state and evolution of the ICM affecting the observed X-ray emission.

A comprehensive description of cluster evolution and its emission in X-rays requires accounting for the described complex non-linear processes. However, the self-similar model proposed by (Kaiser, 1986) provides baseline predictions for the evolution of cluster scaling relations that closely match observational results.

The derivation of the self-similarity scaling relations relies on the assumption that the ICM in galaxy clusters is in hydrostatic equilibrium, i.e. its pressure and density are related as:

$$\frac{1}{\rho}\frac{dP}{dr} = -\frac{GM}{r^2}$$

We can assume that the cluster is spherically symmetric and the local gas density ρ is related to the temperature T by the perfect gas law $p = \rho kT/\mu m_H$, where m_H is the mass of the hydrogen atom and μ is the mean molecular weight of the gas. For a fully ionised gas with the standard cosmic abundance of the elements, we can assume $\mu = 0.6$. Differentiating the perfect gas law with respect to r and using the hydrodynamical equilibrium, we see that the total mass inside a given cluster radius is given by:

$$M(<r) = -\frac{k_B T(r)}{\mu m_p G}\left(\frac{d\ln\rho(r)}{d\ln r} + \frac{d\ln T(r)}{d\ln r}\right)$$

After that, we can estimate the total mass of a galaxy cluster using the gas density and temperature radial profiles. If we define the cluster mass (M_Δ) as the mass inside a spherical region of radius r_Δ, then it can be expressed as:

$$M_\Delta = \frac{4\pi}{3}\Delta\rho_c(z)r_\Delta^3$$

Where, from Section 1.2, ρ_c is the critical density that depends on the the Hubble parameter which is a functions of the redshift. Assuming that galaxy clusters fit the self-similarity criteria, i.e. larger clusters are just scaled-up versions of smaller ones, then:

$$M_\Delta \propto \Delta\rho_c(z)r_\Delta^3 \propto E^2(z)r_\Delta^3$$

Given that the gas heated by gravitational infall is assumed to be in equilibrium within the gravitational potential ϕ of the cluster, it is expected to have the temperature $kT \propto \phi \propto M_\Delta/r_\Delta$. Then, the relation between the mass and the radius scales as:

$$TE^{-2/3} \propto M_\Delta^{2/3}$$

The scaling relation between the X-ray luminosity can also be derived as follows. The X-ray luminosity is proportional to the square of the density ρ^2 and proportional to cooling function Λ. Assuming that the main channel of X-ray emission is the bremsstrahlung emission ($\Lambda \propto T^{1/2}$), integrated into the cluster volumes, then:

$$L_{X,\Delta} \propto \rho^2\Lambda r_\Delta^3 \propto \frac{M_{gas}^2}{r^3}T^{1/2}$$

Under the self similarity model, assuming that the gas mass fraction is independent of the cluster mass, then the $M_{gas} \propto M_\Delta$. Then, the X-ray luminosity scales with the total mass as:

$$L_{X,\Delta} \propto M_\Delta^{4/3}E(z)^{7/3}$$

These scaling relations provide a framework for connecting fundamental properties of galaxy clusters, such as mass, with observable quantities, such as X-ray luminosity and temperature. The derived scaling relations are particularly valuable because they reflect the universal nature of gravitational processes, offering a powerful tool for studying the underlying physics of large-scale structures in the universe.

1.8 Scope of this thesis.

In this thesis, we combined observational data obtained with the Dark Energy Camera (DECam) and the full-physics cosmological simulations Illustris-TNG and Millenium-TNG to characterise the differences in the impact of the dynamical state of galaxy groups and clusters on the physical properties of their satellite galaxies. Those properties includes the red sequence morphology, colour distribution, quenched fractions, and gas availability, and the scaling relations that allow estimating the virialisation stage of the largest structures in the Universe.

This thesis addresses the key questions:

- How do cluster mergers influence the cluster red sequence, particularly in colour, across different redshifts in galaxy clusters?
- How does the dynamical state of galaxy groups and clusters influence their galaxy populations' colour, star formation rate, and gas availability?
- How do the scaling relations derived from X-ray emissions differ between relaxed and disturbed galaxy clusters, and how do these relations compare to observational data and theoretical predictions?

In Chapter 2, we provide a detailed description of the cosmological simulations employed in this thesis. This chapter covers the methodologies, physical models and technical aspects of the simulations.

In Chapter 3, we analyse a sample of 84 galaxy clusters observed with the Dark Energy Camera, covering a redshift range of 0.11 to 0.88. Our objective is to assess how cluster mergers affect galaxy populations using colour-magnitude diagrams. We show that high-redshift clusters contain a higher fraction of blue galaxies, regardless of their dynamical state. Specifically, in the high-redshift bin, disturbed clusters display a larger scatter in the Red Sequence, with a broader distribution and more blue galaxies compared to relaxed clusters. In contrast, at lower redshifts, there is an agreement between the galaxy populations in relaxed and disturbed clusters. These findings suggest that in massive cluster halos at $z < 0.55$, galaxy quenching occurs primarily as galaxies become satellites of another structure, while at $z \geq 0.55$, quenching is primarily driven by in-situ processes within the cluster.

In Chapter 4, we investigate the impact of the dynamical state of galaxy groups and clusters on the physical properties of their galaxy populations, using the most massive halos ($M \gtrsim 10^{13} M_{\odot}$) from the Illustris TNG100 simulations. Galaxy groups and clusters, as the most massive gravitationally bound structures in the Universe, form by merging smaller structures. These mergers provide a dynamic environment that influences the evolution and transformation of their satellite galaxies. We aim to characterise the distribution of galaxy colours, specific star formation rates (sSFR), quenched galaxy fractions, and gas availability in galaxies bound to these massive structures. As in Chapter 3, we focused on the analysis of galaxies bounded to relaxed and disturbed clusters. Here, the classification of these different structures was done based on the offset between the Brightest Cluster Galaxy (BCG) and the gas's centre of mass. The galaxy populations were further divided into red and blue galaxies using a threshold derived from a double Gaussian fit to their colour distribution. Additionally, galaxies were classified as star-forming or quenched using a threshold defined as one dex below the interpolated star-formation main sequence. Our results reveal significant differences in the physical properties of galaxies in disturbed versus relaxed clusters. Disturbed clusters exhibit a higher fraction of blue star-forming galaxies than their relaxed counterparts. This discrepancy is attributed to the increased gas availability, including hot, diffuse, and condensed gas, in satellite galaxies within disturbed clusters. We also identify two critical phases in the merging process: an initial phase characterised by a significant boost in star-formation rates, followed by a suppression as the cluster approaches equilibrium.

In Chapter 5, we developed a pipeline to generate mock X-ray emission maps of galaxy clusters to study the differences in scaling relations between relaxed and disturbed clusters. We produced these mock X-ray maps using Illustris TNG-300 and Millennium TNG-740 full-physics simulations and validated our pipeline by comparing the resulting scaling relations with existing observational data. The clusters were categorised as relaxed or disturbed to explore variations in key X-ray-derived parameters, such as the concentration index, centroid offset, and power ratios. We derived scaling relations between L_X and M_{500} across a broad mass range. Furthermore, our study indicates that a broken power law can describe these scaling relations with a pivot at $10^{14} M_{\odot}$. The slopes for high-mass clusters ($M > 10^{14} M_{\odot}$) align with theoretical predictions based on the self-similarity assumption, providing new insights into the impact of cluster dynamical states on X-ray scaling relations.

Chapter 2

Cosmological Simulations

As discussed in Chapter 1, structure formation in the Universe is mainly driven by a variety of nonlinear processes that are often coupled or acting over a wide range of scales. Thus, because of their complexity, cosmological simulations are used to track the time evolution of cosmic structures. The resulting models are analysed to compare with the observed properties derived from the large amount of observational data available from modern surveys, thus providing important clues for our understanding of the physics governing this process. The earliest simulations of the galactic structure were performed by Lindblad (1960). Then, simulations of cluster collapse and evolution, using identical particles interacting via gravitational force in three dimensions, were carried out by Peebles & Yu (1970), and by White (1976). However, the first simulations of cosmological clustering in an expanding universe were done by Aarseth et al. (1979), Haggerty & Janin (1974), and (Miyoshi & Kihara, 1975). These simulations used a particle-particle method to compute forces, which strongly limits the number of particles that could be considered. To overcome this limitation, alternative methods such as the particle mesh (Klypin & Shandarin, 1983; White et al., 1983) or tree code (Barnes & Hut, 1986; Hernquist, 1987; Bouchet & Hernquist, 1988) were developed, which offer much better efficiency and scalability.

Computational methods to perform simulations have rapidly evolved, allowing us nowadays to produce simulations of large cosmological boxes, not only including the collisionless dark-matter particles but also adding the baryonic component. This clearly significantly increases the complexity of the simulations: Although DM interacts only gravitationally, many other physical processes have to be modelled when considering baryons. Hydrodynamical simulations such as IllustrisTNG (Weinberger et al., 2017; Pillepich et al., 2018a; Springel et al., 2018; Nelson et al., 2018) and MilleniumTNG (Pakmor et al., 2023) are intended to describe the evolution of structures such as galaxies, groups, and clusters, including the time evolution of those matter components. In this sense, dark matter, which is the dominant driver of structure formation (Mo et al., 2010), is modelled as a collisionless fluid which dynamical evolution is described by the Vlasov equation given by:

$$\frac{df}{dt} = \frac{\partial f}{\partial t} + \frac{\partial f}{\partial x} \cdot v + \frac{\partial f}{\partial v} \cdot \left(- \frac{\partial \Phi}{\partial x} \right) = 0 \tag{2.0.1}$$

$$\nabla^2 \Phi(x,t) = 4\pi G \int f(x,v,t)dv \tag{2.0.2}$$

Where f is a general distribution function of particles with velocity v at coordinates x and given time t. At small scales, the baryonic component plays a dominant role. The equations that govern the gas dynamics in the universe can be described using the Euler/Navier-Stockes equations which are the conservation laws for mass, momentum and energy. The equations of ideal magnetohydrodynamics(MHD) can be written as (Pakmor & Springel, 2013):

$$\begin{aligned}
\frac{\partial \rho}{\partial t} + \frac{1}{a}\nabla(\rho V) &= 0 && (2.0.3)\\
\frac{\partial}{\partial t}(\rho w) + \nabla(\rho v v^T + I p_{tot} - \frac{BB^T}{a}) &= -\frac{\rho}{a}\nabla\Phi && (2.0.4)\\
\frac{\partial \varepsilon}{\partial t} + a\nabla[v(E + p_{tot}) - \frac{1}{a}B(v \cdot B)] &= \frac{\dot{a}^2 B^2}{2} - \rho(v \cdot \nabla\Phi) + a^2(\mathcal{H} - \Lambda) && (2.0.5)\\
\frac{\partial B}{\partial t} + \frac{1}{a}\nabla \cdot (B v^T - v B^T) &= 0 && (2.0.6)
\end{aligned}$$

With,

$$w = av, \; \varepsilon = a^2 E$$

Where, x and v are the proper positions and velocity vectors, a is the scale factor, ρ is the density, p is the pressure, Φ is the gravitational potential, B is the magnetic field strength, u_{th} denotes the thermal energy per unit volume, and p_{tot} is the total gas pressure. This set of basic equations allows us to model the time evolution of the phase-space distribution of constrained cosmic regions. The total energy and pressure are calculated as:

$$E = \rho u_{th} + \frac{1}{2}\rho v^2 + \frac{B^2}{2a}$$

$$p_{tot} = (\gamma - 1)\rho u_{th} + \frac{B^2}{2a}$$

2.1 AREPO code

The Vlasov equation describes the time evolution of the phase-space distribution function of a collisionless fluid. However, the high dimensionality of this equation makes the direct discretisation very difficult (Yoshikawa et al., 2013). As a result, it is necessary to sample the phase space using discrete particles and solve their equations of motion. To compute those solutions, AREPO uses the Tree-particle-mesh (Tree-PM) algorithm, which is the combination of two techniques: the oct-tree algorithm and a grid-based approach. The TreePM algorithm combines the strengths of the oct-tree and particle mesh methods to efficiently calculate gravitational forces. The particle-mesh (PM) approach is effective in computing long-range forces and is particularly suited for periodic boundary conditions, as it solves the Poisson equation using Fourier transformations on a regular grid. However, it is limited by the grid resolution, which restricts its dynamic range. In contrast, the oct-tree algorithm excels at handling short-range interactions and large dynamic ranges, as it groups distant particles and calculates their collective contribution to the overall force. For these reasons, the TreePM method divides the gravitational force into short-range and long-range components (Weinberger et al., 2020). The long-range forces are computed using the PM algorithm, while the short-range forces are handled by the tree algorithm. This hybrid approach allows AREPO to efficiently model both large-scale structures and high-resolution details, making it well-suited for cosmological simulations where periodic boundaries and highly clustered particle distributions are common. This implementation of TreePM follows a similar approach as in the Gadget code (Springel, 2005) and more details of the method were introduced by Bagla (2002).

AREPO solves the hydrodynamics equations using a finite-volume method on an unstructured, moving Voronoi tessellation of the simulation domain. Each cell tracks conserved quantities such as mass, momentum, and energy, and for magnetohydrodynamics (MHD), the cell-averaged magnetic field. AREPO's moving, unstructured mesh, generated via Voronoi tessellation, adapts naturally to the fluid flow, offering Lagrangian-like behaviour regarding resolution and adaptivity. This approach overcomes the limitations of Smoothed Particle Hydrodynamics (SPH) and fixed-grid Eulerian methods. Unlike SPH, which struggles with fluid instabilities and poor shock resolution, AREPO avoids these issues while maintaining the benefits of adaptive resolution in high-density regions. Similarly, AREPO addresses the lack of Galilean invariance in Eulerian methods, ensuring that results remain consistent regardless of the reference frame, which is crucial in cosmological simulations involving large-scale flows (Gene et al., 2014). Eulerian methods, despite their accuracy in shock resolution, are limited by their fixed grids, leading to overmixing and complications with high-velocity flows. SPH, while adaptive, fails to capture instabilities like the Kelvin-Helmholtz and Rayleigh-Taylor, and its modifications, such as artificial viscosity, remain imperfect solutions (Lucy, 1977; Gingold & Monaghan, 1977; Tasker et al., 2008; Wadsley et al., 2008). In AREPO, the Voronoi mesh adjusts dynamically to fluid density, concentrating resolution in high-density regions (e.g., galaxies, shock fronts) while reducing computational costs in low-density areas. Its second-order Godunov scheme with an exact Riemann solver allows it to accurately capture shocks and discontinuities, which is essential for simulating astrophysical phenomena such as supernovae and galaxy mergers. Furthermore, AREPO is highly parallelised for efficient scaling on distributed memory systems, allowing large high-resolution simulations of galaxy clusters and cosmological volumes (Springel, 2010).

Both simulations analysed in this thesis, Illustris TNG and MilleniumTNG, use the AREPO code. However, the version used in Millenium TNG has major updates compared to the one used in IllustrisTNG. For the MillenniumTNG (MTNG) project, several technical enhancements were made to fit the large simulation MTNG740, which has a box size of 740 Mpc per side.

This simulation has 4320^3 DM particles and an identical number of gas cells (see section 2.3), within the memory constraints of the supercomputer. Although the core physics model remained largely consistent with the IllustrisTNG's model, significant optimisations were introduced. One major change was the use of shared memory on computing nodes via MPI-3, allowing data like domain decomposition and top-level tree structures to be stored only once per node instead of once per computer, reducing memory usage. Efficiency improvements were also made in global MPI operations by first computing collective results on a node level before inter-node communication. The operations of the gravitational tree algorithm were reordered to minimise the waiting times caused by the varying number of imported and exported elements. Additionally, the simulation incorporated real-time post-processing, such as friends-of-friends (FoF) group finding, substructure detection using the SUBFIND-HBT algorithm, merger tree computations and light-cone output (Pakmor et al., 2023).

2.2 IllustrisTNG simulations

This suite of simulations has three different box sizes: 50 Mpc, 100 Mpc, and 300 Mpc per side, hereafter TNG50, TNG100, and TNG300, respectively. Each box has different mass resolutions for CDM and baryonic particles. In Table 2.2.1, we present the main features of the simulations of the IllustrisTNG suite including the boxsize, number of particles, mass resolutions, and softening lengths. The three simulation boxes complement each other by focussing on different aspects of galaxy formation. The largest box, TNG300, with its substantial physical volume, facilitates the study of galaxy clustering, the examination of rare objects like galaxy clusters, and provides the most extensive galaxy sample. On the other hand, although the smaller volume of the TNG50 simulation limits the sampling of rare objects, it achieves a mass resolution a few hundred times higher than that of TNG300. TNG100 strikes a balance between mass resolution and sample of galaxies. Each of the three simulation boxes has been run at three resolution levels.

Table 2.2.1: The TNG300, TNG100, and TNG50 simulations of IllustrisTNG: table of physical and numerical parameters for the three resolution levels of the three simulations. The parameters are: the box side-length, the initial number of gas cells and dark matter particles, the target baryon mass, roughly equal to the average initial stellar particle mass, the dark matter particle mass, and the gravitational softening of the collisionless component.

Series	Run	Boxsize [Mpc]	N_{gas}	N_{DM},	N_{tracer},	m_b $[h^{-1}M_\odot]$	m_{DM}, $[h^{-1}M_\odot]$	ε $[h^{-1}kpc]$
TNG300	TNG300(-1)	302.6	2500^3	2500^3	2500^3	7.44×10^6	3.98×10^7	1.0
	TNG300(-2)	302.6	1250^3	1250^3	1250^3	5.95×10^7	3.19×10^8	2.0
	TNG300(-3)	302.6	625^3	625^3	625^3	4.76×10^8	2.55×10^9	4.0
TNG100	TNG100(-1)	110.7	1820^3	1820^3	2×1820^3	9.44×10^5	5.06×10^6	0.5
	TNG100(-2)	110.7	910^3	910^3	2×910^3	7.55×10^6	4.04×10^7	1.0
	TNG100(-3)	110.7	455^3	455^3	2×455^3	6.04×10^7	3.24×10^8	2.0
TNG50	TNG50(-1)	51.7	2160^3	2160^3	1×2160^3	5.7×10^4	3.1×10^5	0.29
	TNG50(-2)	51.7	1080^3	1080^3	1×1080^3	4.6×10^5	2.5×10^6	0.58
	TNG50(-3)	51.7	540^3	540^3	1×540^3	3.7×10^6	2.0×10^7	1.15

The groups and clusters in the Illustris-TNG simulations were identified using the Friend-of-Friends algorithm with a linking length of 1 h^{-1}kpc, 0.5 h^{-1}kpc, and 0.2h^{-1}kpc for TNG300, TNG100, and TNG50 respectively (Springel et al., 2018). Their corresponding subhalos were identified using the SUBFIND algorithm (Springel et al., 2001; Dolag et al., 2009).

2.3 Millenium TNG simulation

Millenium TNG is a follow-up of the successful model of IllustrisTNG. It uses essentially the same physical model, but in a 15-time larger volume than the largest IllustrisTNG simulation. The MilleniumTNG suite consists of one hydrodynamical simulation and several DM-only simulations, all of which share the same box size but vary in the number of DM particles. The suite also includes a series of DM-only runs that incorporate massive neutrinos. This suite is designed to investigate baryonic physics on large scales, such as galaxy clusters and the cosmic web (Pakmor et al., 2023). In this thesis, specifically in chapter 5, we use the flagship hydrodynamical simulation of the suite, hereafter MTNG. MTNG was run with a periodic box of 750 Mpc per side using 4320^3 DM particles and an identical number of gas cells. MTNG has a mass resolution of 1.7×10^8 $M_\odot$ in dark matter and $3.1 \times 10^7 M_\odot$ in gas cells (Hernández-Aguayo et al., 2023; Pakmor et al., 2023), with a softening length of $\varepsilon = 370 pc$. The galaxy formation physics model and the cosmological parameters of MTNG are essentially the same as the one used in IllustrisTNG. The MTNG box is 15 times larger in volume than TNG300, allowing us to have a sample of 9 galaxy clusters with masses larger than 1×10^{15}, 1500 galaxy clusters with masses larger than 10^{14} $M_\odot$, and 38000 clusters with masses larger than 10^{13} $M_\odot$ at redshift $z = 0$, all maintaining a mass resolution comparable to TNG300.

2.4 Physics model

The IllustrisTNG and MTNG simulations include inhered models from the Illustris simulations that incorporate nonlinear physical processes driving galaxy formation and evolution, such as star formation, stellar evolution, chemical enrichment, and gas recycling (Vogelsberger et al., 2014; Gene et al., 2014; Sijacki et al., 2015). Illustris TNG also has updated models for the growth and feedback of supermassive black holes, galactic winds, and metal abundance evolution (Weinberger et al., 2017; Pillepich et al., 2018a).

The star formation model in the IllustrisTNG and MTNG simulations is based on the multiphase interstellar medium (ISM) sub-grid model developed by Springel & Hernquist (2003). In this model, star formation occurs in dense gas regions, where the gas is treated as a two-phase medium consisting of cold clouds embedded in a hot, diffuse component. Star formation is triggered when the local gas density exceeds a critical threshold of 0.1 hydrogen atoms per cubic centimetre. In this regime, star formation occurs stochastically, assuming a Chabrier (2003) initial mass function (Pillepich et al., 2018a). Once stars form, they evolve according to the stellar population models. This includes the return of gas and metals to the surrounding medium through Type II and Type Ia supernovae and winds from the asymptotic giant branch (AGB) stars. The feedback from these processes injects energy, momentum, and metals back into the ISM, driving turbulence, heating the gas, and regulating further star formation. IllustrisTNG tracks the chemical abundances of the nine most important elements: H, He, C. N, O, Ne, Mg, Si, and Fe individually. In contrast, MTNG only traced the total metal abundance.

In the IllustrisTNG and TNG models, supermassive black holes (SMBHs) form in sufficiently massive halos and influence their surroundings through feedback mechanisms as they accrete gas. The model distinguishes between two modes of feedback based on the SMBH accretion rate. At low accretion rates (radio mode), with an accretion rate below 5% of the Eddington rate, a kinetic mode is activated, where energy is injected through momentum-driven winds. This feedback operates in a more continuous manner and is primarily responsible for regulating gas accretion in massive galaxies. In contrast, at higher accretion rates, typically corresponding to quasar mode, thermal energy is injected into the surrounding gas, heating the immediate environment (Springel, 2005). This process limits star formation by expelling or heating gas in the central regions of galaxies (Pillepich et al., 2018a). The complete description of the Illustris TNG physics model can be found in the simulation presentation papers by Pillepich et al. (2018a), and Vogelsberger et al. (2018).

2.5 IllustrisTNG Main Results

The IllustrisTNG simulations reproduce notably well several observed statistical properties of the galaxy population. These properties include the galaxy mass function from redshift $z = 4$ to $z = 0$ (Pillepich et al., 2018b), the clustering of galaxies as a function of stellar mass, colour, star formation, and redshift (Springel et al., 2018), the cosmic star formation rate density (Springel et al., 2018), the galaxy colour bimodality (Nelson et al., 2019), the galaxy morphologies (Rodriguez-Gomez

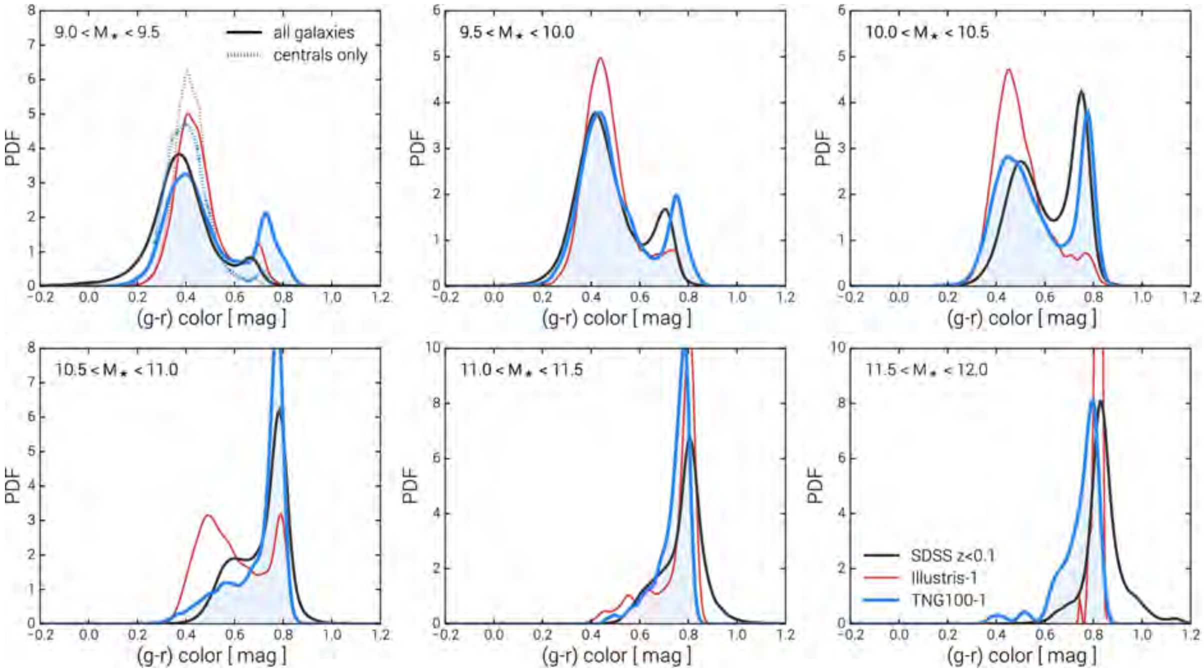

Figure 2.5.1: The distribution of simulated versus observed (g-r) colours. In black, the SDSS sample $z < 0.1$ is shown, while red shows the result from the old Illustris simulation, and blue the result from our new TNG100 simulation of equivalent box size and resolution. In all cases, galaxies with stellar masses from 10^9 to 10^{12} $M_\odot$ are included, divided into six mass bins as indicated in the six panels. Figure taken from Nelson et al. (2018)

et al., 2019), the gas content of the galaxies (Donnari et al., 2019), and the galaxy quenched fraction (Donnari et al., 2021), among others. In this section, we will describe the most important properties for this thesis.

2.5.1 Galaxy colour distribution

Galaxy colours are sensitive indicators of both the star formation rate and the metallicity of the stars. By incorporating a detailed description of chemical enrichment into simulations, researchers can compare predicted and observed properties of cluster galaxy populations more accurately. Hydrodynamical simulations address star formation by converting cold, dense gas particles into collisionless star particles, which are then treated as single-age stellar populations. To analyse galaxy populations in simulations, luminosities in various bands are computed using stellar population synthesis models. Galaxies are identified as gravitationally-bound groups of star particles through group-finding algorithms, and their luminosity and colours are determined by summing the luminosities of individual star particles. Figure 2.5.1, presented in Nelson et al. (2018), compares the simulated galaxy colour distributions with observations from the Sloan Digital Sky Survey (SDSS DR12) sample, which includes 378,287 galaxies with spectroscopic redshifts $z < 0.1$ (Alam et al., 2015). The observed galaxies display a well-known bimodality in colour, with lower-mass galaxies being predominantly blue ($g - r \sim 0.4$), while red galaxies ($g - r \sim 0.8$) become increasingly dominant as stellar mass increases. This transition is particularly evident around $M_* \simeq 10^{10.5}$ $M_\odot$, where the blue and red populations are roughly equal. At higher masses, blue galaxies disappear, leaving the red population as the dominant type. The TNG100 simulation replicates this observed bimodal distribution with high accuracy, especially for galaxies with stellar masses below 10^{11} $M_\odot$, where the positions of the blue and red peaks and their relative amplitudes align well with the SDSS data. However, TNG100 shows a slight discrepancy at the low-mass end ($M_* < 10^{9.5}$ $M_\odot$), producing an excess of red satellite galaxies. These low-mass red systems may result from limited resolution; increasing resolution tends to shift these galaxies toward bluer colours. Despite this tension, the overall agreement between the simulation and observations underscores the success of TNG100 in reproducing the galaxy colour bimodality across a wide range of stellar masses.

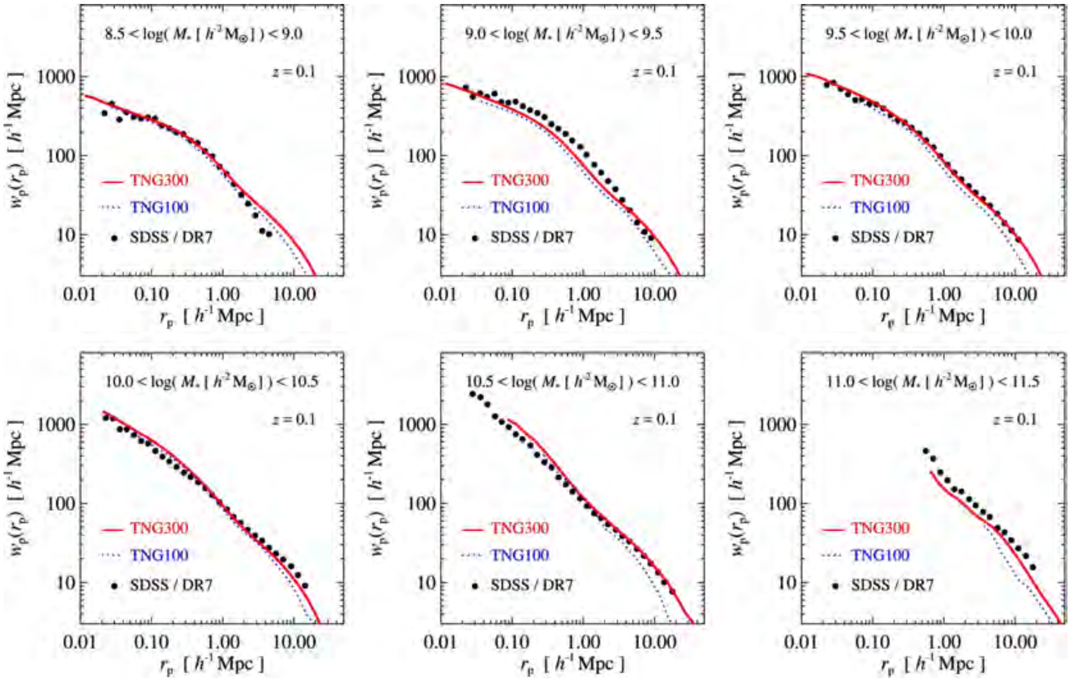

Figure 2.5.2: Comparison of the projected two-point galaxy correlation functions of TNG300 (solid) and TNG100 (dotted) at $z = 0.1$ to the SDSS in six different stellar mass ranges. The data are taken from Guo et al. (2011). Overall, the agreement is remarkably good. Figure taken from Springel et al. (2018).

2.5.2 Galaxy Clustering

The TNG300 simulation offered new insights into the clustering of galaxies across a large volume. Figure 2.5.2 presented in Springel et al. (2018) shows the projected correlation functions of galaxies in TNG300 at redshift $z \sim 0.1$. These correlation functions align well with observational data from the Sloan Digital Sky Survey (SDSS), as compiled by Guo et al. (2011, 2010). The simulation shows excellent agreement with SDSS across six stellar mass bins. TNG300 and TNG100 show strong general agreement, with the exception of large scales around $r \sim 10\,h^{-1}$ Mpc, where TNG100 shows a noticeably lower clustering amplitude. This discrepancy is expected due to the smaller box size of the TNG100. Additionally, in the highest stellar mass range, TNG100 contains too few galaxies to reliably compute the correlation function at small separations. The overall agreement of galaxy clustering in TNG300 highlights its success in capturing large-scale structures, making it one of the most accurate hydrodynamic simulations in this regard (Artale et al., 2017).

Springel et al. (2018) also present the clustering of galaxies separating between red and blue galaxy populations. The agreement with the clustering of blue galaxies with observations is excellent across nearly all stellar masses. However, the clustering of red galaxies is slightly overestimated at intermediate stellar masses. Overall, the level of agreement with the available data is encouraging, indicating that the quenching mechanisms in our hydrodynamical simulations are broadly successful in reproducing the observed clustering of red and blue galaxies and their dependence on stellar mass.

2.5.3 Fraction of quenched galaxies

Figure 2.5.2, presented by Donnari et al. (2021), shows the fraction of quenched galaxies compared to the observational data. At low redshift ($z = 0.1$), the agreement between simulations and observations is strong, especially for low-mass and high-mass central galaxies. The quenched fractions of massive centrals align well with surveys like SDSS and SAMI, where less than 5% of low-mass centrals are quenched (Wetzel et al., 2013; Lin et al., 2014). For massive centrals, TNG simulations reproduce the observed quenched fractions in the range of 80-90%, especially in higher stellar mass regimes (Donnari et al., 2021). The results for satellite galaxies, particularly those with high stellar masses, also exhibit reasonable agreement with Wetzel et al. (2013) and Mcgee et al. (2011).

At intermediate redshifts ($z = 0.35$), the quenched fractions of both centrals and satellites are systematically lower in the TNG model compared to observational results. In particular, the differences are important when compared to data sets such as that in Jian et al. (2018), which show a discrepancy of up to 40 percentage points for the centrals and a similar gap for the satellites. These discrepancies may result from variations in the way galaxies are classified in different surveys. For example, observational surveys such as Lin et al. (2014) and Jian et al. (2018) often classify galaxies based on group richness, whereas TNG adopts different classification methods, leading to significant inconsistencies, especially in low-mass regimes.

At higher redshifts ($z = 0.65$), the simulations are in better agreement with some observational data for massive centrals, where the quenched fraction in TNG is consistent with Lin et al. (2014), and Jian et al. (2018). However, there remains an offset when compared to the 3DHST/CANDELS data, with the TNG model predicting a lower quenched fraction for low-mass galaxies and a higher one for massive galaxies (Donnari et al., 2021).

2.6 MilleniumTNG Main Results

Millennium TNG is a recent simulation that is not yet publicly available, which limits the number of studies analyzing its results. Nevertheless, because the physics model closely mirrors that of IllustrisTNG, MTNG is expected to reproduce all the key features of the galaxy distribution observed in IllustrisTNG. Bose et al. (2023) compared galaxy clustering in MTNG with SDSS data, showing agreement with observations. They also examined the clustering of red and blue galaxies separately. Although the clustering of blue galaxies aligns well with observations, MTNG740 overpredicts the clustering of red galaxies,particularly in objects in a mass range $9.5 \leq \log(M/M_{\odot}) \leq 10.5$, an issue not observed in the semi-analytic model of the MillenniumTNG suite.

MTNG740 provides valuable insight into galaxies' intrinsic alignment (IA). The IA refers to the non-random orientations or shapes of galaxies that are correlated with the large-scale cosmic structures in their environment. This phenomenon occurs due to the gravitational influence of the surrounding matter (both dark and baryonic) on the galaxies, causing their shapes to align with the cosmic web's tidal fields, including the dark matter haloes, filaments, and voids. This can be directly quantified by measuring their intrinsic ellipticities. In Delgado et al. (2023), the IA signals were detected by measuring the projected correlation functions between galaxy shapes and various tracers of large-scale structure. Significant IA signals were found for both elliptical and spiral galaxies. For elliptical galaxies, the signal was strongest and well-detected across different redshifts ($z = 0.0$, 0.5, and 1.0), while a weaker signal was observed for spiral galaxies, in line with the predictions of a quadratic tidal torquing model. In Figure 2.6.1, taken from Delgado et al. (2023), we can see that the IA signals in MTNG align closely with low-redshift data from the SDSS-III BOSS survey (Singh et al., 2015), showing similar amplitudes and shapes in the IA correlation functions. They also showed that the MTNG740 is consistent with recent measurements from the KiDS survey (Fortuna et al., 2021), particularly for luminous red galaxies, demonstrating that the simulation is able to reproduce the observed IA features with high accuracy.

However, MTNG also has caveats, such as the inability to account for the unexpectedly high abundance of high-redshift ($z \geq 8$) luminous galaxies recently observed with JWST (Kannan et al., 2023). This suggests that while MTNG can reproduce many internal properties of galaxies, several processes are not fully understood.

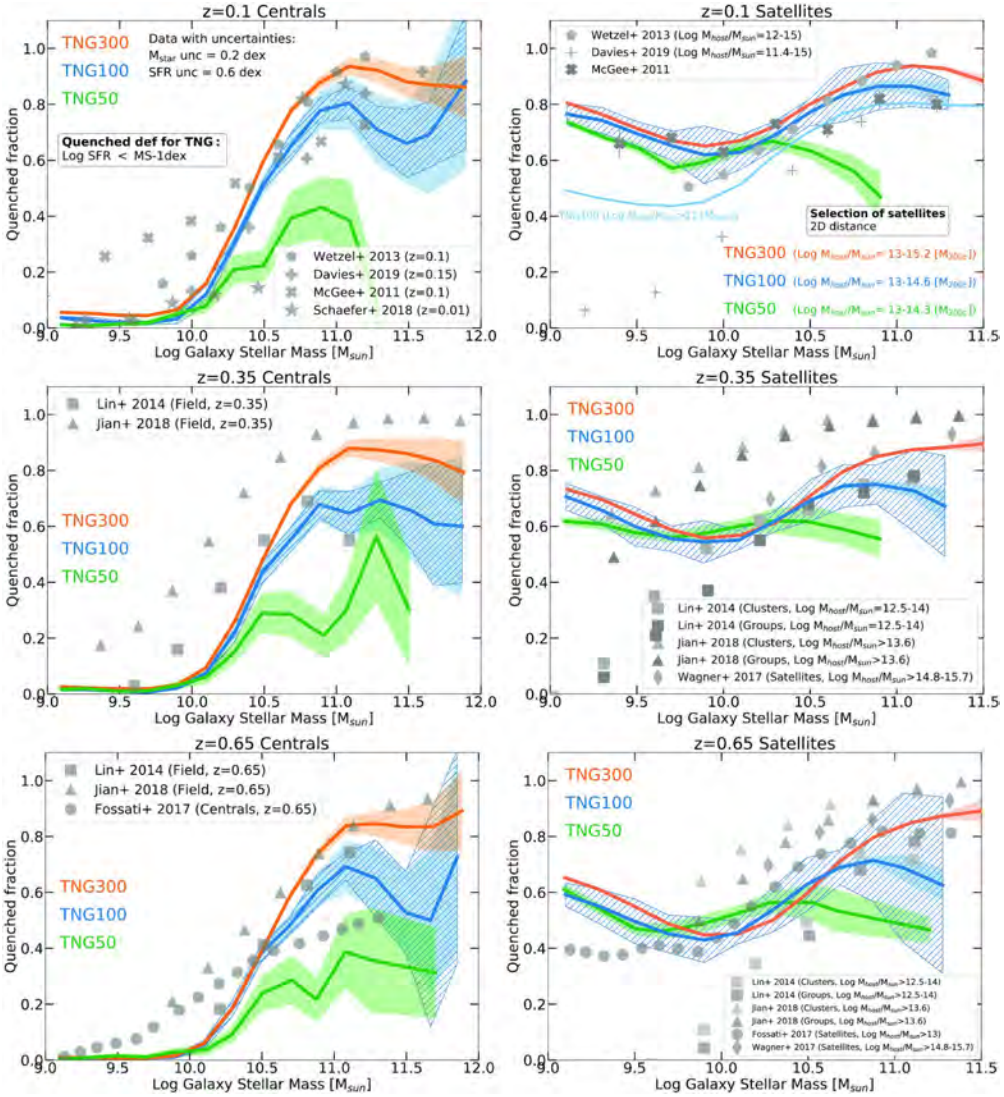

Figure 2.5.3: Quenched fractions in TNG100 (blue), TNG300 (orange), and TNG50 (green) for central galaxies (left column) and satellites (right column) at $z = 0.1$ (top), $z = 0.35$ (middle), and $z = 0.65$ (bottom). Shaded areas represent the Poissonian errors, while the striped areas around TNG100 represent the cosmic variance uncertainties. They compared the results with the quenched fractions obtained from different observational data sets. Overall, the TNG quenched fractions are qualitatively (and often, quantitatively) in good agreement with observations as a whole, although discrepancies are visible in certain regimes. Figure taken from Donnari et al. (2021).

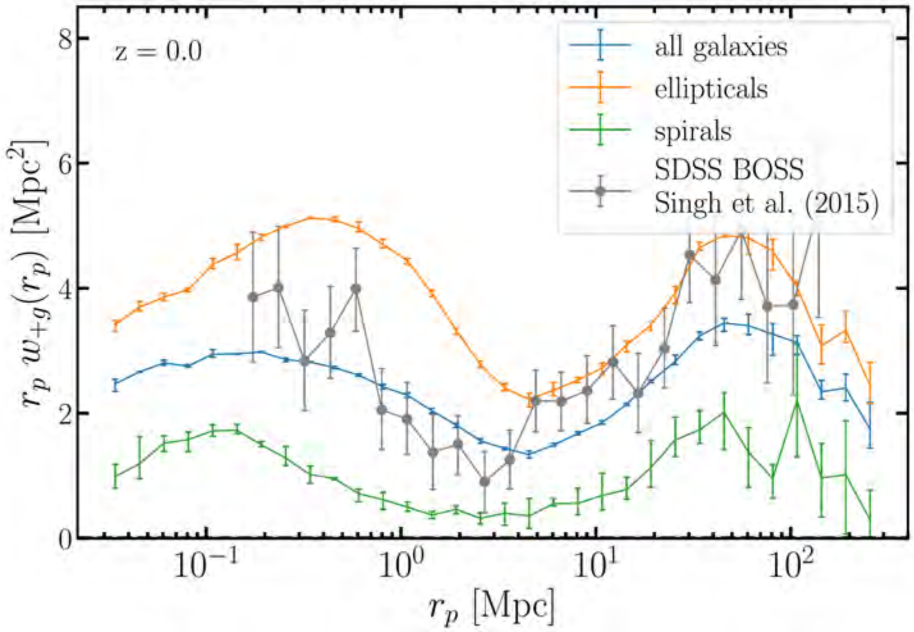

Figure 2.6.1: Projected cross-correlations of the intrinsic galaxy shear with galaxy positions, $w_{\rm p}^{+g}(r_{\rm p})$, at redshift $z = 0$. The correlations are shown separately using the shapes of the subsamples of elliptical and spiral galaxies, as well as for all galaxies. At the same time, the density field is always sampled by using all galaxies as unweighted tracers. Figure taken from Delgado et al. (2023).

Chapter 3

The Impact of Cluster Mergers in the Red Sequence.

Abstract

Merging of galaxy clusters are some of the most energetic events in the Universe, and they provide a unique environment to study galaxy evolution. We use a sample of 84 merging and relaxed SPT galaxy clusters candidates, observed with the Dark Energy Camera in the $0.11 < z < 0.88$ redshift range, to build colour-magnitude diagrams to characterise the impact of cluster mergers on the galaxy population. We divided the sample between relaxed and disturbed, and in two redshifts bin at $z = 0.55$. When comparing the high-z to low-z clusters we find the high-z sample is richer in blue galaxies, independently of the cluster dynamical state. In the high-z bin we find that disturbed clusters exhibit a larger scatter in the Red Sequence, with wider distribution and an excess of bluer galaxies compared to relaxed clusters, while in the low-z bin we find a complete agreement between the relaxed and disturbed clusters. Our results support the scenario in which massive cluster halos at $z < 0.55$ galaxies are quenched as satellites of another structure, i.e. outside the cluster, while at $z \geq 0.55$ the quenching is dominated by in-situ processes. [1]

---

[1] Based on Aldás, Zenteno, Gómez, et. al., 2023, published in MNRAS.

3.1 Introduction

Galaxy clusters are the largest collapsed gravitationally bound structures of the Universe and typically contain hundreds or thousands of galaxies (Voit, 2005; Abell, 1958). These clusters have grown to their present-day mass through the merger and accretion of neighbouring substructures. Galaxy clusters can be found in different dynamical states. In a relaxed cluster, the Intra-Cluster Medium (ICM) is generally close to thermodynamic equilibrium. However, in clusters colliding with other massive structures, the released binding energy of the systems results in the heating of their ICM (Sarazin, 2001). Cluster mergers are the most energetic events after the Big Bang and can emit energies up to 10^{64} erg (Sarazin, 2004; Kravtsov & Borgani, 2012). Indeed, observations at different wavelengths suggest that a significant fraction of clusters are not fully virialized but are interacting with other ones or still collapsing(Dressler & Shectman, 1988; Hou et al., 2012; Zhang et al., 2009; Andrade-Santos et al., 2017). Such energetic cluster merging events can trigger and/or quench star formation in their galaxy members, thus affecting their observable properties such as colours.

The dynamical state of galaxy clusters is described using different observational proxies. Among them we find the central cooling time (Bauer et al., 2005), the concentration index which is the excess of the surface brightness in the central part of the cluster measured in X-rays (Santos et al., 2008; Yuan et al., 2022), the displacement between the cluster X-ray surface brightness peak from its surface brightness centroid (Cassano et al., 2010; Yuan et al., 2022), and combinations of different observations such as the offset between the position of the brightest cluster galaxy (BCG) and the Sunyaev-Zeldovich (SZ) centroid (Zenteno et al., 2020). Additionally, some quantities can be used to study the dynamical state using cosmological simulations, for example, the virial ratio η based on the virial theorem that measures the degree of deviation that a cluster has from an equilibrium state, the fraction of mass of the cluster contained in subhalos with respect to its total mass, and the offset between the centre of mass of cluster with the cluster centre, or a weighted combination of these parameters (Zhang et al., 2022).

Today, a significant fraction of the members inhabiting these clusters consist of elliptical and lenticular galaxies (Hubble & Humason, 1931; Oemler & Hale Observatories, 1974; Dressler, 1980). These early-type galaxies feature a well-defined linear relation between their colour and magnitude (Visvanathan & Sandage, 1977; Bower et al., 1992; Kodama & Arimoto, 1996), the so-called red sequence (RS). Such galaxies in the cluster RS have null or little ongoing star formation (Gladders & Yee, 2005; Gladders et al., 2007; De Propris et al., 2016), and their colour evolution can be remarkably well described by simple evolutionary models (Stanford et al., 1998). In fact, such models are so successful that they have been used to identify clusters (Gladders & Yee, 2000; Murphy et al., 2012; Bleem et al., 2015; Rykoff et al., 2016) and to provide robust photometric redshifts up to z $\sim$ 1.5 (e.g. Song et al., 2012; Bleem et al., 2015, 2020), with a precision better than z $\sim 0.01 \times (1+z)$ up to z $\sim$ 1.0 (e.g. Rykoff et al., 2016; Klein et al., 2018, 2019). While the slope and zero-point evolution of the RS describes the aging of galaxies' stars formed at $z \sim$2 - 3 (at least up to z $\sim$1.3, e.g., Mancone et al., 2010), the scatter provides information about its stellar population age diversity (Connor et al., 2019).
Previous studies have shown that the scatter remains relatively constant up to z $\sim$1 (e.g. Jaffé et al., 2011; Hennig et al., 2017). However, at $z \gtrsim 1.3$, the RS is found to be wider and bluer, indicating that at such z clusters are approaching their star formation epoch (Hilton et al., 2009; Papovich et al., 2010; Snyder et al., 2012). Furthermore, Brodwin et al. (2013) suggest that $z \sim 1.4$ could be where clusters star formation activity ends and the era of passive evolution begins.

Previous works have studied the differences in the star formation rates of galaxies in disturbed clusters concerning their relaxed counterparts. Yet, there is no agreement about whether a galaxy's star formation rate is stimulated or suppressed during large merger events. For example, Pranger et al. (2014) through an analysis of the galaxy population in Abell 3921, and Kleiner et al. (2014) in A1750, found that mergers quench star formation. Shim et al. (2011) also studied the interacting cluster A2255, finding that the merging process suppresses star formation and transforms galaxies into quiescent galaxies. However, other authors such as Ferrari et al. (2003), by an spectroscopic analysis of Abell 521, and Owers et al. (2012) by studying the cluster Abell 2744 (which is currently undergoing a major merger) found that the high-pressure merger environment triggers star formation. In support of this, Sobral et al. (2015) and Yoon & Im (2020) found that the star formation rate in the interacting clusters is around 20% higher than the observed in relaxed structures. Such findings are confirmed using Hα observations of disturbed and relaxed clusters at $z < 0.4$ finding a higher prevalence of Hα emitter galaxies in disturbed clusters, within 2 Mpc from the cluster's center, than in relaxed clusters (Stroe et al., 2017; Stroe & Sobral, 2021). In the same way, Hou et al. (2012) studying groups of galaxies at intermediate redshifts ($z \sim 0.4$) show that galaxies in groups with substructures present a significantly higher blue galaxies population compared to galaxy groups with no detected substructures.

The goal of this work is to study the impact that the merging of clusters has on their red galaxy population. We compare the cluster galaxies RS of a sample of 84 clusters, both relaxed and disturbed, all within a wide redshift range between $0.11 \leq z \leq 0.88$. The cluster sample was first introduced in Zenteno et al. (2020). This Chapter is organised as follows: in § 3.2 we provide details of the observations and data reduction. In § 3.3 we show the data calibration between DES and Munich pipeline reductions, while in § 3.4 we report our findings. Finally in § 3.5 are our conclusion. Throughout this Chapter, we assume a flat Universe, with a ΛCDM cosmology, $h = 0.7$, $\Omega_M = 0.27$ (Komatsu et al., 2011).

3.2 Data

The observations used in this work were carried out with the Dark Energy Camera (DECam; Flaugher et al., 2015), a 570 Mega-pixels CCD, installed at the prime focus of the V. M. Blanco 4-meter Telescope at Cerro Tololo Inter-American Observatory (CTIO). The DECam has a field-of-view of 2.2°. We use two sets of data; 65 clusters ($0.11 \lesssim z \lesssim 0.65$) comes from the Dark Energy Survey public second data release (DES; DES-Collaboration et al., 2021), while for 19 clusters at $z \gtrsim 0.65$ we use archival data as well as data obtained using Director Discretionary Time (DDT). DDT was pooled with the DECam eROSITA Survey (DeROSITAS; PI Zenteno) allocation, taking advantage of the flexibility a large pool of nights provide to programs with different needs.

DES is a 5000 square degree optical survey using the DECam and 5 filters `g,r,i,z,Y`, covering a wavelength range from 400 nm to 1065 nm. The Data Release 2 (DR2) of DES is the result of six years of observations (2013-2019) collecting information of around 700 million galactic and extragalactic sources (DES-Collaboration et al., 2021). The image reduction and processing for the DES sample set was done by the DESDM system. This process performs flat-fielding, bad-pixel masking, overscan removal, masking of cosmic rays and artificial satellites, and other image corrections (Morganson et al., 2018). Once the images are fully reduced, the pipeline performs a fitting with PSFEx and source detection using Source Extractor generating the co-added images and its associated source catalogues that are ready for science analysis (DES-Collaboration et al., 2021; Bertin, 2011; Bertin & Arnouts, 1996). We retrieved the source catalogues from the DES DR2 repository. The downloaded parameters are: `MAG_AUTO`, `MAGERR_AUTO`, `FLAGS`, `IMAFLAGS_ISO`, and `SPREAD_MODEL` for each g, r, i, z bands. `MAG_AUTO` are the magnitude estimations using an elliptical model considering the Kron radius, with `MAGERR_AUTO` their uncertainties (Kron, 1980). `FLAGS` store additive flags indicating potential problems in the source extraction process, and `IMAFLAGS_ISO` are flags where sources have missing / flagged pixels in their single epoch images. Finally, `SPREAD_MODEL` is a parameter to identify extended sources comparing the fit quality between the local point-spread function (PSF) and an extended circular exponential disk (Desai et al., 2012; DES-Collaboration et al., 2021). The limiting magnitudes of the DES (DR2) for the selected clusters, at 10σ are $g \sim 23.7$, $r \sim 23.7$, $i \sim 23.0$, and $z \sim 22.27$ mag.

3.3 Catalogues

DeROSITAS is a survey designed to complement the German sky of the eROSITA survey (Merloni et al., 2012) in the optical wave range. DeROSITAS was performed using DECam in filters g, r, i, and z, reaching minimum depth of 22.7 (23.5), 23.2 (24.0), 23.3 (24.0), 22.5 (23.2) AB magnitudes at $10(5)\sigma$. DeROSITAS observing strategy consisted in filling the sky, avoiding archival data when at sufficient depth, and carrying out observations in coordination with other current surveys, such as DELVE (Drlica-Wagner et al., 2021), to avoid duplication. During DeROSITAS nights, high-z clusters observations were triggered when the seeing and the effective time $t_{\rm eff}$ (H. Neilsen, Jr. et al., 2016) were better than average (seeing better than ∼1.0” and $t_{\rm eff} > 0.4$). The $t_{\rm eff}$ is a scale factor to be applied to the open shutter time to reflect the quality of the observations compared to good canonical conditions. These good conditions are defined as observations with a FWHM of 0.9” and sky brightness obtained when pointing the telescope to the zenith under dark conditions.

The DeROSITAS observations used here reach magnitudes $i \sim 23.9$, and $z \sim 23.6$, which is between 0.9 and 1.3 magnitudes deeper than DES (we used just those bands because those observations are focused in high-redshift clusters). The data reduction was done using a pipeline similar to DESDM (Desai et al., 2012), where the steps are done by first building single epoch

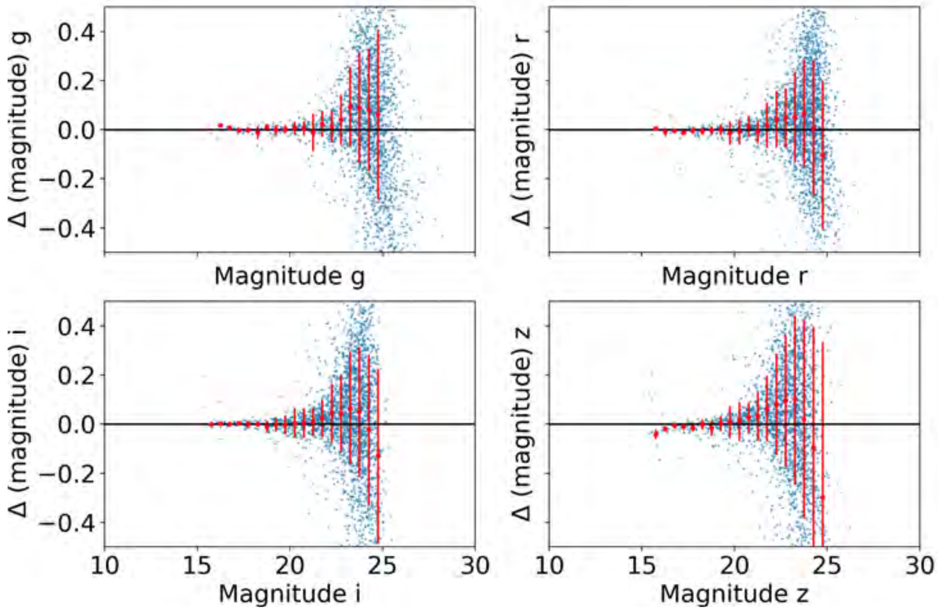

Figure 3.3.1: Example of the difference between magnitudes measured by DES and *high-z clusters*, in each used filter for stars detected in the field of the cluster SPT-CLJ0310-4647, located at $z = 0.710$ after the SLR correction. The red dots is the average difference between those MAG_AUTO and the error bars correspond to the standard deviation of the differences.

(SE) images and then using a co-adding pipeline. The single epoch pipeline groups the observations according to the observation night and then, for each DECam observation that contributes to the cluster area (within 1×1 deg^2 from the SPT position), it constructs $\sim$62 (one for each CCD) photometrically flattened, astrometrically calibrated single SE images, together with position variable PSF models and PSF corrected model fitting catalogs. The processing includes overscan and bias correction, flat-fielding, initial astrometric calibration and PSF corrected model fitting photometry using PSFex. The final astrometric and photometric calibrations for each SE image are done using Gaia DR2 (Evans et al., 2018) photometry data (for details refer to George et al., 2020). Finally, the coadd pipeline works similar to the DES processing, generating PSF homogenised COADD images and catalogues by using a combination of SourceExtractor and PSFex software. The final *high-z clusters* sample is presented in Table 3.7.1, and the DES cluster sample is presented in the Table 3.7.2.

As we mentioned, we have two sets of data. The first comes from the DES DR2 database public repository, and the second, with deeper photometry, comes from our own reductions. Following the catalogues calibration described in the preceding section, hereafter we will create the final sample joining both catalogues in the following way: 65 clusters from DES described in Table 3.7.2 at $0.1 < z < 0.65$ (henceforth the *DES clusters* sample), and the 19 clusters from DeROSITAS at redshift higher than 0.65 (henceforth the *high-z clusters* sample) detailed in Table 3.7.1. As those two catalogues were obtained from two different pipelines, we expect slight differences. To reduce such photometric differences we correct the colour of both catalogs using the Stellar-Locus-Regression (SLR) technique High et al. (2009). Once the colour is corrected we adjust the zeropoint by adopting the DES zeropoint for the *high-z clusters* catalogs. The process is outlined below:

First, we calibrated the colours $g-r$, $g-i$, $r-i$, and $i-z$ for both sets of data using the SLR code. This technique uses a region in the colour-colour diagram populated by stars (Covey et al., 2007; Ivezić et al., 2007). The SLR code accurately calibrates the colours for stars and galaxies using catalogued flat-fielded images without having to measure standard stars or determining the zero-points for each pass-band. The SLR technique also corrects for differences in instrumental response, atmospheric response, and galactic extinction. As input, the SLR code needs magnitudes, magnitudes errors, and extinction value for every source in each passband used (g, r, i, z). The dust extinction were obtained using the Schlafly & Finkbeiner Dust (Schlafly & Finkbeiner, 2011; Schlegel et al., 1998). Colour correction was made considering objects classified as stars. The photometric catalogues include the `SPREAD_MODEL` parameter, which is a star-galaxy separator. Following the same crite-

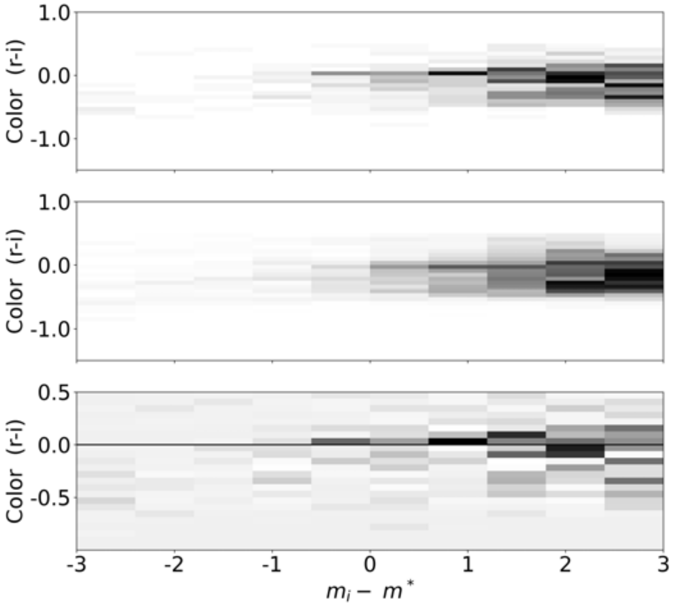

Figure 3.3.2: Background correction process for the cluster SPT-CLJ0253-6046. On the top panel, we have the detected objects inside the virial radius R_{200}. In the middle panel, the objects found in the background, located in the annulus between $1.5-3R_{200}$. Finally, in the bottom panel, the Red Sequence of the cluster computed as the overdensity corrected by the background. The three panels were plotted after performing the redshift slope correction for the RS time evolution. The used bins for the CMDs have a size of 0.6 in magnitude and 0.06 in colour.

ria used by Hennig et al. (2017), we consider as stars the sources with `SPREAD_MODEL < 0.002`. We clean the final sample by excluding sources with `IMAFLAGS_ISO > 0` in all bands to avoid saturated objects and objects with missing data (Morganson et al., 2018) and `FLAGS` $\geq$ `4`, to include deblended sources but excluding sources flagged with warnings during the extraction process (DES-Collaboration et al., 2021).

As a result of the SLR calibration, we obtained corrected colours for stars and galaxies for the DES and *high-z clusters* catalogs. Next, we correct the absolute magnitude of the *high-z clusters* catalogues by comparing its star's magnitudes to the DES star magnitudes for the $i-$band. We used a 0.25 arcseconds to match stars and a 0.5 magnitude difference to avoid variable stars. Once such correction is found (which has an average value of ~ 0.02 magnitude), we applied the correction to all objects in the *high-z clusters* catalogue.

As an example of the results of the calibration process, in Figure 3.3.1 we present four diagrams, one for each band (g, r, i, z) for the catalogues corresponding to the cluster SPTCLJ0310-4647. In those diagrams, each point corresponds to a Milky-Way star detected in the field of view of the cluster, present in both DES and DeROSITAS catalogues. Stars were selected by `SPREAD_MODEL < 0.02`). In the x-axis, we show the magnitude (MAG_ AUTO) corresponding to the DES catalogue (taken as a base to calibrate the high-redshift data set),meanwhile in the y-axis we have the $\Delta(magnitude)$ defined as the difference between DES and *high-z clusters* MAG_AUTO. Similar plots were obtained for the 19 clusters in common. We can see that the differences in magnitude for DES and *high-z clusters* observations are close to zero for the brightest end. The maximum mean difference for the brightest stars (mag < 20.5), between the two catalogues, computed as the average difference between the DES and DeROSITAS magnitudes, is around 0.04 mag in all four bands. This result suggests that the fluxes obtained using both pipelines are very close to each other and, thus, we can consider them as equivalents.

Table 3.3.1: Bands used for the colour- magnitude diagram depending on the cluster redshift to capture the 4000 Å Balmer break.

Redshift	color bands	magnitude band
$0 < z \leq 0.33$	(g-r)	r
$0.33 < z \leq 0.74$	(r-i)	i
$0.74 < z \leq 0.9$	(i-z)	z

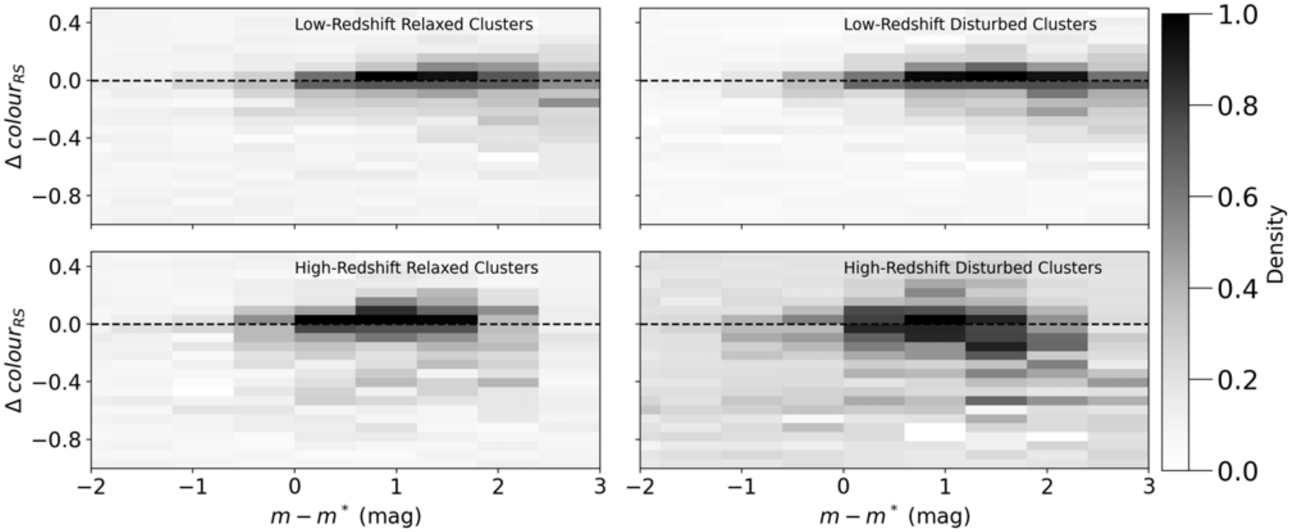

Figure 3.4.1: Colour magnitude diagram of galaxies for each studied clusters subsets. In the top row we have the low -redshift $(z < 0.55)$ relaxed (left) and disturbed clusters (right) and in the bottom row we have the relaxed (left) and disturbed (right) clusters for the high redshift bins $(z > 0.55)$.

3.4 Results

The goal of this Chapter is to study the differences in the cluster RS galaxy population as a function of the cluster dynamical state. A galaxy spectrum is mostly flat and is mainly composed of a combination of blackbody emitters, but there is a noticeable break at 4,000 Å in the rest frame where there is an absorption of high energy radiation in the stellar atmospheres in metal-poor populations (Mihalas, 1967a; Poggianti & Barbaro, 1997). This break allows to separate blue from red galaxies (Poggianti & Barbaro, 1997). For this reason, we used two photometric bands that contain the Balmer break in the rest frame. In those filters, the elliptical galaxies tend to be redder than normal galaxies at any lower redshift, thus becoming easily noticeable from the background (Gladders & Yee, 2000). Then, the selected bands depend on the redshift of each cluster, and are presented in the Table 3.3.1.

To construct a cluster colour-magnitude diagram (CMD), we consider galaxies within R_{200} as cluster galaxies and galaxies in the annulus between $1.5 \times R_{200} < r < 3 \times R_{200}$ as background. Where R_{200} is defined as the radius where the cluster density is 200 times the critical density of the Universe at a given redshift. The cluster centers corresponds to the SPT-SZ centers (Bleem et al., 2015), and the R_{200} were estimated by Zenteno et al. (2020) using the estimated M_{500}, and the Duffy mass-concentration relation (Duffy et al., 2008). We bin both the cluster and background CMDs, using bins of 0.6 in magnitude and 0.06 in colour, and perform a statistical background subtraction to correct for contamination due to the projection effects.

Once the background-subtracted CMD is built for each cluster, we use a stellar population synthesis model to stack them. We do this by using models with an exponential starburst decay and a Chabrier IMF (Bruzual & Charlot, 2003) for six metallicities

Table 3.4.1: Number of clusters in the used sample in each analyzed group. We divided the sample between low and high redshift samples and relaxed and disturbed clusters.

Redshift range	Relaxed clusters	Disturbed clusters
$0.1 < z < 0.55$	16	27
$0.55 \leq z < 0.9$	25	16

described in Song et al. (e.g., 2012), and Zenteno et al. (2016).
Using the cluster's redshift, and following the procedure described by Hennig et al. (2017), we obtain the model (expected) cluster RS slope as a function of the magnitude and then subtract it from the observed slope, bringing the cluster's colour slope to zero. The model also provides the characteristic magnitude defining the knee of the luminosity function, m^*, for each filter and redshift. The cluster redshift used in this work corresponds to the same as Zenteno et al. (2020), which are photometric and spectroscopic redshifts collected from several literature sources.
In Figure 3.3.2, we show the process of the background correction for the SPT-CLJ0253-6046 galaxy cluster, located at $z = 0.45$. For this cluster we used the r and i bands. In the horizontal axis we have the magnitude $(m_i - m^*)$, with m^* obtained from the model. The three vertical axes show the $r-i$ colour. In the top panel, we show the density of objects within the virial radius, plotted in gray scale. The middle panel focuses on objects located between 1.5 to 3 viral radius. Finally, in the bottom panel we show the resulting red sequence, obtained after subtracting the number object in the background from the number of objects within R_{200}, normalized by their areas.

We then combined the cluster CMDs by adding all background-corrected numbers of galaxies, normalised by the total number of clusters used in each bin. De Propris et al. (2016) studied the evolution of galaxies as they experience gravitational infall into cluster cores during merging processes, resulting in a transformation of the cluster RS (red sequence) morphology, as previously observed by De Lucia et al. (2007); Stott et al. (2007). The RS evolution below $z \sim 0.5 - 0.6$ shows that there are little or no morphological changes in the galaxy population, unlike earlier in time. For this reason, we separated the cluster sample into two redshift bins: the first one includes clusters between $0.1 < z < 0.55$ (low redshift bin) and the second one includes clusters with redshifts between $0.55 \leq z < 0.9$. Additionally, we subdivided our cluster sample according to their dynamic state. As a result, we have four subgroups of clusters: disturbed and relaxed clusters at low and high redshifts. The number of clusters in each subgroup is presented in Table 4.3.1. It should be noted that we have at least 16 clusters in each subgroup.

The dynamical state of the clusters used in this Chapter was estimated by Zenteno et al. (2020). They classified between relaxed and disturbed clusters using four different proxies: The offset between the position of the BCG and the SZ centroid (D_{BCG-SZ}), the core temperature, the morphological parameter(A_{Phot}), which measures the asymmetry of the X-ray emission, and the offset between the BCG and the peak of X-ray emission. In this analysis, a cluster is defined as relaxed if it met any of the following three conditions: i) the cluster has $A_{phot} < 0.1$, ii) the cluster has a cool core ($K_0 < 30$ keV cm^2) (McDonald et al., 2013), or iii) the offset between BCG and X-ray peak is less than 42 kpc (Mann & Ebeling, 2012). Meanwhile, the clusters were classified as disturbed if the offset between the position of the BCG and the position of the SZ centroid D_{BCG-SZ} is greater than 0.4 R_{200}. This distance varies during the interaction, making it possible for a disturbed cluster to have this offset momentarily close to zero. The last criterion was chosen given that the distribution of D_{BCG-SZ} looks flat after this value. Clusters that don't meet any of the four previously mentioned criteria are considered in an intermediate evolutionary state and are excluded from this analysis. The BCG position is used as a proxy of the collisionless component since it is expected to quickly fall to the lowest region of the potential well (Tremaine, 1990). This position was derived from optical observations. Meanwhile, the centroid of the SZ was used as a proxy for the collisional component. When a cluster interacts with other clusters or groups, the gas, dark matter and galaxy components act differently depending on their nature. Then, the offset between the collisional and collisionless matter components can be used as a proxy to quantify the relaxation state of clusters (Zenteno et al., 2020).

In Figure 3.4.1, we present the stacked CMD for the four subgroups: low and high redshift relaxed clusters and low and high redshift disturbed clusters. The gray scale covers the same numeric range in the four panels. Darker (lighter) colours represents higher (lower) density regions in colour-magnitude space. In all panels we see a dominant RS with an associated

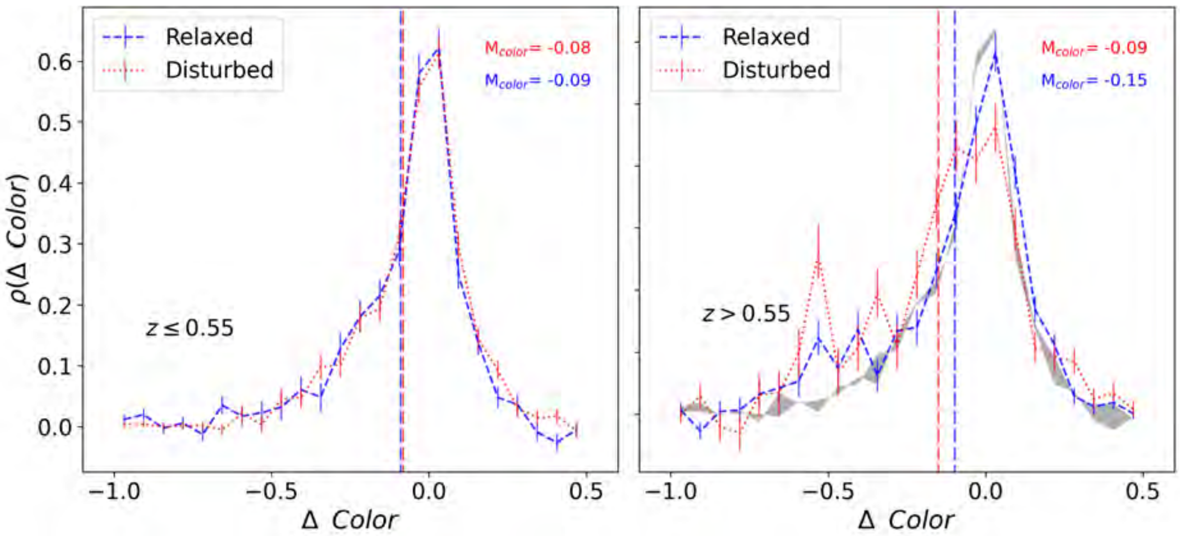

Figure 3.4.2: Colour density distributions for galaxies in each sample bin. The left panel presents the colour density distribution for the low-redshift bins relaxed in the blue line and disturbed in the red line and their error bars were computed as a Poisson noise. The vertical dashed lines indicate the median of the corresponding distribution. The right panel presents the same as described before, but for the high redshift $(z > 0.55)$ clusters, also in gray scale we show the density distribution for the low-redshift clusters.

bluer galaxy population. For the low redshift sample, we find that disturbed and relaxed clusters red sequence show similar colour distributions. This is, the relative contribution from early- and late-type galaxy populations to the CMD is comparable in both cases, indicating that the current dynamical state of a galaxy cluster has little impact on its CMD at the present-day. On the other hand, on the bottom panels of Figure 3.4.1 we show the RS for the high redshift sample. These RS distributions are generally wider with respect to the low-redshift counterpart. More interestingly, we observe a wider colour distribution in the disturbed cluster population when compared with both the high redshift relaxed distribution and the overall low redshift sample.

Figure 3.4.2 shows histograms from collapsing Figure 3.4.1 in the magnitude $(m - m^*)$ axis for the four studied subgroups. Those histograms are normalised by their Euclidean norm. In the left panel, we have the relaxed and disturbed clusters for low redshift clusters $(z < 0.55)$. Similarly, in the right panel we have the galaxy colour distribution for high redshift clusters $(z > 0.55)$, relaxed in blue, and disturbed in red. The error bars were computed as Poisson noise. In this plot, we also present in vertical dashed lines the medians of the colour distribution, we can see that for the low-redshift sample, the colour density distribution is very similar for the relaxed and disturbed clusters, and the medians are also nearly identical. However, in the right panel, we can see an excess of blue galaxies in the disturbed sample compared to the relaxed clusters. The differences shown in the bottom panel are above the observational uncertainties, and the values of the medians are significantly different, -0.09 for relaxed clusters and -0.15 for disturbed clusters. This result shows that the galaxy population of disturbed clusters is bluer and possibly less quenched compared to the relaxed clusters.

3.5 Bands Mixture Analysis

In this section, we analyze the effect of mixing photometric bands during the construction of the cluster RS. As showed in Table 3.5.1, we join in the low redshift bin clusters observed with $g - r$ $(z \leq 0.33)$ filters and $r - i$ $(0.33 < z \leq 0.55)$ filters and for the high redshift bin, we join $r - i$ $(0.55 < z \leq 0.74)$ and $i - z$ $(0.74 < z \leq 0.9)$ observations. Those bands capture the 4000 Å Balmer break that allows us to detect a prominent cluster Red Sequence. The RS position in the CMD was corrected using the Bruzual & Charlot (2003) stellar evolution model before stacking to avoid introducing a redshift bias in our sample. However, in this section we repeated the analysis using just the clusters observed between $0.33 < z \leq 0.74$ using $r - i$ bands to confirm that the differences observed between relaxed and disturbed clusters for high redshift bin is not a consequence of

Table 3.5.1: Number of cluster in low and redshift bins considering the clusters observed using just the r and i bands.

Redshift range	Relaxed clusters	Disturbed clusters
$0.33 < z < 0.55$	12	22
$0.55 \leq z < 0.74$	19	15

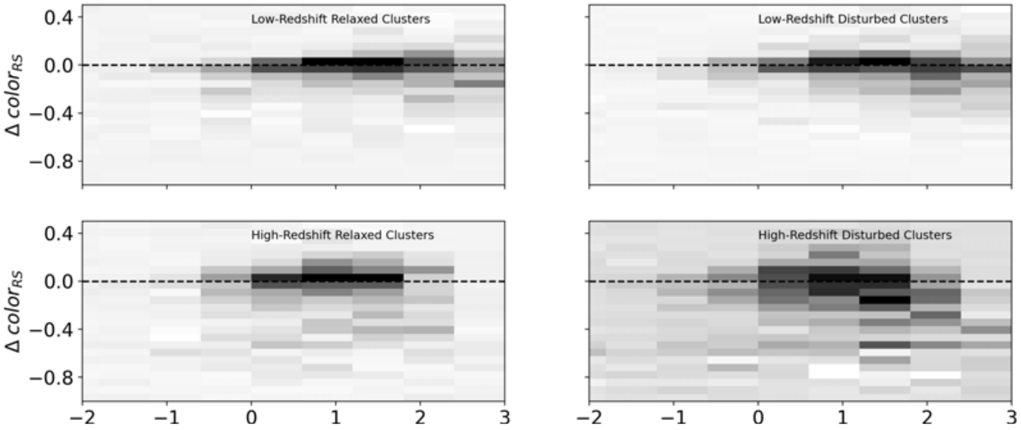

Figure 3.5.1: Similar to Fig. 3.4.1 but using only the r-i vs i colour magnitude diagram. In the top row we have the low$-z$ $(0.33 < z < 0.55)$ relaxed (left) and disturbed clusters (right), and in the bottom row we have the relaxed (left) and disturbed (right) clusters for the high$-z$ bin $(0.55 < z < 0.74)$. It can be seen that combining multiple colours do not affect our results.

mixing photometric bands. In Table 3.5.1, we have the number of stacked clusters for each considered subgroups, we can see that in each subgroup we have at least 12 clusters for low redshift bins and 22 clusters for high redshift bins. Similar to the previous analysis, we stacked the CMD in each subgroup after the redshift correction using the Bruzual & Charlot (2003) stellar evolution model. The morphology of the RS is the same that the showed in the Fig. 3.4.1 and the conclusions are the same: at low redshift bins, the galaxy population is mainly dominated by early-type galaxies, however at high redshift bins, there is a remnant blue (no yet-quenched) galaxy population.

We also repeated a colour density diagram presented in the Fig. 3.4.2 for cluster observed with $r - i$ bands presenting in the Fig. 3.5.2. We can see that those diagrams are very similar and the differences in colour are maintained between relaxed and disturbed clusters at high redshift bins. We also can conclude that the galaxy population at high redshift bins is more mixed in disturbed clusters compared to relaxed ones. With those two plots, we show that the morphological differences in RS come from the intrinsic properties of clusters and not from the band mixing process.

3.6 Discussion and Conclusions

We used optical data for 84 galaxy clusters detected by SPT-SZ and optically confirmed by the DES survey. The data set is composed by 65 galaxy clusters from DES survey DR2 and 19 high-z clusters from our dedicated observations. Both data sets were observed using the Blanco telescope and the Dark Energy Camera. In order to have an homogeneous data set, we performed a calibration using the Stellar Locus Regression code. This allowed us to correct systematic differences between both data sets. We divided the final sample in two redshift bins at $z = 0.55$.

The results summarized in Fig. 3.4.2, show that, as expected, high redshift clusters have a more significant blue galaxy population with respect to the low redshift subsample (see e.g. Butcher & Oemler, 1984). At $z \lesssim 0.55$ the relaxed and disturbed show almost identical CMDs. However, at $z \gtrsim 0.55$ we see significant differences in their cluster galaxy colour distribution. Specifically, the disturbed sample shows an excess of blue galaxies with respect to the relaxed sample.

This result provides more evidence that the galaxy colour distribution not only depends strongly on the global environment (e.g. Peng et al., 2010; Iovino et al., 2010; Muzzin et al., 2012), but also depends on the dynamical state of the clusters (e.g.,

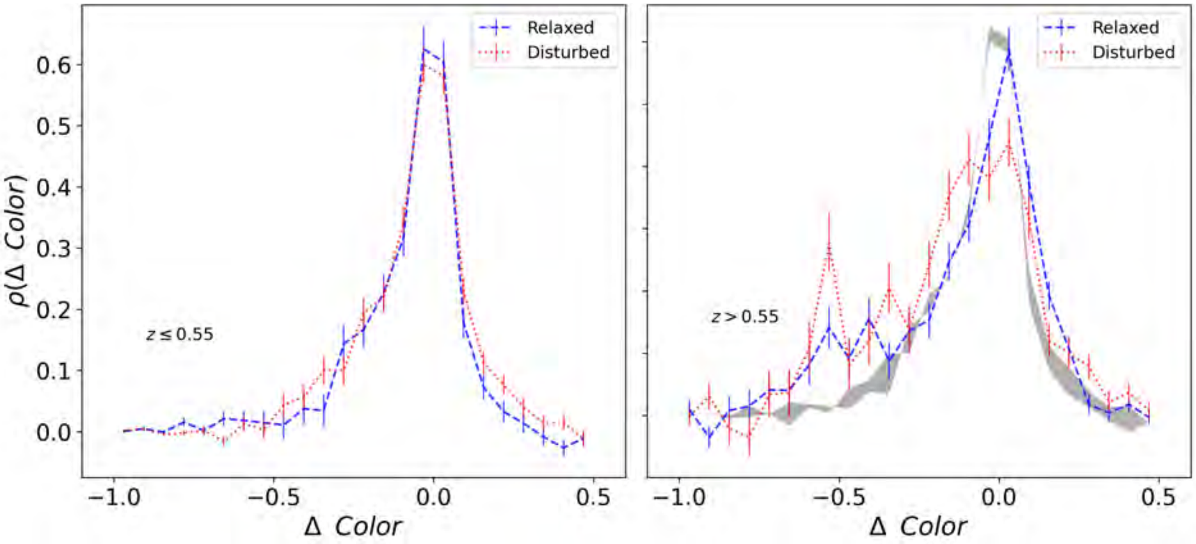

Figure 3.5.2: Similar to Fig. 3.4.2 but using only the r-i versus i colour magnitude diagram. The left panel presents the colour density distribution for the low-redshift bins relaxed in blue line and disturbed in red. Right panel the same for $(z > 0.55)$. It can be seen that combining multiple colours does not affect our results.

Stroe et al., 2017; Zenteno et al., 2020; Stroe & Sobral, 2021), at least at $z \gtrsim 0.55$. Our results are consistent with the anti-correlation between the relaxed state of the cluster and their star formation activity found by Cohen et al. (2015) and Hou et al. (2012). The two possible explanations for the excess in the blue population are the same than the ones proposed by Cohen et al. (2015) for the enhancement of the SFR: *i)* the merging process triggers star formation in the galaxies inside the merging clusters generating a more mixed and bluer galaxy population or *ii)* disturbed clusters correspond to a less evolved state than relaxed clusters. Its worth noting that our results are consistent with Pallero et al. (2022). Using a suite of fully cosmological hydrodynamical simulations, they showed that most quenched galaxies in massive halos $(M_{200} > 10^{14} M_{\odot})$ at $z < 0.5$ were quenched in ex-situ groups or clusters. However for $z > 0.5$ the in-situ quenched galaxies dominates their population, suggesting that the galaxies quenched inside the first cluster they fall in. In this scenario, at $z > 0.5$ relaxed clusters would have a redder population than disturbed clusters, as they have had more time to evolve their population in-situ. At $z < 0.5$ that difference disappears; the disturbed sample and relaxed clusters have the same galaxy population since they are being assembled from structures whose members have been already preprocessed within massive substructures. Indeed, this scenario could explain why the galaxy colour distribution at low redshift is the same in both, relaxed and disturbed sample. It is worth to mention that our results do not change if SLR correction is not applied to the data in §3.3.

Based on the results obtained in this Chapter, it is not possible to conclude what is the physical mechanism driving the excess of blue galaxies in disturbed high-z clusters. In Chapter 4, we compare our results against cosmological simulations to characterise the mechanisms responsible for such differences.

3.7 List of clusters

In Table 3.7.1, we present the list of the 19 high-redshift clusters observed in the frame of the DeROSITAS survey. Alongside their names, we also present the redshift, virial mass (SZ-based), and virial radius obtained using spectroscopic and photometric observations as specified in (Zenteno et al., 2020). In Table 3.7.2, we present the list of the clusters observed by DES including their redshifts, masses, and radius. Finally, in Table 3.7.4, we present the exposure time, FWHM and the number of observations made for one of those 19 high-z galaxy clusters in bands (r, i, and, z). .

Name SPT-CL	SPT RA J2000	SPT Dec. J2000	z	M_{200} $10^{14}h_{70}^{-1}\ M_{\odot}$	R_{200}
J0014-4952	3.69	-49.87	0.752	3.27	8.10
J0058-6145	14.58	-61.76	0.83	2.87	6.65
J0131-5604	22.93	-56.08	0.69	3.17	6.17
J0230-6028	37.64	-60.46	0.68	3.06	5.41
J0310-4647	47.62	-46.78	0.709	3.17	6.53
J0313-5645	48.26	-56.75	0.66	2.82	3.96
J0324-6236	51.05	-62.60	0.75	3.21	7.57
J0406-4805	61.72	-48.08	0.737	3.16	7.01
J0406-5455	61.69	-54.92	0.74	2.86	5.23
J0422-4608	65.74	-46.14	0.7	2.79	4.36
J0441-4855	70.45	-48.91	0.79	3.05	7.23
J0528-5300	82.02	-53.00	0.768	2.84	5.53
J0533-5005	83.40	-50.09	0.881	2.64	5.78
J2043-5035	310.82	-50.59	0.723	3.18	6.88
J2222-4834	335.71	-48.57	0.652	3.62	8.22
J2228-5828	337.21	-58.46	0.71	2.85	4.77
J2242-4435	340.51	-44.58	0.73	2.66	4.10
J2259-6057	344.75	-60.95	0.75	3.34	8.57
J2352-4657	358.06	-46.95	0.73	3.14	6.71

Table 3.7.1: 19 *high-z clusters* used in this analysis. The redshift, virial mass and virial radius were obtained from Zenteno et al. (2020)

.

Name SPT-CL	SPT RA J2000	SPT Dec. J2000	z	M_{200} $10^{14}h_{70}^{-1}\ M_{\odot}$	R_{200}
J0000-5748	0.24	-57.80	0.702	3.25	6.91
J0033-6326	8.47	-63.44	0.597	3.67	7.12
J0038-5244	9.72	-52.74	0.42	4.16	4.79
J0107-4855	16.88	-48.91	0.6	3.08	4.24
J0111-5518	17.84	-55.31	0.56	3.23	4.23
J0123-4821	20.79	-48.35	0.655	3.38	6.73
J0135-5904	23.97	-59.08	0.49	3.57	4.28
J0144-4807	26.17	-48.12	0.31	5.27	4.8
J0145-5301	26.26	-53.02	0.117	14.25	7.73
J0147-5622	26.96	-56.37	0.64	3.01	4.54
J0151-5654	27.78	-56.91	0.29	5.54	4.75
J0152-5303	28.23	-53.05	0.55	3.79	6.59
J0200-4852	30.14	-48.87	0.498	4.18	7.13
J0212-4657	33.10	-46.95	0.655	3.71	8.93
J0217-4310	34.41	-43.18	0.52	3.89	6.3
J0231-5403	37.77	-54.05	0.59	3.26	4.87
J0232-5257	38.18	-52.95	0.556	4.03	8.08
J0243-5930	40.86	-59.51	0.635	3.48	6.92
J0253-6046	43.46	-60.77	0.45	3.9	4.6
J0256-5617	44.09	-56.29	0.58	3.7	6.83
J0257-4817	44.44	-48.29	0.46	3.93	4.95
J0257-5732	44.35	-57.54	0.434	4.04	4.73
J0257-5842	44.39	-58.71	0.44	4.09	5.05
J0304-4748	46.15	-47.81	0.51	3.93	6.2
J0307-5042	46.95	-50.70	0.55	4.03	7.92
J0307-6225	46.83	-62.43	0.579	3.84	7.63
J0317-5935	49.32	-59.58	0.469	4.12	5.96
J0334-4659	53.54	-46.99	0.485	4.48	8.29
J0337-4928	54.45	-49.47	0.53	3.59	5.14
J0337-6300	54.46	-63.01	0.48	3.77	4.81

Table 3.7.2: 65 DES clusters used in this analysis. The redshift, virial mass and virial radius were obtained from Zenteno et al. (2020)

.

Name SPT-CL	SPT RA J2000	SPT Dec. J2000	z	M_{200} $10^{14} h_{70}^{-1}\ M_{\odot}$	R_{200}
J0342-5354	55.52	-53.91	0.53	3.58	5.11
J0343-5518	55.76	-55.30	0.55	3.59	5.61
J0352-5647	58.23	-56.76	0.649	3.34	6.41
J0354-5904	58.56	-59.07	0.41	4.61	6.19
J0403-5719	60.96	-57.32	0.466	4.05	5.58
J0429-5233	67.43	-52.56	0.53	3.32	4.08
J0439-4600	69.80	-46.01	0.34	5.77	7.86
J0439-5330	69.92	-53.50	0.43	4.23	5.32
J0451-4952	72.96	-49.87	0.39	4.34	4.6
J0509-5342	77.33	-53.70	0.461	4.52	7.57
J0522-5026	80.51	-50.43	0.52	3.51	4.62
J0526-5018	81.50	-50.31	0.58	3.15	4.25
J0542-4100	85.71	-41.00	0.642	3.6	7.82
J0550-5019	87.55	-50.32	0.65	2.9	4.17
J0551-5709	87.90	-57.15	0.423	4.79	7.42
J0559-5249	89.925	-52.82	0.609	3.88	8.76
J0600-4353	90.06	-43.88	0.36	5.4	7.35
J0611-4724	92.92	-47.41	0.49	3.9	5.56
J0612-4317	93.02	-43.29	0.54	3.73	6.02
J2011-5725	302.85	-57.42	0.279	5.88	5.16
J2022-6323	305.52	-63.39	0.383	4.85	6.17
J2040-5342	310.21	-53.71	0.55	3.66	5.94
J2055-5456	313.99	-54.93	0.139	11.8	6.99
J2130-6458	322.72	-64.97	0.316	5.96	7.25
J2134-4238	323.50	-42.64	0.196	9.45	8.85
J2140-5331	325.03	-53.51	0.56	3.31	4.56
J2146-5736	326.69	-57.61	0.602	3.36	5.57
J2148-6116	327.18	-61.27	0.571	3.71	6.7
J2232-5959	338.14	-59.99	0.594	3.89	8.39
J2233-5339	338.32	-53.65	0.44	4.81	8.23
J2254-5805	343.58	-58.08	0.153	9.75	5.08
J2331-5051	352.96	-50.86	0.576	3.99	8.46
J2332-5358	353.10	-53.96	0.402	5.08	7.89
J2344-4224	356.14	-42.41	0.29	5.44	4.49
J2358-6129	359.70	-61.48	0.37	4.92	5.92

Table 3.7.3: 65 DES clusters used in this analysis. Continued.

Name	Exposure Times^a (s)			FWHM (”)			N_{obs}		
	r	i	z	r	i	z	r	i	z
J0014-4952	–	1840	2090	–	0.95	0.78	–	10	11
J0058-6145	–	3150	4746	–	1.06	1.16	–	15	21
J0131-5604	–	1200	1800	–	0.97	0.82	–	8	10
J0230-6028	–	1200	2938	–	0.94	1.15	–	8	13
J0310-4647	–	3750	1800	–	1.03	0.90	–	27	10
J0313-5645	–	1080	3080	–	1.10	1.17	–	9	14
J0324-6236	–	2000	2640	–	1.00	0.87	–	10	15
J0406-4805	–	1575	2460	–	0.96	0.94	–	8	12
J0406-5455	–	1600	3750	–	1.01	0.88	–	8	15
J0422-4608	–	2638	2152	–	0.91	1.03	–	18	13
J0441-4855	–	1400	4200	–	0.84	0.99	–	7	14
J0528-5300	–	3000	3300	–	1.11	1.03	–	15	11
J0533-5005	–	5700	4815	–	0.98	0.86	–	19	15
J2043-5035	2045	1664	1400	1.30	1.10	0.84	14	8	7
J2222-4834	1050	1080	–	1.39	0.81	–	9	9	–
J2228-5828	600	–	–	1.51	–	–	4	–	–
J2242-4435	2085	1335	2000	1.22	1.52	0.81	15	10	10
J2259-6057	–	3579	3600	–	1.13	1.01	–	18	18
J2352-4657	–	1582	5350	–	0.97	0.89	–	9	22

Table 3.7.4: Observations of the *high-z clusters* sample. ^{a}The exposure times shown are in addition to the observations carried out by DES (Abbott et al., 2021), which were included in the final *griz* stacks.

Chapter 4

Dependence of the physical properties of satellite galaxies with the cluster's dynamic state.

Abstract

Galaxy groups and clusters are the most massive collapsed structures in the Universe. Those structures are formed by merging with other smaller structures. Groups and cluster mergers provide an appropriate environment for the evolution and transformation of their galaxies. The merging process of groups and clusters can affect the properties of their galaxy populations. Our aim is to characterise the distribution of galaxies' colour, specific star formation rate, quenched galaxy fraction, and gas availability in galaxies bounded to groups and clusters and to examine how these properties relate to the dynamical state of their host environments. We used the most massive halos ($M > 10^{13}$ $M_\odot$) in Illustris TNG100 simulations and separated the sample into two categories: relaxed and disturbed halos. This classification was done based on the offset between the position of the Brightest Cluster Galaxy (BCG) and the centre of mass of the gas. Subsequently, we classified their galaxy populations into red and blue galaxies using a threshold derived from a double Gaussian fit to their colour distribution. Additionally, we distinguished between star-forming and quenched galaxies by applying a threshold defined as one dex below the interpolated star-formation main sequence. Our findings reveal differences in physical properties such as colour, star formation rates, and gas availability among satellite galaxies bound to interacting clusters compared to relaxed clusters. Disturbed clusters exhibit more blue, star-forming galaxies than their relaxed counterparts. This discrepancy in the fraction of blue and star-forming galaxies can be attributed to higher gas availability, including hot, diffuse, and condensed gas in satellite galaxies in disturbed clusters compared to relaxed ones. Furthermore, our study shows that during cluster mergers, there are two crucial phases; at the beginning of interaction, there is an important boost in the star formation rate followed by a suppression as the cluster reaches the equilibrium state. [1]

---

[1] Based on Aldás, Gómez & Vega-Martínez, submitted to A&A.

4.1 Introduction

Galaxy groups and clusters are the most massive gravitationally bounded structures in the Universe, containing up to thousands of luminous galaxies (Abell, 1958; Abell et al., 1989). According to the ΛCMD model, the building of structures in the Universe followed a hierarchical process. Initially, small overdensities in the primordial Universe collapsed, and later developed into larger systems, such as groups and clusters, through merging and accretion with other smaller structures (Cole et al., 2000; White & Rees, 1978; White & Frenk, 1991). As a result, galaxy groups and clusters are not always in a dynamic equilibrium. A significant fraction, between 30 and 70%, is currently undergoing a merger process (Hou et al., 2012). Cluster mergers rank among the most energetic events in the Universe, second only to the Big Bang, releasing energies up the order of 10^{63} erg. (Sarazin, 2001; Molnar, 2016). During these collisions, the evolution of the two primary cluster components exhibits distinct behaviours: dark matter, characterised by its collisionless nature, is only driven by gravitational force. In contrast, gas is susceptible to pressure forces and dissipative effects (Molnar, 2016). Both, gravity and dissipation significantly influence the star formation history of cluster member galaxies during the cluster-merging process (Caldwell & Rose, 1997). Therefore, these powerful events provide suitable environmental conditions for galaxy transformation and evolution. Indeed, whereas galaxy groups and clusters are mainly populated by red and quenched galaxies (Oemler & Hale Observatories, 1974; Dressler, 1980), recent studies suggest the physical properties of satellite galaxies differ between relaxed and disturbed clusters. In this sense, in Chapter 3, using a sample of 84 galaxy clusters with redshifts between $z = 0.1 - 1$, we showed that relaxed clusters have a redder galaxy population. In comparison, disturbed clusters have a more diverse and bluer galaxy population. This finding is supported by the observations of Sobral et al. (2015) and Yoon & Im (2020), who found that interacting clusters exhibit an increased star formation rate compared to non-interacting ones. In contrast, other studies, such as those by (Kleiner et al., 2014) and (Shim et al., 2011), found no evidence of an increase in the star formation rate, suggesting that interacting clusters can even suppress star formation.

The dynamical state of groups and clusters can play an important role in their mass determinations, which are typically estimated using self-similarity scaling relations. The relations are highly dependent on the structure's dynamical state. An example is the scaling relation proposed by Munari et al. (2013), which relates the cluster galaxies' velocity dispersion and the cluster mass, $\sigma \propto \mathrm{M}_{200}^{\alpha}$, where M_{200} represents the virial mass and α is a fitting parameter. M_{200} is defined as the mass enclosed inside the virial radius (R_{200}), which is the radial distance where the cluster's density is 200 times the critical density of the Universe. Additional scaling relations usually assume equilibrium between the intra-cluster medium and the gravitational potential well, meaning that the cluster is entirely relaxed (Maughan, 2013). Examples are the power law proposed by Kravtsov et al. (2006) expressed as $\mathrm{M}_{500} = C\mathrm{Y}_{x}^{\alpha}$, which is a commonly used scaling relation between $\mathrm{Y}_x = T_X M_{gas}$, which is the product between the temperature and gas mass and mass, and the widely used Sunayev-Zeldovich (SZ) emission (Y_{SZ}) to mass scaling relation $M \propto \mathrm{Y}_{SZ}^{\alpha}$ proposed by Nagai (2006) and Battaglia et al. (2012). However, some studies show deviation of those scaling relations for non-relaxed galaxy clusters, leading to errors in the mass estimation (Barnes et al., 2021; Biffi et al., 2016).

From an observational standpoint, the dynamic state of clusters has been quantified using data from different wavelengths. Radio-emitting clusters are often associated with disturbed clusters due to shocks during merging that can trigger the acceleration of charged particles and lead to synchrotron radiation (Brunetti et al., 2008). In contrast, those lacking radio emission are considered relaxed clusters (Brunetti et al., 2007, 2009; Feretti et al., 2012). The presence of a cool core in X-ray observations of clusters has also been used as an indicator of a relaxed state in these clusters. When the radiative cooling time in the core is shorter than the cluster's age, it suggests that the cluster has likely attained a relaxed state (Bauer et al., 2005). This inference is grounded in the fact that X-rays emitted by the ICM induce a temperature drop in the innermost regions of galaxy clusters. In addition, some authors have investigated the dynamical state of galaxy clusters by examining morphological parameters of their X-ray emission, such as the asymmetry parameter (A_{phot}). This parameter quantifies the deviation of the photometric distribution within a specific annulus from a symmetric distribution (Nurgaliev et al., 2013, 2017). Another parameter commonly used is the centroid shift, which measures the offset between the position of the centroid of the X-ray surface brightness and the peak of the X-ray emission (Nurgaliev et al., 2017; Yuan et al., 2022; Campitiello et al., 2022). In this sense, Campitiello et al. (2022) defined a relaxation parameter (M) to produce a unique indicator of the dynamical state of the clusters as the combination of the centroid shift (separation between the X-ray peak and the centroid of the X-ray surface brightness), the concentration index, which measures the ratio of the surface brightness measured in two apertures (0.1 and 1 R_{500}), and the power ratio, which is based on the multipolar two-dimensional decomposition of the X-ray surface brightness.

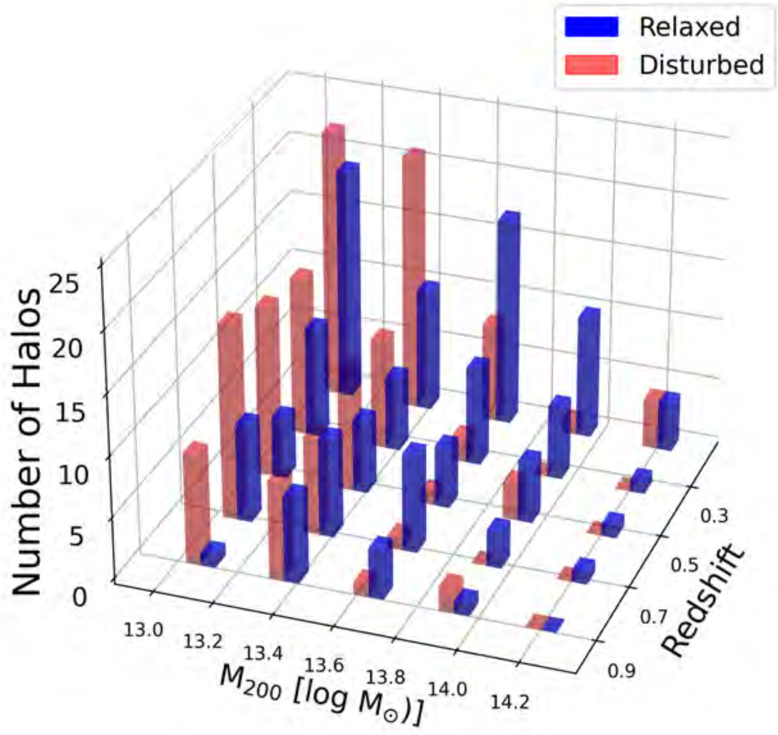

Figure 4.2.1: Histogram presenting the halos selected for this study in function of their virial mass (M_{200}) in the x-axis and their redshift (z) in the y-axis. In blue we have the selected relaxed clusters and in red the disturbed sample.

Cosmological simulations also have been used to investigate the dynamical state of galaxy clusters, computing other indicators. For example, Bett et al. (2007) used the 'virial ratio', defined as $2T/U + 1$, to select the halos near the equilibrium state, where T is the total kinetic energy and U is the total potential energy of the halo particles. Neto et al. (2007) proposed another two parameters: i) the offset between the position of the centre of mass of the halo and the potential centre, and ii) the substructure mass fraction defined as the ratio of the central galaxy to the total mass. Additionally, there are some other parameters to measure the relaxation state of the clusters using the combination of these three parameters (Haggar et al., 2020; De Luca et al., 2021). However, Zhang et al. (2022) showed that the most important parameter to classify the dynamical state of clusters is the offset between the position of the most bounded particle, or density cusp, and the cluster's centre of mass.

In this Chapter, we unveil the influence of the galaxy cluster's dynamical state on the physical properties of their galaxy population, such as colour, star formation, metallicity, and gas availability. We also investigate the physical mechanisms responsible for causing these changes. This work was done using a fully cosmological simulation Illustris-TNG that includes a model to describe galaxy formation and evolution. This Chapter is organised as follows: Section 4.2 provides an overview of the cosmological simulations used. Section 4.3 describes how we selected our sample and characterised the dynamical state of halos. Section 4.4 and 4.5 explain the differences in the physical properties of relaxed and disturbed clusters. Section 4.6 describes how these differences vary as a function of the redshift. Section 4.7 discusses the gas availability in galaxies bound to clusters in different relaxation states. Finally, Section 4.8 presents an example of the evolution of star formation and gas availability as a function of time.

4.2 Cosmological Simulations

In this project, we use the Illustris TNG cosmological magnetohydrodynamical simulations, which are a series of large simulations aimed at exploring the formation and evolution of galaxies within the Λ-Cold Dark Matter model framework (Pillepich

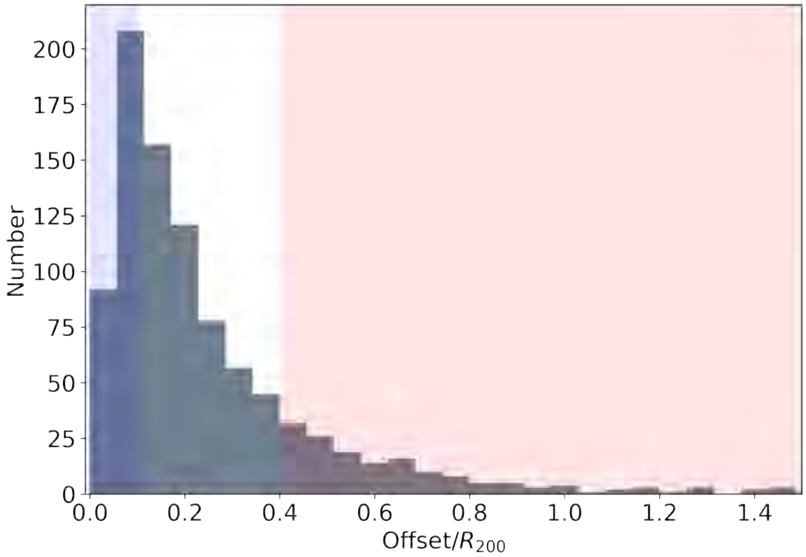

Figure 4.3.1: Histogram of the offset between the position of the Brightest Galaxy Cluster (BCG) and the center of mass of the gas used as an indicator of the dynamical state of groups and clusters. In the blue shadow area, the selected 153 most relaxed groups and clusters between $0.1 \leq z \leq 1$, and in the red shadow area, the selected 153 disturbed ones.

et al., 2018b; Springel et al., 2018; Naiman et al., 2018; Nelson et al., 2018; Marinacci et al., 2018). Illustris TNG was run with the AREPO code, a flexible code for hydrodynamical cosmological simulations that solves Poisson's equation in a fully dynamical unstructured mesh with a finite-volume method (Weinberger et al., 2020). These simulations include inhered models from Illustris simulations incorporating non-linear physical processes driving galaxy formation and evolution, such as star formation, stellar evolution, chemical enrichment, and gas recycling (Vogelsberger et al., 2014; Gene et al., 2014; Sijacki et al., 2015). Illustris TNG also has updated models for the growth and feedback of supermassive black holes, galactic winds, and metal abundance evolution (Weinberger et al., 2017; Pillepich et al., 2018a). This model exhibits a good agreement with observational data regarding the abundance of molecular and atomic gas in the IllustrisTNG, as compared to the abundances derived with the 21-cm Hydrogen line using the Giant Metre-wave Radio Telescope (Rhee et al., 2018; Diemer et al., 2019). This suite of simulations has three different box sizes: 50 Mpc, 100 Mpc, and 300 Mpc per side, hereafter TNG50, TNG100, and TNG300, respectively. Each box has different mass resolutions for Dark Matter (DM) and baryonic particles. The groups and clusters in the Illustris-TNG simulations were identified using the Friend-of-Friends algorithm with a linking length of $b = 0.2$ (Springel et al., 2018). Their corresponding subhalos were identified using the SUBFIND algorithm (Springel et al., 2001; Dolag et al., 2009). The TNG300 simulation has a volume 27 times larger and contains approximately 20 times more halos than TNG100 (Pillepich et al., 2018b). However, TNG100 offers a mass resolution that is one order of magnitude better than TNG300. Specifically, TNG100 contains 1820^3 DM and an equivalent number of baryonic particles with a mass resolution of 7.5×10^6 M$_\odot$ and 1.4×10^6 M$_\odot$, respectively. For this work, we have chosen to use the TNG100 to balance the number of detected structures and a good resolution. TNG100 has more than 2000 halos with masses greater than 10^{12} M$_\odot$, and the most massive object detected at redshift $z = 0$ has a mass of 3.8×10^{14} M$_\odot$.

The Illustris TNG simulations reproduce notably well several observed statistical properties of the galaxy population. These properties include the clustering of galaxies as a function of stellar mass, colour, star formation, and redshift (Springel et al., 2018), the galaxy colour bimodality (Nelson et al., 2019), and the stellar mass functions from $z = 4$ to today (Pillepich et al., 2018b). Illustris TNG uses the cosmological parameters from Planck observations (Planck Collaboration, 2016), as follows: $\Omega_b = 0.0486$, $\Omega_m = 0.3089$, $\Omega_\Lambda = 0.6911$, and $H_0 = 67.74$ km s^{-1} Mpc^{-1}.

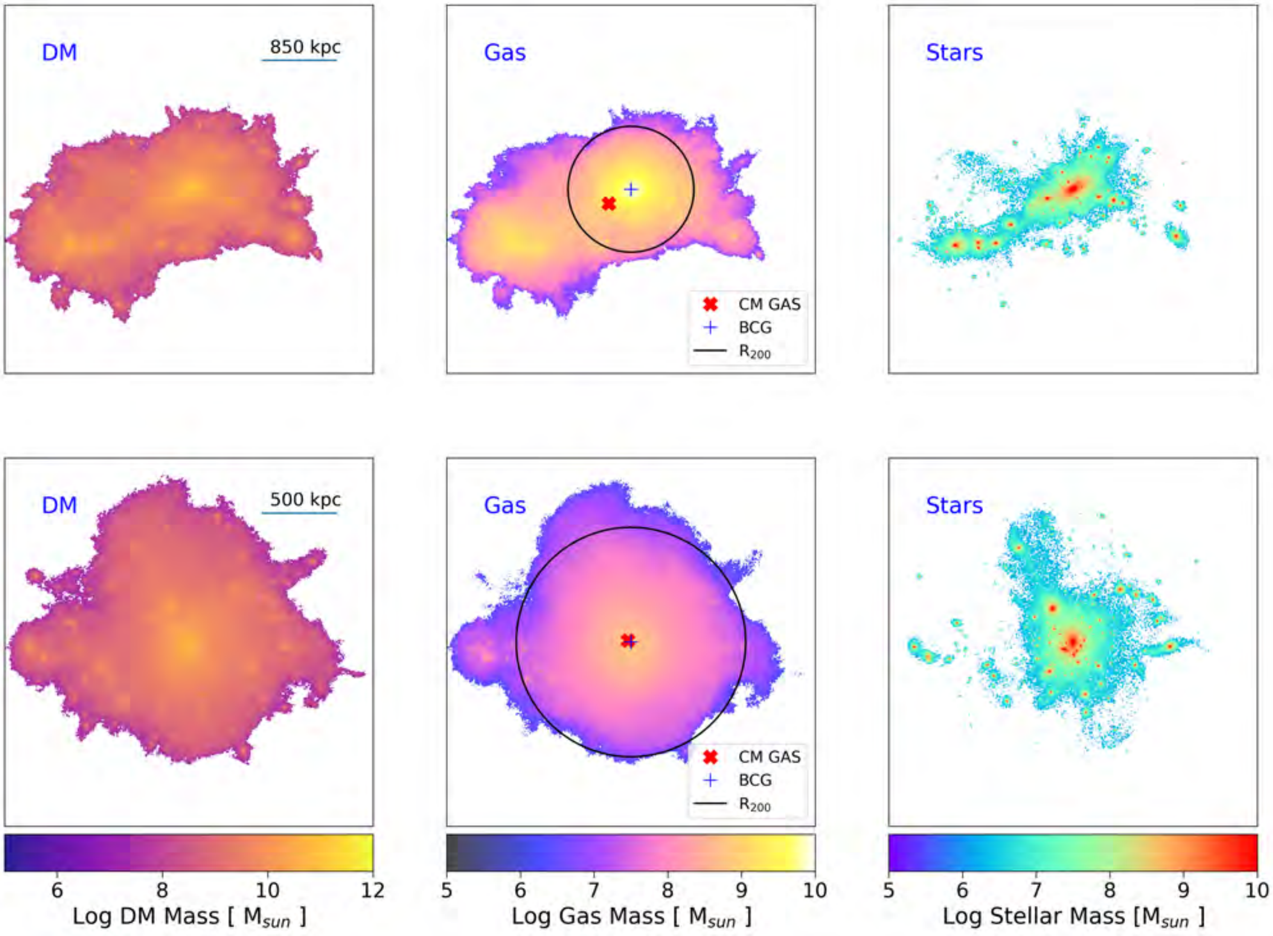

Figure 4.3.2: In the top panels, the dark matter (left), gas (centre), and stars particles (right) mass distribution, using the particles bounded to the FOF, for the most massive disturbed halo at redshift $z = 0.1$ of the Illustris TNG simulations. We also show the position of the BCG and the centre of mass of gas cells in the central panel; we can see that the position of the center of mass is located around 0.4R$_{200}$ measured from the position of the BCG. In the bottom panels, similar to the top panels, the distribution of the different components for the most massive relaxed halo at the same redshift.

4.3 Sample Selection

In this Chapter, we analyse the properties of galaxy populations in groups and clusters. Our focus will be on structures with masses greater than $M_{200} \geq 10^{13}$ M$_\odot$ containing at least ten galaxies per halo. This Chapter will consider as galaxies, subhalos with stellar mass greater than 10^9 M$\odot$, resolving each galaxy with more than 800 stellar particles. We look for clusters and groups of galaxies independently in different simulation snapshots, assuming that the dynamical state of the structures changes over time. We select halos from seven different redshifts, between 0.1 and 1. The used redshifts are 0.1, 0.2, 0.3, 0.4, 0.5, 0.7, and 1. Following Zenteno et al. (2020) and Chapter 3, to study the differences in properties of cluster galaxies at low and high redshifts, we subdivide our sample of galaxies into two redshift bins. The first is a low redshift bin from $0.1 \leq z < 0.5$ and a high redshift bin with halos between $0.5 \leq z \leq 1$.

In Figure 4.2.1, we present the selected groups and clusters' mass and redshift distribution. The virial mass is presented on the x-axis, and the redshift is on the y-axis. The masses between relaxed and disturbed clusters are similar; then the differences found in the next sections are not the result of the mass difference between relaxed and disturbed clusters. The mean temporal separation between the used snapshots is 1.3 Gyrs. This separation is around half the free-falling time for two collapsing

Table 4.3.1: Number of clusters in the selected sample in each analysed subgroup. We divided the sample into low and high redshift bins and relaxed and disturbed clusters. In parenthesis, we also show the number of bounded galaxies.

z	# Rel. clust. (Gal.)	# Dist. clust. (Gal.)
$0.1 < z < 0.5$	90 (2809)	80 (2682)
$0.5 \leq z < 1$	63 (1633)	73 (1802)
Total	153 (4442)	153 (4494)

structures with masses of 10^{14} $M_\odot$, which were initially separated at a distance of 1 Mpc. This ensures that the dynamical state of clusters will be different from one selected snapshot to another.

4.3.1 Dynamical State of Clusters

To study the dynamical state of galaxy clusters, following Zenteno et al. (2020), we separated our sample of groups and clusters of galaxies into relaxed and disturbed categories using an observationally motivated parameter: the 3D offset between the position of the BCG and the position of the center of mass of the gas. The position of the BCG is determined by the position of the most bound particle, and the center of mass of the gas is computed using all gas cells bound to the halo. We consider that a cluster is disturbed if the offset between the BCG and the center of mass of the gas ($D_{\text{BCG-CM}}$) is larger than $0.4 \times R_{200}$. We use the position of the center of mass of the gas as a proxy for the SZ effect centroid. Our proposed methodology aligns closely with the approach outlined by De Luca et al. (2021). In their study, they incorporate various indicators for the dynamical state, including the 3D offset between the centre of mass of the cluster considering all particle types and the position of the highest density peak. When considering the centre of mass computed across all particle types in our groups and clusters and imposing the same threshold of $0.4 \times R_{200}$, we find that comparing both methodologies, most of the groups and clusters classified as disturbed with our criteria (around 85%) are also classified as disturbed using the De Luca's criteria.

We found 640 groups and clusters with virial masses greater than 10^{13} $M_\odot$ within the selected seven snapshots. From those clusters, we identified 153 as disturbed structures. To make a fair comparison of the cluster galaxies' physical properties between relaxed and disturbed clusters, we also selected the 153 most relaxed clusters. These are the ones with the lowest $D_{\text{BCG-CM}}$ (< 0.01 R_{200}). Our criterion for identifying relaxed clusters is more stringent compared to the approach suggested by Cui et al. (2017) for the center of mass offset, leading us to focus solely on the most relaxed clusters. In Figure 4.3.1, we present a histogram of the distribution of D_{BCG-CM} in units of R_{200}. The blue and red shadowed areas show the selected relaxed and disturbed clusters, respectively. This selection criteria allow us to maximise the differences between the two samples. As a result, clusters that are in an intermediate relaxation state, which are located in between the shaded areas of Figure 4.3.1, have not been considered in this study. As shown in Table 4.3.1, the relaxed clusters have 4442 galaxies, while the disturbed ones have slightly larger substructures, corresponding to 4494 galaxies. Each subsample, i.e. disturbed and relaxed, is further subdivided into a low ($z < 0.5$) and high ($0.5 \leq z \leq 1$) redshift subsample. As a result, we end up with four distinct galaxy groups. The final number of galaxy clusters and the number of their member galaxies in each subgroup is given in Table 4.3.1. Each subgroup has at least 63 clusters and groups with at least 1633 bounded galaxies.

The left, middle and right columns of Figure 4.3.2 show the DM, gas and stellar mass distribution, of an example of disturbed (top panels) and relaxed (bottom panel) cluster, respectively. In the central panels, the blue '+' mark represents the position of the most bound particle, which traces the location of BCG. The red 'x' mark represents the position of the CM of the gas distribution, and the black circle represents the virial radius (R_{200}) of the halo centred in the BCG position. The disturbed cluster (top panels) has a halo with $M_{200} = 2.7 \times 10^{14}$ $M_\odot$ at redshift $z = 0.1$. We can see that the position of the CM of the gas has an offset of 0.42 R_{200} from the position of the BCG due to another massive structure that is infalling in the central halo. On the other hand, in the bottom panels, we present a halo with a mass of $M_{200} = 3.28 \times 10^{14}$ $M_\odot$, also at redshift $z = 0.1$, as an example of one relaxed cluster. We can see that, despite some small structures falling into the central halo, the position of the centre of gas remains the same as the position of the BCG, and the cluster's shape is much more symmetrical compared to the example of the disturbed one. In each example, the distribution of gas and DM mass follows similar shapes, in accordance with results by Rasia et al. (2004), who showed that the gas and DM follow similar density profiles with different concentration values for $r > 0.1R_{200}$. Finally, we can observe that the stellar mass is mainly distributed in the inner parts of

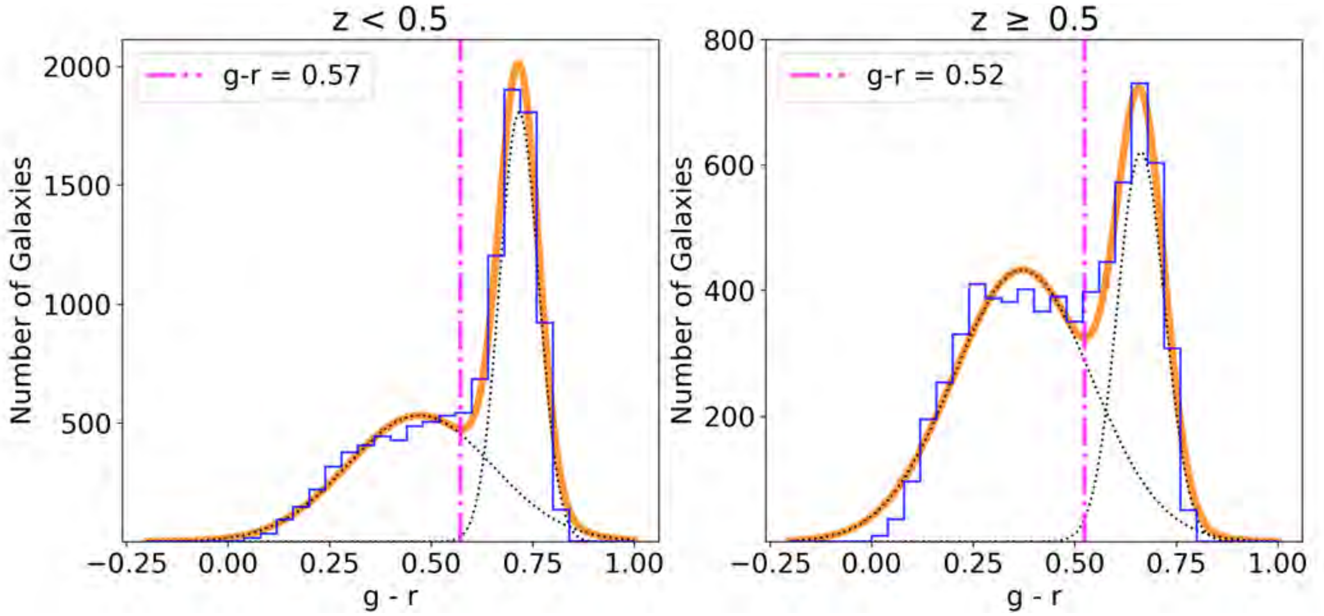

Figure 4.4.1: Galaxy color distribution in color $g-r$ (SDSS passbands in rest frame). In the left panel, we present the histogram for colours corresponding to galaxies at low redshift $(z < 0.5)$ and in the right panel, the histogram of colour distribution for galaxies belonging to clusters at high redshift $(0.5 \geq z < 1)$. In both panels, the orange line corresponds to a double Gaussian fit, and the pink dotted line corresponds to the threshold to separate between red and blue galaxies, defined as the minimum of the colour distribution. These thresholds are located at 0.57, and 0.52 for the low and high redshift subsamples, respectively.

the halo, where the gas density is large enough to trigger the star formation.

4.4 Galaxy Populations

In this section, we analyse the colour of galaxies, establishing a threshold to divide between red and blue galaxy populations. Additionally, we classify galaxies based on their star formation activity into star-forming and quenched galaxies. We consider all galaxies bound to groups and clusters, regardless of their dynamical state. The impact of the dynamical state on the physical properties of satellite galaxies will be studied in Section 4.5.

4.4.1 Color distributions

Galaxies are classified into red and blue based on their colours, providing insight into their dominant stellar populations. Red galaxies are characterised by a prevalence of late-type stars, while blue galaxies are dominated by early-type stellar populations. The Balmer break offers a way to identify sample sets of star-forming galaxies because its presence is common in A-type stars. The presence of A-type stars and their limited lifetime indicate recent star formation (Mihalas, 1967b; Poggianti & Barbaro, 1997). The Balmer break can be found by spectrography and photometry using specifically chosen colour indices. For this reason, we define the colour of a galaxy as the difference in magnitude between the simulated $g-$ and $r-$ SDSS broadband filters. TNG100 simulations provide the rest-frame absolute magnitudes for each galaxy computed as the summed-up luminosity of all-star particles gravitationally bounded to the subhalo in different passbands (Pillepich et al., 2018b).

The division into red and blue galaxies is typically done by using a threshold in the colour of the galaxies. As the threshold is expected to vary with redshift due to the Butcher-Oemler effect (Butcher & Oemler, 1984), we define a value for low-redshift and another for high-redshift galaxies. To determine these values, we followed the pipeline proposed by Guglielmo et al. (2019). This process consists of fitting a double-Gaussian model to the galaxy's colour distribution and using the local minimum of its distribution as the threshold. In the left panel of Figure 4.4.1, we show the double-Gaussian fit for galaxies in low-redshift clusters ($z < 0.5$), while the right panel shows the results for the high-redshift clusters ($z \geq 0.5$). Figure 4.4.1 shows that the colour distribution for galaxies is bimodal, with two well-defined peaks corresponding to the blue and red galaxy populations (Nelson et al., 2018). The peaks in the distribution of the blue and red galaxy populations are centred at 0.46 and 0.72 in (g-r) for the low-redshift bin, and are located at 0.37 and 0.66 for the high redshift bin. The thresholds, determined by the minimum between the two peaks, are g-r = 0.57 for low-redshift galaxies and g-r = 0.52 for high-redshift galaxies. We define a galaxy as red if its colour exceeds the threshold, while a galaxy is classified as blue if its colour falls below the threshold. These values obtained for the thresholds align with the findings of Guglielmo et al. (2019), which suggest that this value gets lower as the redshift increases.

Figure 4.4.1 illustrates that in the low redshift bin, the majority of the galaxy population is made up of red galaxies, while blue galaxies are more significant in the high redshift bin. This difference can be quantified by comparing the heights of the Gaussian curves. For low-redshift galaxies, the peak of the red population is approximately 3.5 times higher than that of the blue population. However, in the high redshift bin, the peak of the red population is only 1.5 times higher than that of the blue population. This procedure allowed us to naturally define two populations, effectively distinguishing between blue and red galaxies.

4.4.2 Star Forming and Quenched Galaxies

Galaxies can be classified based on their star formation activity into two categories: star-forming and quenched galaxies. Star-forming galaxies are characterised by ongoing star-formation activity, while quenched galaxies have consumed, depleted or heated their gas reservoir, resulting in the cessation of star formation. Defining a single threshold to classify star-forming and quenched galaxies is challenging since star-formation activity depends on the galaxy's mass and redshift. This work follows the definition of quenched galaxies proposed by Donnari et al. (2019) and Pillepich et al. (2019), which states that a galaxy is considered quenched if its Star Formation Rate (SFR) is one dex below the extrapolated star-forming main sequence (MS). Donnari et al. (2021) fitted the location of the MS in the stellar mass versus SFR diagram for the galaxies in the Illustris-TNG300 simulations using the relation:

$$\log\left(\frac{\langle \mathrm{SFR}\rangle_{\text{sf-ing galaxies}}}{\mathrm{M}_{\odot} yr^{-1}}\right) = \alpha(z)\log\left(\frac{\mathrm{M}_{\text{stars}}}{\mathrm{M}_{\odot}}\right) + \beta(z) \tag{4.4.1}$$

where $\alpha(z)$, and $\beta(z)$ are coefficients obtained from a iterative fitting process. The values for the coefficients are presented in Table 3 of Donnari et al. (2021). Despite the definition adopted in this work, the main results and conclusions do not change if we repeat the analysis using the widely used definition of quenched galaxies according to their specific star formation rate (sSFR), where a galaxy is quenched if $\log(\mathrm{sSFR}) < -11$ (Wetzel et al., 2012).

In this article, we have calculated the SFR of a galaxy by adding up the SFR of each gravitationally bounded gas cell in it. This value corresponds to the instantaneous star formation rate available in the IllustrisTNG catalogues (Donnari et al., 2019). However, observationally, deriving the SFR is a complex and costly effort that can consist of a variety of different methods (SED fitting, UV, IR, radio continuum), resulting in an average SFR value. Although both indicators give information about the galaxy's star-forming activity, the instantaneous SFR indicates the present stellar formation, while the galaxy's colour indicates its recent evolution.

4.5 Differences between Relaxed and disturbed clusters

In this section, we use the relaxed and disturbed clusters selected in a redshift range of $0.1 \leq z \leq 1$ to study the dependence of the physical properties of galaxies on the dynamical state of their host clusters. Figure 4.5.1 shows histograms of the galaxies colour, sSFR and stellar metallicity (Fe/H) in the first, second and last rows, respectively. The left panels present the galaxies within R_{200}, while the right panels present those outside R_{200}. In each panel, the histogram for galaxies inhabiting disturbed clusters is shown in red, while for galaxies inhabiting relaxed clusters in blue. All histograms are normalised by the corresponding total number of galaxies, i.e. inside and outside R_{200}. First, we notice a larger fraction of galaxies outside the virial radius (up to 3 R_{200}) in the disturbed clusters compared to the relaxed ones. This is expected since disturbed clusters are interacting with other structures that also have their satellite galaxies, often located outside the main structure's

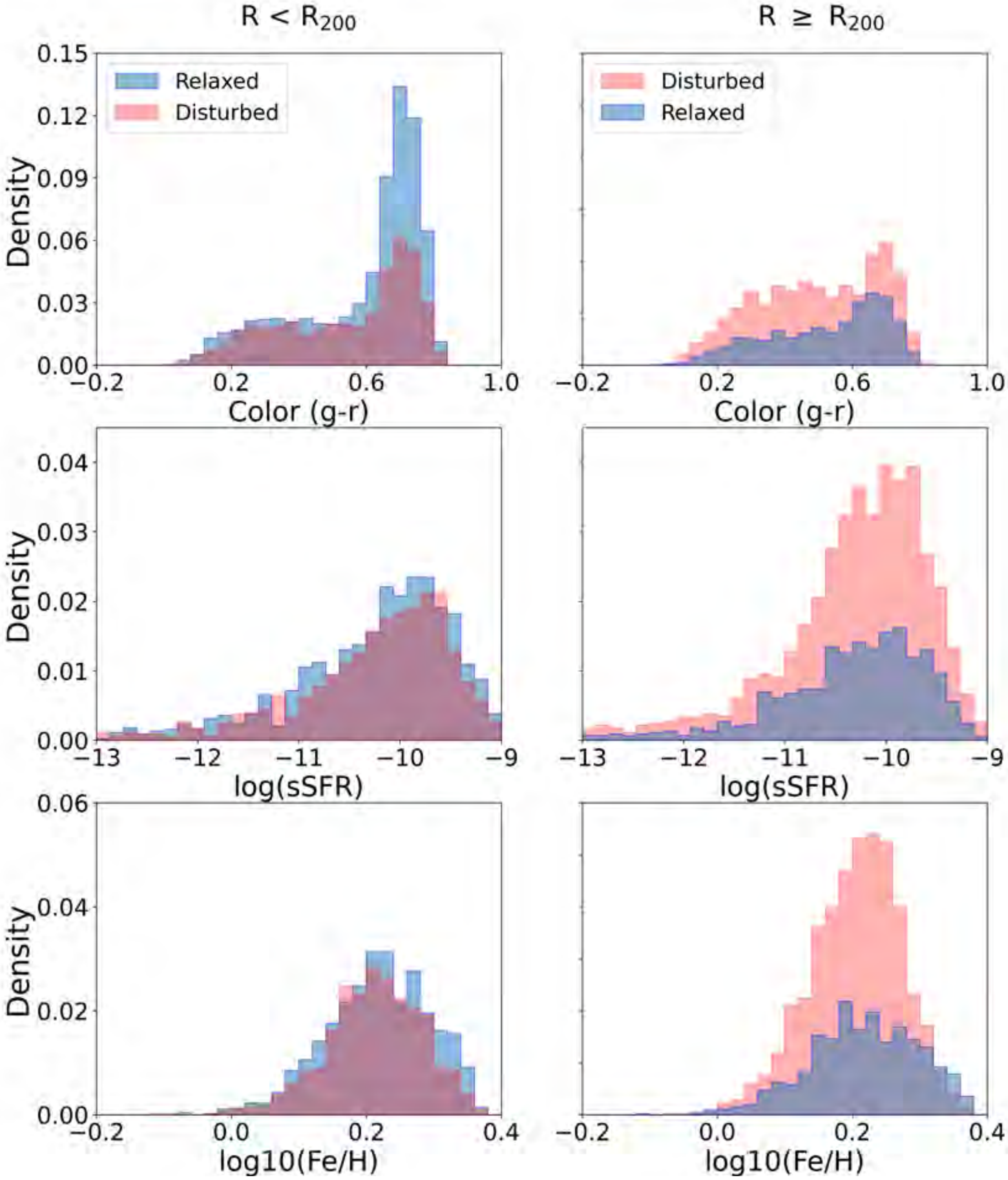

Figure 4.5.1: Differences in the physical properties (colour, sSFR and metallicity) of the satellite galaxies belonging to relaxed (blue) and disturbed (red) clusters. We also separate the satellite galaxies inside R_{200} (left panels) and outside R_{200} (right panels). The normalization shows equal area between relaxed and disturbed clusters; however, galaxies without gas are not included in the sSFR and metallicity panels.

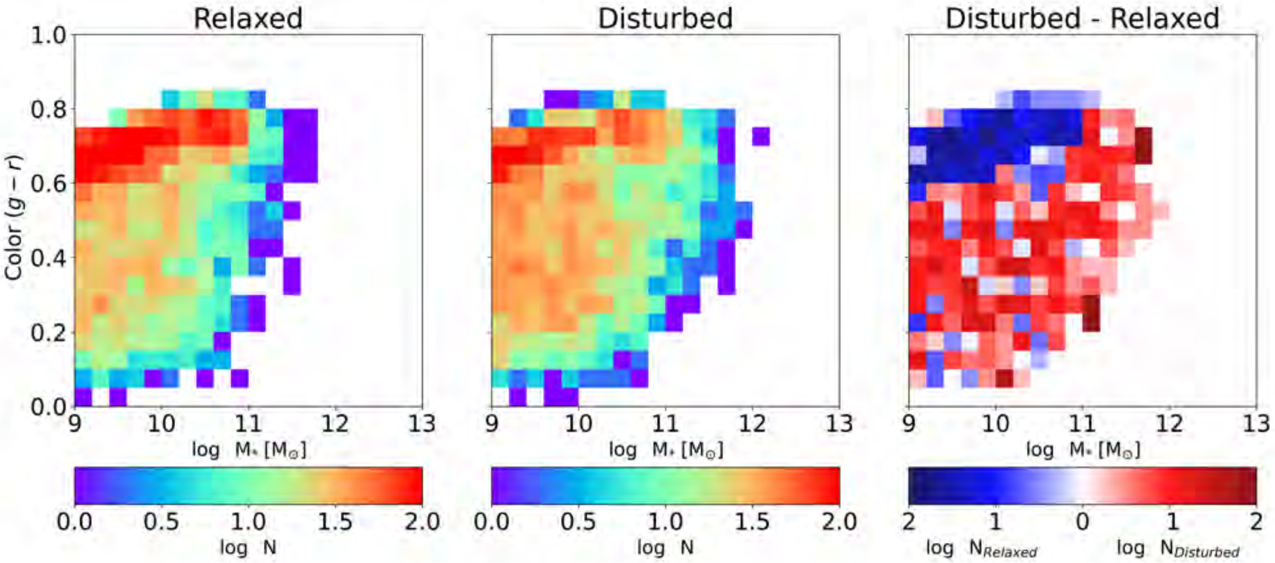

Figure 4.5.2: Colour versus stellar mass diagram distribution of galaxies in relaxed (left panel) and disturbed (middle) panel, respectively. In the left and middle panels we show the satellite galaxy densities distribution for the disturbed and relaxed clusters; whereas in the last panel, we have the difference in the galaxy density between relaxed and disturbed galaxy clusters after normalising. Notice that the sum of the densities in the last panel equals zero. There is an excess of galaxies in the red sequence of the diagram in relaxed clusters compared with the disturbed ones.

R_{200}. In the top panels, we observe a well-defined Red Sequence (RS), centered at ~ 0.7 in colour (g-r), dominating the galaxy distribution, especially in the inner regions of the clusters. However, within R_{200}, the fraction of galaxies in the RS is smaller in the disturbed sample with respect to their relaxed counterpart. The RS peak is also present for galaxies in the outer parts of the cluster (outside R_{200}) but is less noticeable. The differences in the populations between red and blue galaxies are quantified using the threshold derived in Section 4.4.1. The results show that, for the inner parts of the cluster, 70% of galaxies are red in relaxed clusters while 57% in disturbed clusters. Meanwhile, in the outer parts of the cluster, the fraction of the red population decreases to 51% for the relaxed clusters and 42% for the disturbed ones. These results show that the outer parts of clusters have a population of galaxies bluer than those within R_{200}, which are denser environments, and ram pressure stripping is stronger, thus quenching the galaxies more efficiently. Disturbed clusters have more blue galaxies in the outer parts, suggesting a more recent star formation activity in the disturbed clusters. These results agree with those presented by Ferrari et al. (2003), and Łokas (2020), showing that infalling galaxies to the cluster display bluer colours. Meanwhile, the galaxies inside the R_{200} become redder as they spend time interacting with the Intra Cluster Medium (Pallero et al., 2022). As expected, we find that early-type galaxies tend to dominate in the centre of clusters, and late-type galaxy population is more important in the outskirts of clusters (Dressler, 1980). Finally, our results broadly agree with (Soares & Rembold, 2019), which, using data from SDSS III, found that, on average, the stellar populations of galaxies in unrelaxed clusters are younger than in relaxed ones.

In the second row of Figure 4.5.1, we present the distribution of galaxies' sSFR, defined as the Star Formation Rate divided by its stellar mass. Note that not all galaxies are shown in this histogram because galaxies are fully quenched. In fact, 50% of satellite galaxies belonging to relaxed clusters have no gas, and 55% have null star formation. However, in disturbed clusters, we find only 29% of galaxies with no gas and 33% have null star formation. As a result, this plot shows just 50% of satellite galaxies in relaxed clusters and 67% of galaxies in the case of disturbed clusters. However, galaxies without gas are considered for the normalisation of histograms. We clearly note that, in the case of disturbed clusters, a significant fraction of star-forming galaxies are outside R_{200}. Also, in these regions, disturbed clusters have approximately twice as many galaxies with sSFR between $10^{-9.5}$ to $10^{-10.5}$ [yr^{-1}] as in relaxed clusters. However, the sSFR distribution of the star-forming galaxies, is similar for galaxies inside R_{200} for both relaxed and disturbed groups and clusters.

Metal elements are synthesised in the stellar interiors and then redistributed into the Interstellar medium through processes such as SN Type I and Type II and AGB winds. Thus, the gas metallicity provides insights into the star formation history in galaxies (Searle & Sargent, 1972; Nagao et al., 2006). The histograms in the bottom panels of Figure 4.5.1 show the mean gas iron content distribution, denoted as $\log([Fe/H])$ of galaxies in both relaxed and distrurbed clusters. We see that all distributions range from 0 to 0.4 and peak at similar metallicity values $\log([Fe/H]) \approx 0.2$, meaning around 1.6 times the solar metallicity. Also, the distribution of metallicity in relaxed and disturbed clusters is similar for the inner regions of the clusters. We note that, while in the outer cluster region, the distribution is still very similar, we note a larger number of galaxies in the disturbed sub-sample.

To better visualise the differences in the distribution of galaxies in relaxed and disturbed clusters, we present, in Figure 4.5.2, their density distribution in colour (g-r) versus stellar mass, considering all galaxies inside and outside R_{200}. In the left and middle panels, we show the results for the relaxed and disturbed clusters, respectively. Both panels are normalised to have the same number of galaxies. The most representative feature in the two panels is the RS, which is the zone with the higher density of galaxies around $(g-r) \approx 0.7$. This zone is populated by red/elliptical galaxies, whose stellar populations are mainly composed of red and old stars. For this reason, they cover a small range in colour but a larger range in magnitudes. Under the red sequence, we can also identify the blue cloud corresponding to galaxies with recent stellar formation activity. To highlight the difference between those two distributions, we show the residual map in the rightmost panel after subtracting the normalised number between the galaxy population of relaxed clusters from the disturbed clusters in each bin. This panel clearly shows that the red sequence is significantly more populated in relaxed clusters, while the remaining area, including the blue cloud, is more prominent in disturbed clusters. This result means that there is more recent formation activity in the disturbed clusters than in the relaxed ones, or that galaxies in disturbed clusters act as if they are in lower-mass (colliding) clusters.

Figure 4.5.3 presents similar diagrams, but the sSFR versus the stellar mass distribution. Galaxies belonging to relaxed and disturbed clusters are shown in the left and middle panels, respectively. Here, we also include galaxies that have null sSFR with a representative value of 10^{-14} [yr^{-1}]. In those plots, we can see the star-forming main sequence around 10^{-10} [yr^{-1}]. This zone is more populated than other parts of the diagram, except for those that are considered to be fully quenched. However, we notice that it is better defined in the disturbed clusters than in the relaxed ones. We can also identify galaxies with SFR between 10^{-14} [yr^{-1}] and 10^{-12} [yr^{-1}] transitioning from the star-forming zone to the quenched zone. In the right panel, we show the differences between the number of galaxies in relaxed clusters and the number of galaxies in disturbed clusters. We can see that, with respect to the disturbed clusters, the zone of quenched galaxies is more populated by galaxies in relaxed clusters. In contrast, in all other areas, i.e. the star-forming and transition zones, are dominated by the galaxies in disturbed clusters. The distribution of galaxies in Figures 4.5.2, and 4.5.3, and the fact that we observed a clear difference in the fraction of red and quenched galaxies in relaxed clusters and more blue and star-forming galaxies in disturbed clusters, suggests that relaxed clusters are in a more evolved dynamical state than disturbed clusters.

4.6 Redshift Dependence

Several studies suggest that galaxy clusters observed at low ($z < 0.5$) redshifts, exhibit different physical properties than galaxy clusters at higher ($z > 0.5$) redshifts (Butcher & Oemler, 1984; Pallero et al., 2022; Zenteno et al., 2020). The high redshift clusters, particularly their satellite galaxies, tend to have bluer colours and more star formation (Aldás et al., 2023; Zenteno et al., 2020). To explore this reported difference, in this section, we study the quenched fraction of satellite galaxies as a function of redshift and how it depends on the dynamical state of their host groups and clusters.

The left panel of Figure 4.6.1 presents the quenched fraction of satellite galaxies as a function of distance from the cluster centre (in units of R_{200}) for both relaxed and disturbed clusters across different redshift ranges. The galaxies were classified as quenched using the definition provided in section 4.4.2. The fraction of quenched satellite galaxies was computed as the number of passive galaxies divided by the number of all galaxies whose holocentric distances are lower than R. Blue and red lines denote relaxed clusters and disturbed clusters, respectively, and solid lines indicate the results for the low redshifts ($z < 0.5$) subsamples while dashed lines for high redshift ($z \geq 0.5$) subsamples. The shaded regions around each line indicate the uncertainties in the quenched fraction computed under the assumption of a Poisson noise. The left panel shows that quenched fractions decrease with increasing distance from the cluster centre in both relaxed and disturbed clusters, with relaxed clusters consistently exhibiting higher quenched fractions. This trend is more pronounced at low redshifts, indicating

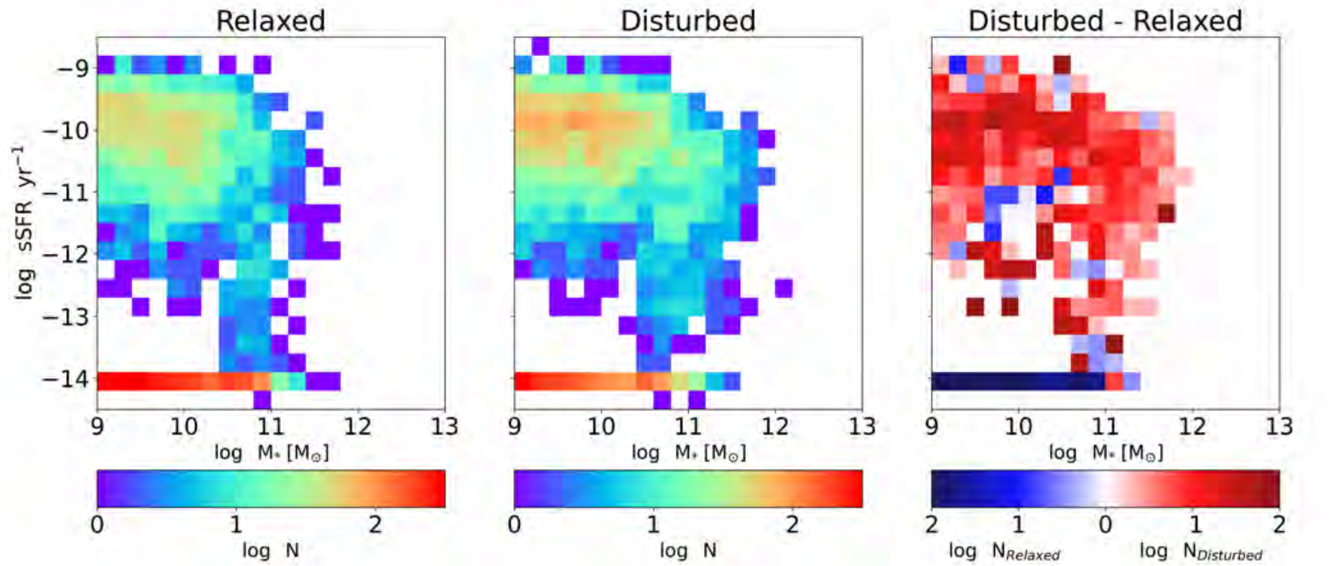

Figure 4.5.3: Specific star formation rate in function of stellar mass diagrams for relaxed halos (left panel), disturbed halos (centre panel), and the difference between relaxed and disturbed halos (right panel). In the last panel, the excess of galaxies bounded to relaxed halos are shown in blue, and the zones of the diagram with an excess of galaxies bounded to disturbed halos are shown in red. There is an excess of quenched galaxies in relaxed clusters compared with the disturbed ones.

that environmental quenching processes are more effective or have had more time to act at these redshifts. Specifically, in the low redshift bin, the fraction of quenched galaxies in the central region of the cluster is approximately 90 %, gradually decreasing to 70% considering all galaxies within a radial distance of 3 R_{200}. Meanwhile, for relaxed clusters, the fraction of quenched galaxies in the central regions is around 80 %, diminishing to 52 %, in the cluster outskirts. On the other hand, in the high redshift bin, both relaxed and disturbed clusters manifest a quenched galaxy fraction of around 75% in their central regions, which subsequently decreases to 54%, taking into account satellite galaxies up 3R_{200} of the relaxed clusters and 36% for disturbed clusters. The higher quenched fractions observed in the central regions of both relaxed and disturbed clusters suggest the presence of strong environmental effects like ram-pressure stripping and tidal interactions close to the cluster core (Boselli & Gavazzi, 2006).

To conduct a more robust comparison between the quenched fraction in relaxed and disturbed clusters, and noting that the quenched fraction consistently exhibits higher values in relaxed clusters compared to disturbed ones, we introduce the concept of the relaxed quenched fraction excess ($f^{\rm rel}_{Q\rm excess}$) following Wetzel et al. (2013), defined as:

$$f^{\rm rel}_{Q\rm excess} = \frac{f^{\rm rel}_{Q} - f^{\rm dist}_{Q}}{f^{\rm dist}_{Q}}$$

The relaxed quenched fraction excess, presented in the right panel of Figure 4.6.1, quantifies the excess (or deficit) of quenched galaxies in relaxed clusters with respect to those typically found in their disturbed counterparts. The right panel shows that quenched fraction excess in relaxed clusters increases with distance from the cluster centre, especially at high redshifts. This suggests, especially at $z \geq 0.5$, that quenching in relaxed clusters is more effective even on the outskirts, potentially impacting satellite galaxies that are on infalling trajectories or those that have been ejected but remain within the cluster's gravitational influence (Bahé et al., 2013). Although the quenching effects are much stronger around R_{200}, Wetzel et al. (2014) show that the environmental quenching could extend up to $2.5 \times R_{200}$ and can be explained by satellites ejected by the cluster. In contrast, at lower redshifts, the excess remains relatively stable, reflecting a sustained quenching effect throughout the cluster's extent. This stability aligns with Pallero et al. (2022), who found that most satellites are quenched during their initial infall, indicating that initial interactions with the cluster environment are crucial for quenching.

In Figure 4.6.2, we show the quenched fraction of satellite galaxies as a function of galaxy stellar mass. At low redshifts, the quenched fraction in relaxed clusters (solid blue line) shows a slight decrease for masses between 10^9 and $10^{10}\mathrm{M}_\odot$, followed by a significant increase with stellar mass, peaking around $\mathrm{M}_* \sim 10^{11}\mathrm{M}_\odot$. The quenched fraction for disturbed clusters at low redshifts (solid red line) follows a similar pattern, but remains consistently lower than in relaxed clusters. This difference is present at low- and high-redshift bins, suggesting that the more stable environments (relaxed clusters) facilitate more effective quenching. We compared our simulated quenched fraction with various observational datasets. For the low-redshift bin, the data from Wetzel et al. (2013) (green circles) correspond to satellite galaxies bound to low redshift clusters (up to $z = 0.06$), based on the NYU Value-Added Galaxy Catalogue from the Sloan Digital Sky Survey (SDSS). These observational results align well with the quenched fraction in relaxed clusters, especially at higher stellar masses, but show discrepancies in the low mass regime. As demonstrated by Donnari et al. (2021), these differences can be attributed to the sample selection. In this context, they illustrated that Wetzel's data could be better replicated by including satellite galaxies bound to lower mass groups ($\mathrm{M}_{200} > 10^{11}\mathrm{M}_\odot$).

Furthermore, comparing with Mcgee et al. (2011) (green stars), using SDSS data at $z \sim 0.08$, it shows that our simulated quenched fractions at low redshift relaxed clusters follow a similar trend. Although their work does not specify any mass cutoff for the galaxy groups, they infer that they are including galaxies belonging to groups with masses $\mathrm{M} > 10^{12.75}\mathrm{M}_\odot$. Therefore, this closer agreement between our simulated quenched fraction and McGuee's observational data is likely due to the better match between the sample selection criteria.

The data from Fossati et al. (2017) (purple circles) correspond to high redshift observations. Specifically, we are comparing the passive galaxy fraction for satellite galaxies with host masses $\mathrm{M} > 10^{13}\mathrm{M}_\odot$ in the redshift range of $0.5 < z < 0.8$. Our simulations reasonably match the observed data, particularly at lower stellar masses. However, the simulations underestimate the quenched fraction in the high mass range. Nevertheless, it is worth noting that the simulation can reproduce a lower quenched fraction in the high redshift bin compared to the low redshift bin at low galaxy mass regimen, as obtained from observational data.

Figure 4.6.2 shows that there is a decrement in the quenched fraction for masses exceeding $10^{11}\mathrm{M}_\odot$. This deviation is due to numerical noise resulting from poor statistics in this mass range. As shown in Donnari et al. (2021), using the significantly larger sample extracted from the TNG300 simulation, considering a similar halo selection criteria and the same criteria to define quenched galaxies. It is worth noting that applying the criteria proposed by Wetzel et al. (2012) to separate between star-forming and passive galaxies (sSFR$< 10^{-11} yr^{-1}$) does not alter our findings and primary conclusions.

In summary, this section's results underscore the influence of the cluster's dynamical state on satellite galaxy quenching. Relaxed clusters exhibit higher quenched fractions at both redshifts, suggesting that stable environments enhance the efficiency of quenching mechanisms. The difference between relaxed and disturbed clusters is more pronounced at low redshifts, where mature clusters have more time to quench their satellite galaxies effectively.

4.7 Gas Content

Here, we analyse the gas content of satellite galaxies within both relaxed and disturbed clusters and groups in the IllustrisTNG simulations. Quantifying the gas in various phases provides valuable insights into the physical mechanisms governing galaxy evolution and could provide important information regarding the cluster's dynamical state (Pillepich et al., 2018a; Nelson et al., 2019). The presence of gas is directly linked to galaxy transformation and evolution. As previously discussed, stellar populations born at different times will have different characteristics depending on the properties of the intra-galaxy gas. For example, gas clouds are progressively enriched with chemical elements, thanks to processes such as SN Type I and II, and winds from AGB stars. As a result, galaxies with ongoing start-formation activity will have not only bluer stellar populations but also different chemical compositions. In dynamical terms, Zhang et al. (2016) showed that merging time scales in galaxy clusters are dependent on their gas content. Clusters with higher gas fractions tend to have shorter merging time scales than those with lower ones. This difference is attributed to the additional gravitational force exerted by the gas, resulting in a quicker infalling of the structures.

To characterise the gas available in galaxies bound to relaxed and disturbed clusters, we classify it into diffuse, condensed,

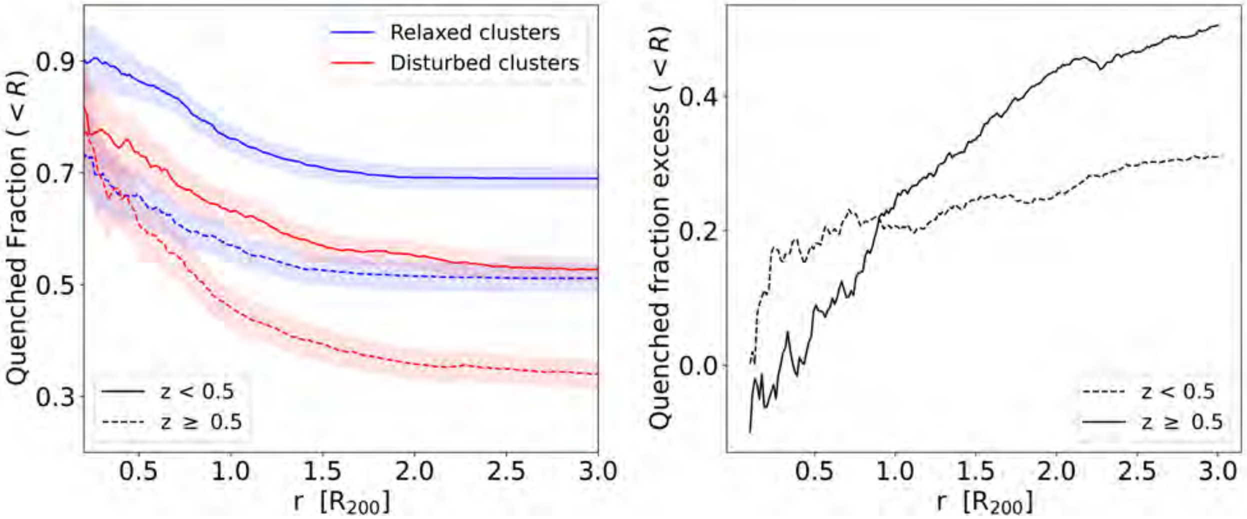

Figure 4.6.1: Left panel: Quenched fraction in the function of the radius from the cluster's centre. In solid lines, the quenched fraction of galaxies that inhabit the low-redshift clusters ($z < 0.5$), and in dotted lines, the fraction of quenched galaxies for clusters in high redshift bins ($z \geq 0.5$). Quenched fractions of galaxies in relaxed clusters are presented in blue, and galaxies inside disturbed clusters are presented in red. The shadow areas are the Poisson's noise. Right panel: Relaxed quenched fraction excess for the high redshift bin in solid line and for the high redshift bin in dotted line.

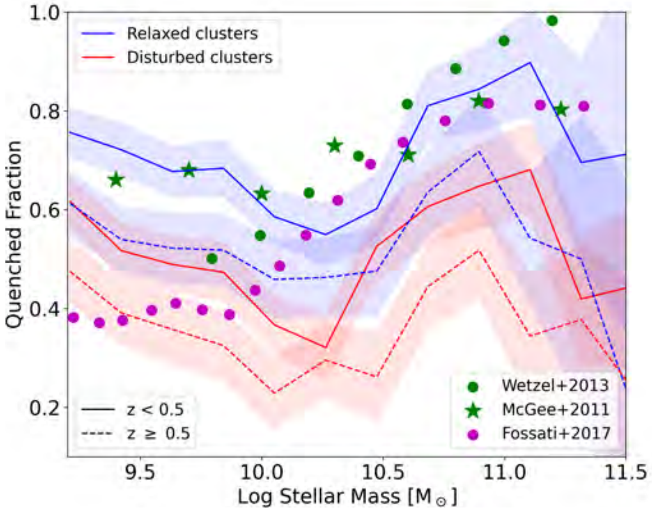

Figure 4.6.2: Quenched fraction of galaxies as a function of stellar mass. In blue, we present the galaxies bounded to relaxed halos, and in red, we present the galaxies bounded to disturbed halos. We separated our sample between low ($z < 0.5$) redshift sample shown in solid lines and high redshift ($z \geq 0.5$) bins shown in dashed lines. The shadow areas represent the uncertainty computed using Poisson's noise. Comparing the subsamples at the same redshift, the relaxed groups and clusters always have more quenched galaxies than disturbed ones.

and hot phases based on density and temperature. The temperature of the gas is calculated for each gas cell using the internal energy μ and the Electron Abundance ($x_e = n_e/n_H$), provided in the simulation outputs with the following equation

$$T = (\gamma - 1)u/k_B \times \mu.$$

Here k_B is the Boltzmann constant, $\gamma = 5/3$, $X_H = 0.76$, m_p is the proton mass, and μ the mean molecular weight, defined as:

$$\mu = \frac{4}{1 + 3X_H + 4X_H x_e} \times m_p$$

The classification of the different gas phases applied here is based on the boundaries proposed by Torrey et al. (2012) and Torrey et al. (2019). Gas is considered hot if $\log(T/10^6 K) > 0.25\log(n_H/405cm^{-1})$, where n_H is the gas density expressed in units of atoms of Hydrogen per unit of cubic volume. Gas not meeting this condition is further categorised as diffuse if its density is $n_H < 0.13cm^{-1}$, and as condensed if its density is greater than $n_H > 0.13cm^{-1}$.
In Figure 4.7.1, the four panels show the distribution of gas related to galaxy clusters in different categories based on their dynamical state (relaxed or disturbed) and redshift (low or high). Those diagrams were obtained by adding together all of the gas particles bound to the cluster galaxies, excluding the gas of the BCG. The x-axis represents the logarithm of gas density (n_H in cm^{-3}), and the y-axis displays the logarithm of gas temperature (T in K). Each panel is color-coded to represent the amount of gas, with blue indicating lower gas quantities and red indicating higher quantities. Additionally, each diagram includes the percentages of gas in the different phases relative to their total and the average amount of gas per galaxy in the corresponding phase per galaxy satellite. The dashed lines demarcate the boundaries between the different gas phases.

Figure 4.7.1 allows us to understand the relationship between the amount of gas available and the dynamical state of the clusters. Satellite galaxies in groups and clusters contain significant amounts of gas across all gas phases. When comparing satellite galaxies in relaxed and disturbed clusters, it is evident that disturbed clusters contain more gas in the hot phase in both low- and high-redshift bins compared to the relaxed ones. The difference in the hot gas fraction is quite substantial, with 28% for relaxed clusters and 76% for disturbed clusters in the low-redshift bin. In the high-redshift bin, the hot gas fraction is 30% for relaxed clusters and 61% for disturbed clusters. It is important to note that not only is the fraction of hot gas greater in disturbed halos, but more importantly, the average mass per galaxy is much higher.

We now look at the diffuse gas phase, corresponding to cold gas cells with a density lower than that required to form stars. In this phase, disturbed clusters have a significantly higher average amount of gas per galaxy than relaxed clusters despite having a lower diffuse gas fraction. For instance, in the low redshift bin, there is 2.6 times more diffuse gas in galaxies belonging to disturbed clusters compared to relaxed ones. This difference is also observed in the high redshift bin, where disturbed cluster galaxies have 2.2 times more diffuse gas available than relaxed ones. It is crucial to quantify the availability of gas in this phase because, during cluster mergers, the gas can be compressed in the front half of galaxies due to ram pressure (Schaye et al., 2015; Troncoso-Iribarren et al., 2020). This can lead to a burst of star formation and gas transfer to the trailing half of galaxies. Using EAGLE simulations, Troncoso-Iribarren et al. (2020) concluded that this effect is more important for galaxies with stellar masses lower than $10^{10.5}$ $M_\odot$ located near R_{200}. This enhancement in star formation in infalling galaxies was observationally confirmed by Roberts et al. (2022) studying the cluster IC3949 using data from the ALMA MaNGA survey. Galaxies with stellar masses larger than this mass range tend to arrive in their final cluster already preprocessed and quenched by their active galactic nuclei (AGN). Additionally, these galaxies may have very little gas in the diffuse phase, as most of it is heated by the AGN. Consequently, gas compression does not play a significant role in this mass range.

The condensed gas phase is the one that has the pressure and density to begin forming stars. This gas phase distribution has a characteristic thin shape in the density-temperature phase diagram, governed by the Springel & Hernquist (2003) state equation, as shown on the right side of the plots in Figure 4.7.1. The amount of available condensed gas per galaxy in disturbed clusters is around 1.5 times the amount of gas available in relaxed ones. As a result, on average, the star formation rate is higher in disturbed galaxy clusters than in relaxed counterparts. This ongoing star formation can explain the presence of a more diverse galaxy population and the excess of blue galaxies found in disturbed clusters compared to the relaxed ones presented in Section 4.5. This difference is present in both redshift bins. However, it is more pronounced for galaxy clusters in the high redshift bin, suggesting that the excess of blue and young galaxy population is likely more significant in the case of clusters between $0.5 < z < 1$. This result agrees with Chapter 3, where we observed that the galaxies are bluer in the disturbed galaxies for this redshift range.

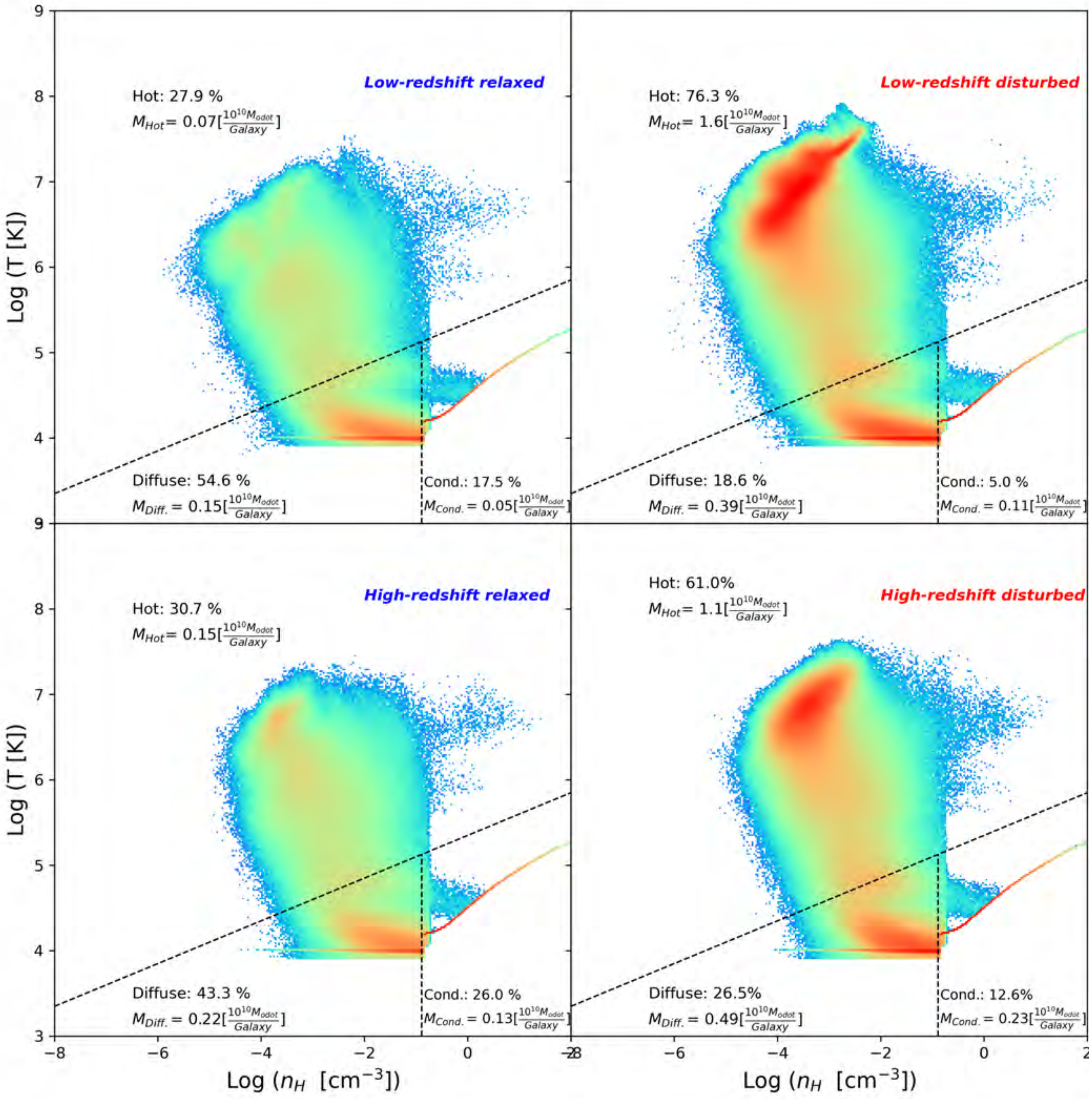

Figure 4.7.1: Gas content of the satellite galaxies in relaxed (left panels) and disturbed clusters (right panels), for low- (upper panels), and high-redshift (bottom panels). Each panel shows the gas content for each gas phase: hot, diffuse, and condensed. On average, galaxies in disturbed clusters have more gas than galaxies in relaxed ones. We also can see that galaxies in disturbed clusters have more hot gas due to the inclusion of the secondary BCG and the gas heat suffered during the interaction.

The differences in the hot gas fraction found between the relaxed and disturbed clusters presented in Figure 4.7.1 can be explained by either a more massive population of galaxies in the disturbed cluster (containing a larger amount of hot gas), as described by Torrey et al. (2019), or by gas shock heating mechanism during cluster interactions, injecting energy into the gas reservoir. To understand the cause of this difference and to make a more fair comparison between the relaxed and disturbed clusters, in Figure 4.7.2, we present plots analogous to those in Figure 4.7.1 but now also excluding the BCG belonging to the secondary structure falling to the main cluster. This difference could be the result of the gas heating during the merger.

A primary distinction evident upon comparison between both figures lies in the hot gas phase, where the large amount of hot gas with high temperature and low density, observed in Figure 4.7.1 becomes less pronounced when excluding the BCG from the secondary galaxy cluster. Consequently, the hot gas fraction in disturbed clusters decreases from 70% to 35% for low-redshift disturbed clusters and from 60% to 30% for high-redshift disturbed clusters. Despite this, the fraction of hot gas in disturbed clusters remains larger than that measured in their relaxed counterparts.

Finally, we examine the gas-to-stellar mass ratio, hereafter referred to as the gas ratio. In this analysis, we include gas cells bound to all satellite galaxies, excluding the BCG in relaxed clusters and the main and secondary BCGs in disturbed ones. The gas ratio parameter is calculated by adding up the mass of all gas cells within a given cluster centric radius R, and dividing it by the total stellar within the same volume. The gas ratio provides insights into the baryon content of the satellite galaxies bounded to the clusters in different dynamical states. This ratio is also closely linked to ram pressure, the predominant mechanism of gas stripping for galaxies in a dense environment like clusters (Jung et al., 2018). The results are presented in Figure 4.7.3, where we show the mean gas ratio for different gas phases: hot gas in the top panel, diffuse gas in the middle panel, and condensed gas in the bottom panel, all as a function of the cluster centric distance. The figure shows that the hot gas bounded to galaxies within R_{200} is relatively sparse in relaxed clusters, while it is slightly larger in disturbed clusters at the same redshift. This difference in the hot gas mass ratio between relaxed and disturbed clusters becomes more pronounced in the outer regions of galaxy clusters, where the presence of hot gas is larger in disturbed clusters, likely due to the accretion shocks (Cole et al., 2000). The middle panel shows the diffuse gas mass ratio, which is also primarily found in galaxies located in the outer parts of the clusters but closer to the cluster's centre than the hot gas. This panel also indicates that galaxies in relaxed clusters have a larger diffuse gas ratio in disturbed clusters compared to relaxed ones. Finally, the bottom panel shows the condensed gas distribution, predominantly located in the galaxies in the central regions of clusters. For the high redshift bin, the condensed gas ratio rises sharply at small radii and then stabilises, whereas in the low redshift bin, the ratio is relatively flat and minimal. These findings are consistent with the notion that, at lower redshifts, most galaxies are already quenched by the time they are incorporated into their final host clusters (Pallero et al., 2022).

Furthermore, these results align with the observations made by Stroe et al. (2014), who, using optical spectroscopic data for the clusters CIZA J2242.8+5301 and 1RXS J0603.3+4213, demonstrated that mergers in gas-rich clusters lead to increased star formation rates. This increase is attributed to shock waves that compress the gas of the cluster galaxy members during these mergers. This finding is also in agreement with the results of the Chapter 3, in which we observed an excess of blue galaxy population in disturbed clusters in the high redshift bin compared to relaxed ones. In contrast, differences for galaxies in the low-redshift bin were within the error, suggesting a convergence in galaxy properties at lower redshifts.

It is worth noting that by including the secondary BCG in disturbed clusters, the results for the condensed and diffuse gas ratio are not affected. However, a significant increase in the hot gas ratio is observed, as illustrated in Figure 4.7.1. This indicates that the secondary BCG is primarily composed of hot gas while containing minimal amounts of diffuse and condensed gas. These results support the idea that the populations of galaxies can provide relevant information about the cluster's dynamical state, especially when both BCGs of the merging system are removed from the analysis.

4.8 Star Formation burst and post quenching.

To delve into the origins of the differences in galaxy populations described in Section 4.5, specifically the higher fraction of blue galaxies in disturbed clusters compared to relaxed clusters, this section explores the star formation history and gas mass distribution in disturbed galaxy clusters during the merging process. In this analysis, we studied four representative disturbed clusters at different stages of interaction: two clusters where the structures are approaching but have not yet crossed R_{200} and two clusters in a more advanced merging stage where the secondary structure has already crossed R_{200} of the main one. The

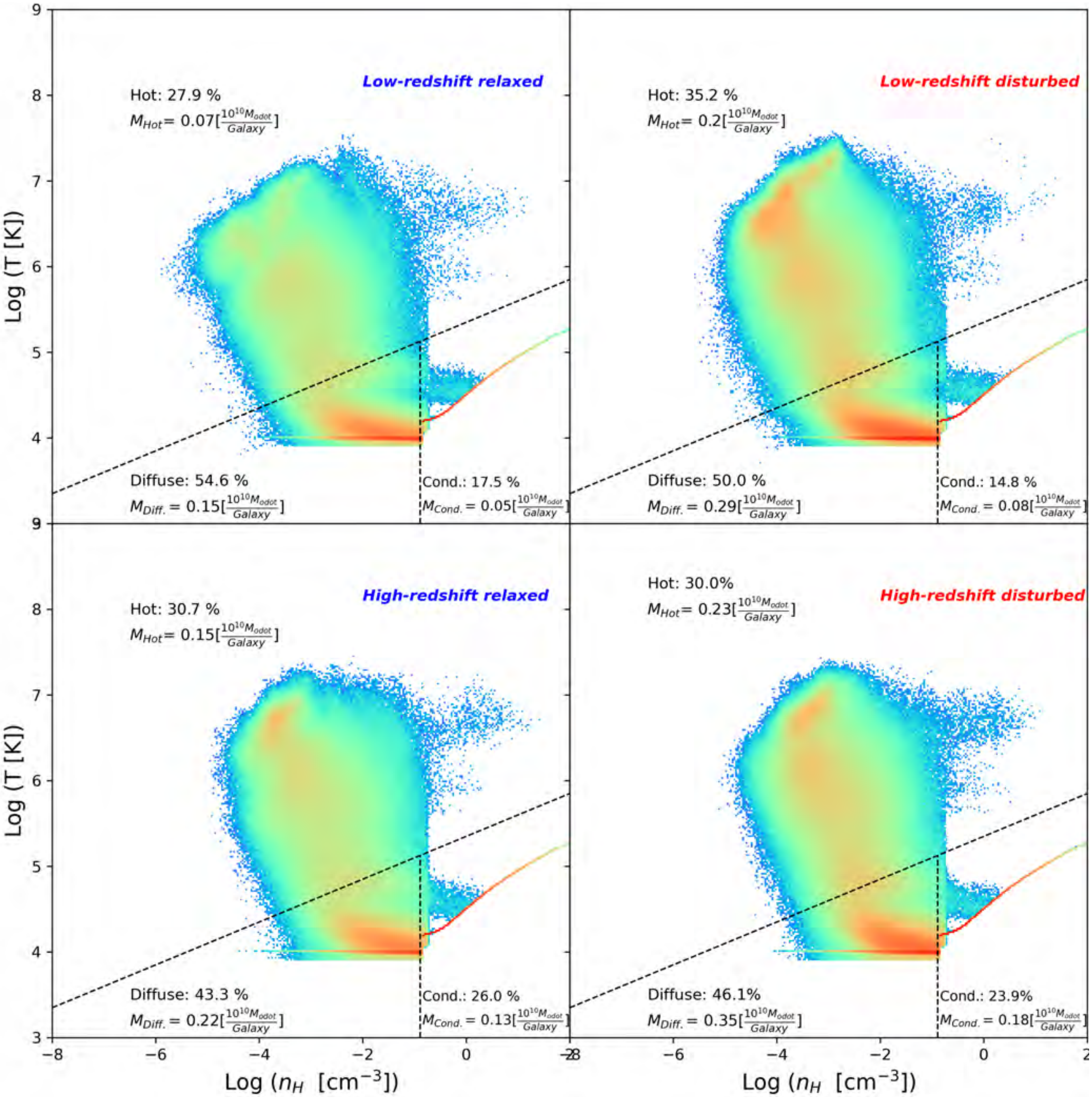

Figure 4.7.2: Gas content of the satellite galaxies in relaxed (left panels) and disturbed clusters (right panels), for low- (upper panels), and high-redshift (bottom panels). In those panels, in contrast to Figure 4.7.1, we exclude the second BCG in the case of disturbed halos. Each panel shows the gas content for each gas phase: hot, diffuse, and condensed.

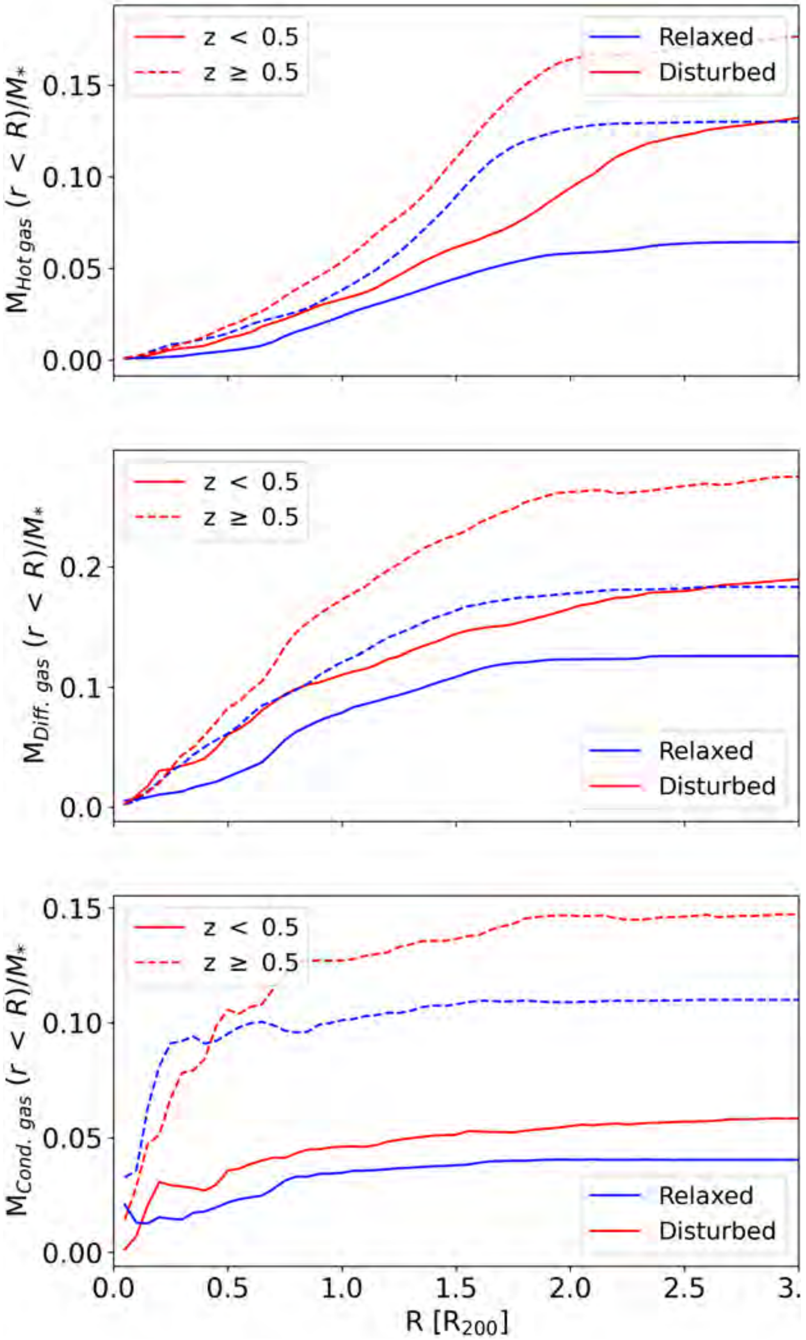

Figure 4.7.3: Gas fraction as a function of the radius. In the top panel, we have the hot gas as a function of the radius. In the middle panel, we present the warm gas as a function of the radius, and in the last panel, we present the condensed gas, which represents the star-forming gas.

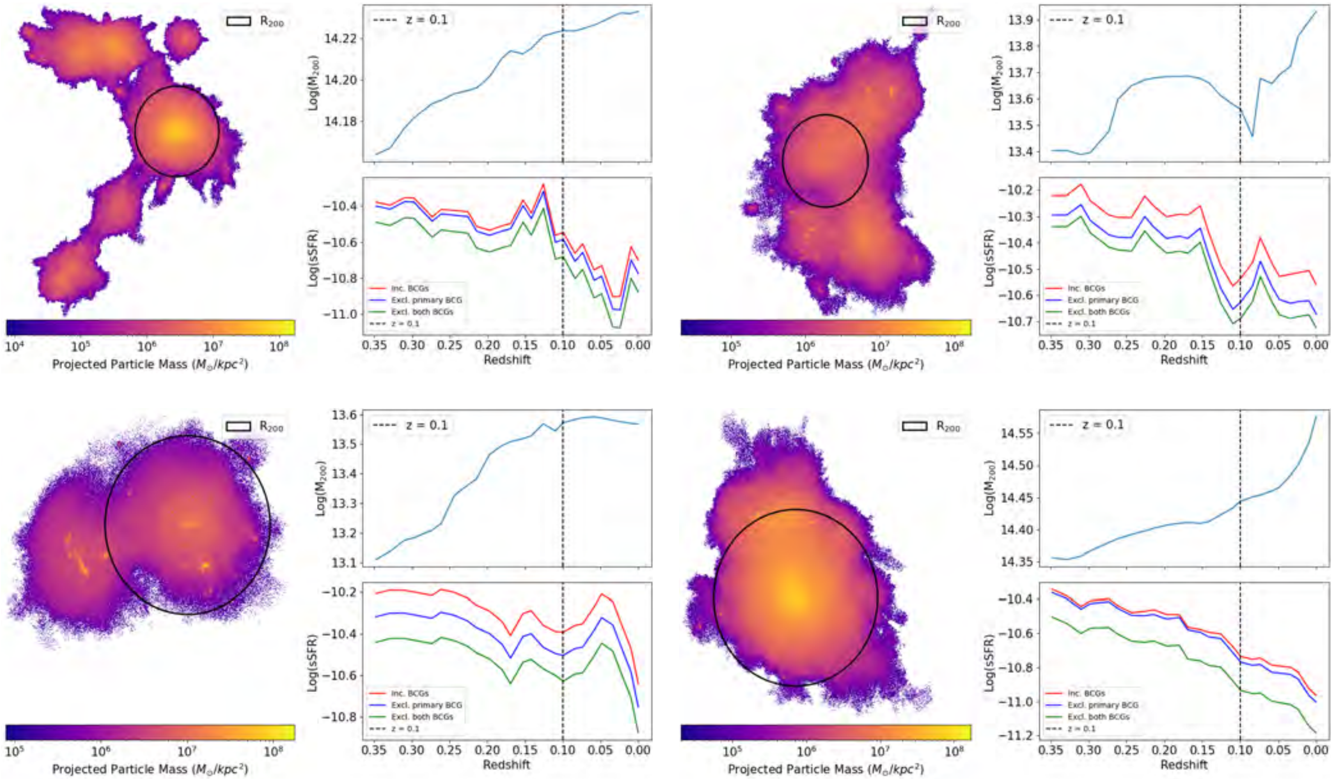

Figure 4.8.1: We present the four selected disturbed galaxy clusters at redshift $z = 0.1$; the top ones are clusters in the early interacting stages, while the bottom panels show clusters in more advanced interacting stages where the secondary structure has already crossed R_{200} of the main one. On the left side, the projected gas mass distribution for redshift $z = 0.1$. On the right side, we have the temporal evolution of total virial mass M_{200} and the sSFR of their satellite galaxies. The clusters exhibit a short boost followed by a decrease in the sSFR, indicating that the sSFR's dynamical state may be influenced by the cluster's dynamical state.

clusters were selected at redshift $z = 0.1$ to provide insights into the later stages of galaxy and cluster evolution as they are closer to their present-day configurations. In Figure 4.8.1, we explore the evolution of these clusters as a function of time. On the left side of each panel, we show their projected gas mass distribution at $z = 0.1$, with a solid line circle representing R_{200} of the main cluster. It is evident that all four clusters are indeed disturbed; however, those in the top panels are in the early stages of interaction, whereas those in the bottom panels are in a more advanced merging stage. The gas morphology in these clusters is irregular and clumpy, showing two or even more structures interacting. Some gas clouds might appear elongated or have comet-like shapes with tails pointing away from the dense central regions, highlighting the effects of ram pressure stripping. On the top right of each panel, we show the time evolution of the cluster's virial mass, M_{200}, of the main structure, computed as the total mass within R_{200} shown in the left panel. The dotted lines in those panels indicate the redshift of the shown gas distribution. We note that the virial mass increases over time, reflecting the hierarchical nature of structure formation in the universe, where small structures merge to form larger ones. The virial mass plots show pronounced raises toward lower redshifts, consistent with their merging nature. Aditionally, the bottom right side of each panel shows the integrated sSFR of the satellite galaxies as a function of redshift. This integrated sSFR is computed considering both BCGs (red), excluding the primary BCG (blue), and excluding both BCGs (green). The presence of peaks and subsequent rapid decreases observed in the sSFR in most clusters shows that it can be influenced by dynamical processes like mergers. The asymmetric gas distributions and gas tails in cluster galaxies have been associated with an enhancement in the star formation rate, which is produced by the gas compression in the leading edge of the galaxies (Safarzadeh & Loeb, 2019; Vulcani et al., 2020; Rohr et al., 2023). It's been suggested that, initially, a merger can trigger star formation by compressing the gas, but gas stripping and heating due to the interaction quench the galaxy over time, as shown in Figure 4.8.1. These results agree with Fujita & Nagashima (1999), who studied the impact of ram pressure on the SFR of satellites in clusters. They found that the SFR increases by a factor of two when galaxies reach the first pericenter passage, given the gas compression. However, after this point, there is a rapid quenching due to the effect of ram pressure near the central regions, resulting in the stripping of the cold gas and, thus, the depletion of molecular gas. This scenario for gas-rich merging clusters was also reported by Stroe et al. (2014), suggesting this short star formation rate increase could last just a few 100 Myr.

Our results complement those presented by Contreras-Santos et al. (2022) who, using the Three Hundred Simulations, found a slight increase of young stars in the BCGs after cluster mergers. They found that the merger-induced star formation rate was also accompanied by an increase in the luminosity and an excess of blue BCGs in the disturbed cluster sample compared than with the relaxed one. The same trend described for those four clusters presented in Figure 4.8.1 is observed in around 75% of disturbed clusters at redshift $z = 0.1$. This is a first boost in star formation rate when the clusters start to interact, followed by a cessation of star formation while the cluster reaches a relaxed state. The process involved in boosting the star formation rate and post-quenching will be studied and quantified more deeply in a follow-up article.

4.9 Summary and Conclusions

In this study, we used the Illustris TNG100 simulations to investigate the relationship between the dynamic state of galaxy groups and clusters and the physical characteristics of their galaxy population. We selected a sample of groups and clusters with masses $M_{200} \geq 10^{13}$ $M_{\odot}$ and classified them between disturbed and relaxed based on the offset between the position of the Brightest Cluster Galaxy (BCG) and the position of the center of mass of the gas cells. Clusters were considered disturbed if this offset is larger than $0.4 \times R_{200}$. We identified 153 disturbed galaxy clusters within a redshift range of $0.1 < z \leq 1$ and compared them with an equivalent set of the 153 most relaxed galaxy clusters. We also divided our sample into high- and low-redshift structures to analyse the evolution of those properties.

Galaxies in each subsample were classified as red and blue galaxies using a double Gaussian fit for the galaxies' colour distribution. The fits were performed for the high and low z groups and clusters. We also separated between quenched and star-forming galaxies following Donnari et al. (2019). Our analysis shows that the physical properties of satellite galaxies, such as colour, star formation rate, and gas availability, depend significantly on the relaxation state of their host clusters. Specifically, we found that clusters in a disturbed state have a higher fraction of blue galaxies and a lower fraction of quenched galaxies compared with their relaxed counterparts. We also find a significant dependence of the fraction of red galaxies and quenched galaxies with redshift of the cluster. We observed a higher proportion of blue galaxies and larger star formation activity at higher redshifts. The higher sSFR observed in galaxies bound to disturbed clusters aligns well with the study conducted by Cohen et al. (2015). In their study, they analysed a sample of 379 galaxy clusters from the Sloan Digital Sky Survey, revealing an inverse correlation between the relaxation state of galaxy clusters and SFR. Those results are also consistent with Pallero et al. (2022). Using sample zoom-in simulations of galaxy clusters, they showed that, at low z, a large fraction of the present-day cluster galaxy population arrives at the cluster pre-processed, regardless of the cluster mass. However, at higher z most galaxies reach their quenching state in situ, regardless of the cluster mass. As a result, even massive clusters show a significant star-forming galaxy population that undergoes a rapid quenching phase after reaching the cluster R_{200}. Also, those results are consistent with Chapter 3, in the sense that in high and low redshifts, the galaxy population is more mixed in the disturbed clusters than in the relaxed ones, but the difference is more pronounced at high redshifts.

We have also explored the differences in gas availability among galaxies bound to relaxed and disturbed clusters. The results show that galaxies in disturbed clusters consistently have higher quantities of gas in all phases - hot, diffuse, and condensed - compared to galaxies in relaxed clusters. The large amount of condensed gas can explain the higher star formation rate found in disturbed clusters and the lower fraction of quenched galaxies. The presence of more hot gas can be explained by the presence of shocks produced during the merging.

Finally, we found that during the initial phases of cluster mergers, the specific star formation rate (sSFR) rises, likely due to gas compression resulting from the shocks generated during the merging process of clusters. As the galaxy cluster becomes more relaxed, star formation slows down, and galaxies become less active in forming new stars. These findings have significant implications for our understanding of galaxy evolution, highlighting the dynamic nature of star formation and the role of gas distribution in this process. To understand why this happens during mergers, we need to track and estimate the tidal forces and ram pressure stripping acting on galaxies, which will be done in a follow-up work.

Chapter 5

X-rays mocks and scaling relations using Illustris-TNG300 and Millenium-TNG simulations.

Abstract

The main baryonic component of galaxy clusters is the hot ionised gas that emits in X-rays. X-ray observations are one of the most important tools for the study of galaxy clusters. In this chapter, we aim to produce a pipeline to create galaxy cluster X-ray mocks to study the differences in the scaling relations between relaxed and disturbed clusters at redshift $z = 0$ using the Illustris TNG-300 and Millennium TNG-740 full-physics simulations. To validate our pipeline, we obtained scaling relations between L_X and M_{500} for a wide range of masses between $10^{12.5} M_\odot < M_{500} < 10^{15.5} M_\odot$, which are consistent with those obtained observationally. We also show that the derived scaling relations can be fitted using a broken power law with a pivot located at $10^{14} M_\odot$. The slopes obtained from the fit to the large mass clusters, $M > 10^{14} M_\odot$, are consistent with the values theoretically derived by using the self-similarity assumption. After that, our sample was divided into relaxed and disturbed galaxy clusters to examine variations in parameters commonly derived from X-ray mocks, such as concentration index, centroid offset and power ratios. Finally, we investigated the differences in the scaling relations between relaxed and disturbed galaxy clusters. [1]

---

[1] Based on Aldás, Gómez, Springel, Pakmor, et. al, 2024, in prep.

5.1 Introduction

Under Λ-CDM model, structures in the Universe grow in mass in a hierarchical way (White & Rees, 1978). In this framework, small initial density fluctuations in the early Universe, amplified by gravitational instability, lead to the formation of the first bound structures, small dark-matter halos. These small halos merge and accrete additional matter over time, gradually forming larger and more massive structures. This process continues in a bottom-up fashion, forming groups and clusters of galaxies (Press & Schechter, 1974). In this sense, galaxy clusters are the larger collapsed and the ones of the more recently formed structures. These massive structures, which contain hundreds to thousands of galaxies, offer insights into the large-scale structure of the Universe, the distribution of dark matter, and the baryonic processes that govern galaxy formation and evolution. Among the most powerful tools for studying galaxy clusters are X-ray observations. X-rays are particularly effective because the emission is proportional to the square of the gas density, thus minimising susceptibility to line-of-sight projection effects (Ramos-Ceja et al., 2019). The analysis of this X-ray emission provides critical information about the physical conditions within galaxy clusters, such as temperature, gas density, and metallicity profiles, which are key to understanding the thermodynamic state of the intracluster medium (ICM) and the assembly history of clusters (Voit, 2005).

However, interpreting X-ray observations presents significant challenges. The ICM is influenced by various astrophysical processes, including radiative cooling, heating by active galactic nuclei (AGN), and turbulence, all of which can affect the observed X-ray properties (McNamara & Nulsen, 2007; Gaspari et al., 2014). Additionally, the assumption of hydrostatic equilibrium may introduce biases in mass estimates, especially in disturbed clusters where non-thermal pressures or bulk motions are significant (Nagai, 2006). The fraction of disturbed clusters, or clusters undergoing a merging process, is not negligible. In fact, between 10 and 20 % of them are undergoing mergers. (Arendt et al., 2024).

There are many proposed proxies widely used in X-ray observations to estimate the dynamical state of galaxy clusters. These parameters are based on the morphology of the cluster: including the concentration index, which measures the core-to-total emission ratio (Fabian, 1994; McDonald et al., 2012); the centroid shift, which is the standard deviation of the projected separation between the X-ray peak and the centroid of the X-ray surface brightness computed within different apertures (Mohr et al., 1993; Kolokotronis et al., 2001); and the power ratio, defined as the ratio between coefficients derived from the multipolar expansion of the emission of the cluster (Buote & Tsai, 1995; Bauer et al., 2005). Furthermore, Yuan & Han (2020) showed that the dynamical state cannot be represented by a single parameter, proposing a new one to improve the estimation of that state based on a profile proxy, which describes the morphology of the cluster, and an asymmetry parameter.

The objective of this Chapter is to present a pipeline to generate mocks of X-ray emission for the Illustris-TNG and Millenium-TNG simulations. We validated the simulated emission maps by comparing the luminosity scaling relation with observational data. We also studied the correlations among the most commonly used parameters to describe the galaxy clusters' dynamical state. Finally, we study the impact of the cluster's dynamical state on the scaling relations of galaxy clusters. This Chapter is structured as follows. Section 5.2 presents the simulation we use, Section 5.3 presents the pipeline used to generate the X-ray mocks, Section 5.4 presents the scaling relations, and Section 5.5 presents the differences in the derived properties between relaxed and disturbed samples.

5.2 Simulations

Hydrodynamical cosmological simulations are crucial to study the formation and evolution of cosmic structures in the Universe. These simulations incorporate dark matter, which serves as the backbone of structure formation, dark energy, which drives the expansion of the Universe, and the baryonic component, which, although constituting only a small fraction of the Universe's matter-energy content, involves complex nonlinear processes such as gas cooling, star formation, supernovae and AGN feedbacks, among others (Vogelsberger et al., 2020). In this Chapter, we used two full-physics and high-volume cosmological simulations: the IllustrisTNG 300 hereafter TNG300 (Marinacci et al., 2018) and the MilleniumTNG 750 hereafter MTNG (Pakmor et al., 2023) simulations. Both simulations, TNG300 and MTNG, use the AREPO code, which incorporates a moving mesh approach to solve hydrodynamical equations with a finite-volume method (Springel, 2010).
TNG300 is part of the Illustris TNG simulation suite, which is a set of fully hydrodynamical cosmological simulations with different box sizes and particle mass resolutions (Marinacci et al., 2018; Naiman et al., 2018; Nelson et al., 2018; Pillepich et al., 2018b; Springel et al., 2018). This suit includes three simulations: Illustris TNG-50, TNG-100, and TNG-300, each

having a box size of 50, 100 and 300 Mpc, respectively. Smaller boxes have better particle resolutions but smaller and less massive structures. In fact, TNG50 only has 23 halos with masses larger than 10^{13} $M_{\odot}$, while we find 168 in TNG100 and 3545 in TNG300. As the main focus of the Chapter is on the mas distribution of massive objects, we use the TNG300. The resolution of the baryonic mass in TNG300 is $1.1 \times 10^7 M_{\odot}$, with a softening length of 370 pc, while the resolution for the DM particles is $5.9 \times 10^7 M_{\odot}$, with a softening length of 1480 pc (Marinacci et al., 2018; Nelson et al., 2019). The TNG300 model can reproduce notably well the distribution of several observed properties in galaxies such as the bimodal colour distribution (Nelson et al., 2018), the galaxy and halo mass functions (Pillepich et al., 2018b), the evolution of abundances of chemical elements in the intra-cluster medium (Vogelsberger et al., 2018), the fraction of quenched galaxies in different environments up to redshift $z \sim 2$ (Donnari et al., 2019, 2021), and the excess of blue galaxies in disturbed galaxy groups and clusters in comparison with relaxed ones (Aldás et al., 2024, 2023), among other properties consistent with observational results.

Millenium TNG is a new suite of simulations that includes one hydrodynamical simulation and a series of DM-only simulations, all sharing the same box size but varying in the number of DM particles. This suite is designed to investigate baryonic physics on large scales, such as galaxy clusters and the cosmic web (Pakmor et al., 2023). In this Chapter, we use the flagship hydrodynamical simulation of the suite, hereafter referred to as MTNG. MTNG was run with a periodic box of 750 Mpc per side using 4320^3 DM particles and an identical number of gas cells. MTNG has a softening length of $\varepsilon = 370 pc$. Each DM particle has a mass of 1.7×10^8 $M_{\odot}$, and the gas cells contain $3.1 \times 10^7 M_{\odot}$ (Hernández-Aguayo et al., 2023; Pakmor et al., 2023). The galaxy formation physics model and also the cosmological parameters of MTNG are the same as the one used in IllustrisTNG. The MTNG box is 15 times larger in volume than TNG300, allowing us to have a sample of 9 galaxy clusters with masses larger than 1×10^{15}, 1500 galaxy clusters with masses larger than 10^{14} $M_{\odot}$, and 38000 clusters with masses larger than 10^{13} $M_{\odot}$ at redshift $z = 0$, all maintaining a mass resolution comparable to TNG300. The combination of TNG300 and MTNG enables a detailed analysis of the scaling relations and study the X-ray emission of galaxy clusters in a wide range of masses, between $10^{12.5}$ - $10^{15.5}$, $M_{\odot}$ and the X-ray luminosity, between $10^{40} - 10^{45}$ erg s^{-1}. This Chapter, as in TNG300 and MTNG, uses the same Planck Collaboration (2016) cosmology given by: $\Omega_0 = 0.3089$, $\Omega_b = 0.0486$, $\Omega_\Lambda = 0.6911$, and $h = 0.6774$.

5.3 X-ray mocks

Observations of galaxy clusters have unveiled an extended X-ray emission, with overall luminosities ranging from 10^{42} to 10^{45} erg s^{-1}. This emission is attributed to the presence of hot gas, which is the dominant phase in galaxy clusters, in their Intra Cluster Medium (ICM). This gas component constitutes about 10-15% of the total cluster mass and represents the majority of the baryonic matter (Allen et al., 2011). In clusters, gravity compresses the gas and, along with processes such as shock heating, raises its temperature to around 10^7 - 10^8 K. At those temperatures the ICM is fully ionised (Shimizu et al., 2003). To generate the mocks of X-ray emission, we assume that the ICM is well-described by an optically thin medium (Mewe, 1998). Consequently, the emitted spectrum from the hot gas is a combination of thermal bremsstrahlung and the line emission of highly ionised elements (Gilfanov et al., 1987). We generate X-ray emission mocks for galaxy clusters in TNG300 with masses $M_{500} \geq 10^{12.5} M_{\odot}$, and for clusters with masses $M_{500} \geq 10^{13} M_{\odot}$ in MTNG following the pipeline proposed by Barnes et al. (2021). Here, M_{500} is the mass contained within a spherical volume where the mean density is 500 times the critical density of the Universe. This procedure can be summarised as follows: First, i) we compute the cooling function $\Lambda(T, Abund)$, then, ii) we compute the emission measure, and finally, iii) we compute the X-ray luminosity. Each step is described in detail in the following paragraphs:

i) *The cooling function* $\Lambda(T, \mathrm{Abund})$ represents the rate at which the ICM radiates energy. This function depends on its temperature and chemical abundance patterns. Therefore, since each gas cell has its own temperature and chemical abundance, it is necessary to simulate the X-ray emission spectrum for each gas cell. This spectrum can be generated using APEC, a code designed to model UV and X-ray emission for collisionally excited plasmas (Brickhouse et al., 2005). The model can be accessed using the Python package pyatomdb. However, since most massive galaxy clusters in TNG300 and MTNG are resolved with more than 10^7 gas particles, generating a spectrum for each particle using `pyatomdb` is computationally non-viable. To address this, we generate spectra for each chemical element traced in TNG300 at predefined temperature values, specifically ranging from 10^5 to 10^9 K in increments of $10^{0.02}$. The final spectrum is then computed as a linear combination

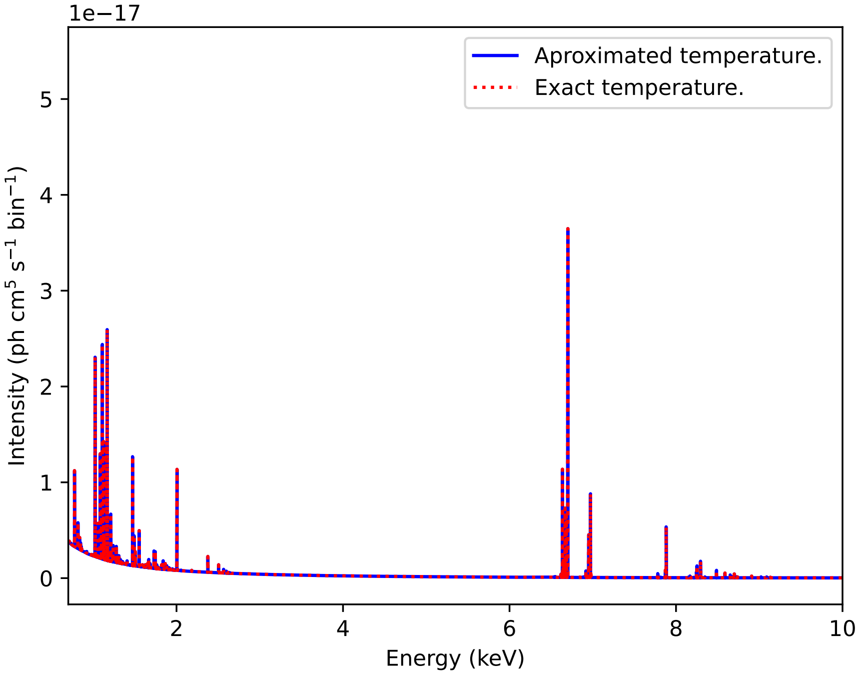

Figure 5.3.1: Spectrum for a value of temperature $Log(T) = 7.82$. In blue, we have the spectrum computed using pyatomdb. In red, the spectrum is computed using a linear combination of the individual spectrums for each element weighted by their abundance.

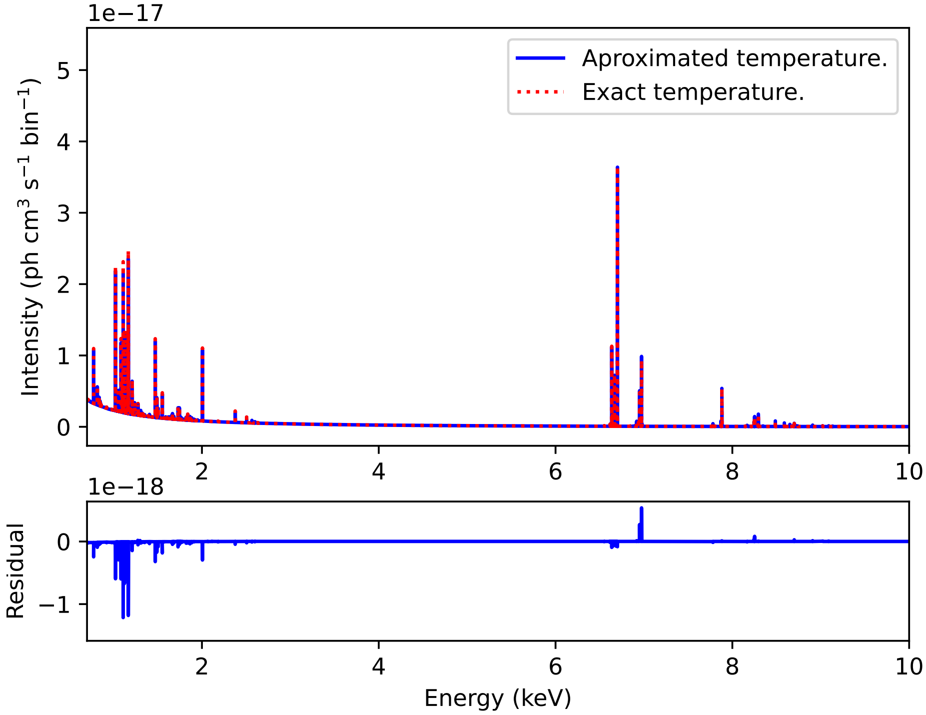

Figure 5.3.2: In the top panel, we have the spectrum for a value of temperature $Log(T) = 7.82$. In blue, we have the spectrum computed using pyatomdb. In red, the spectrum is computed using a linear combination of the individual spectrum for each element weighted by their abundance. In the bottom panel, the residuals, i.e. the error to approximate the temperature.

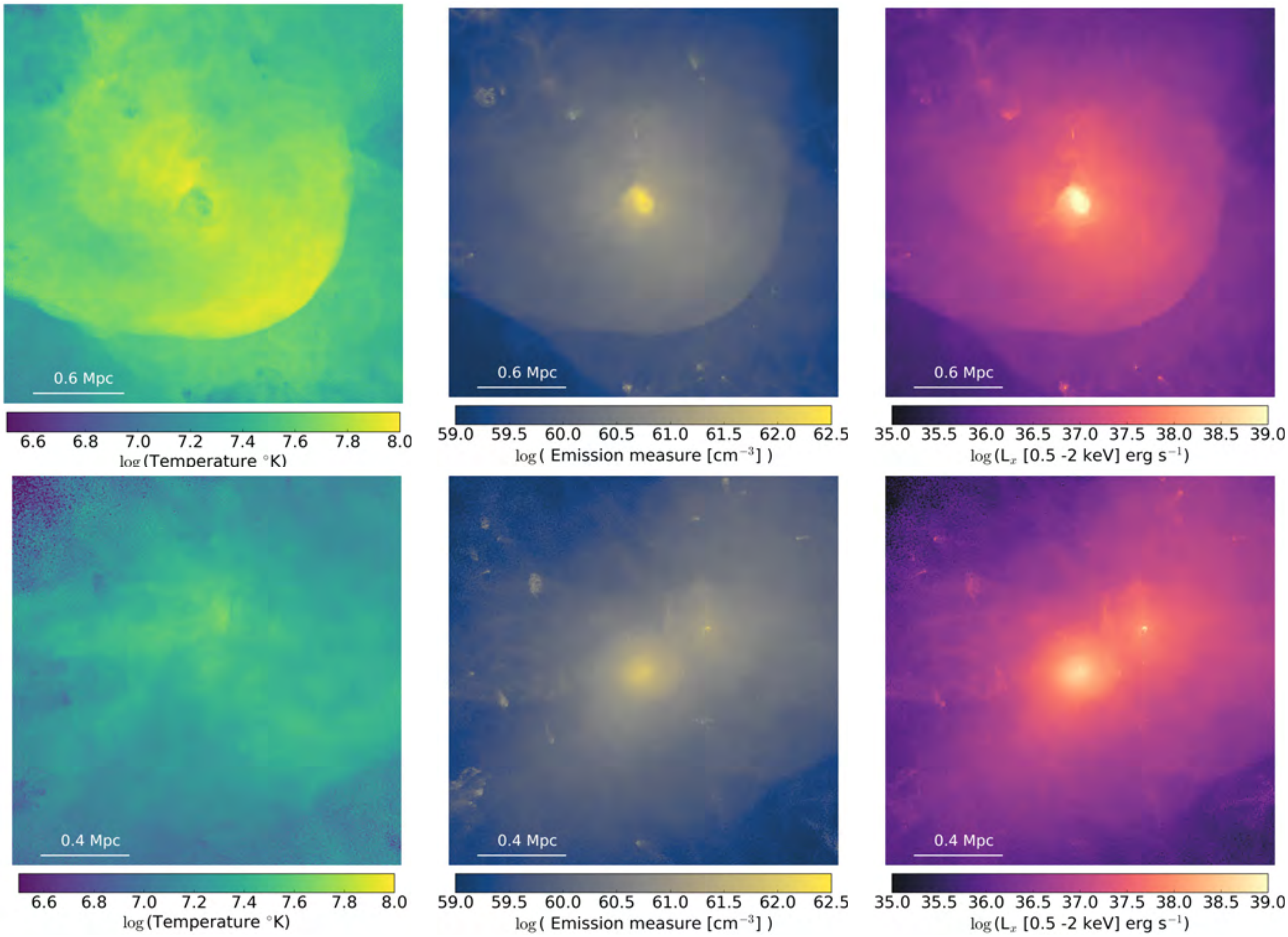

Figure 5.3.3: We present three properties for the galaxy clusters: the distribution of temperature (left), the emission measure (centre) and the X-ray luminosity (right). The first row is for a relaxed halo, while, in the second row, we present the same properties for a disturbed halo in TNG300.

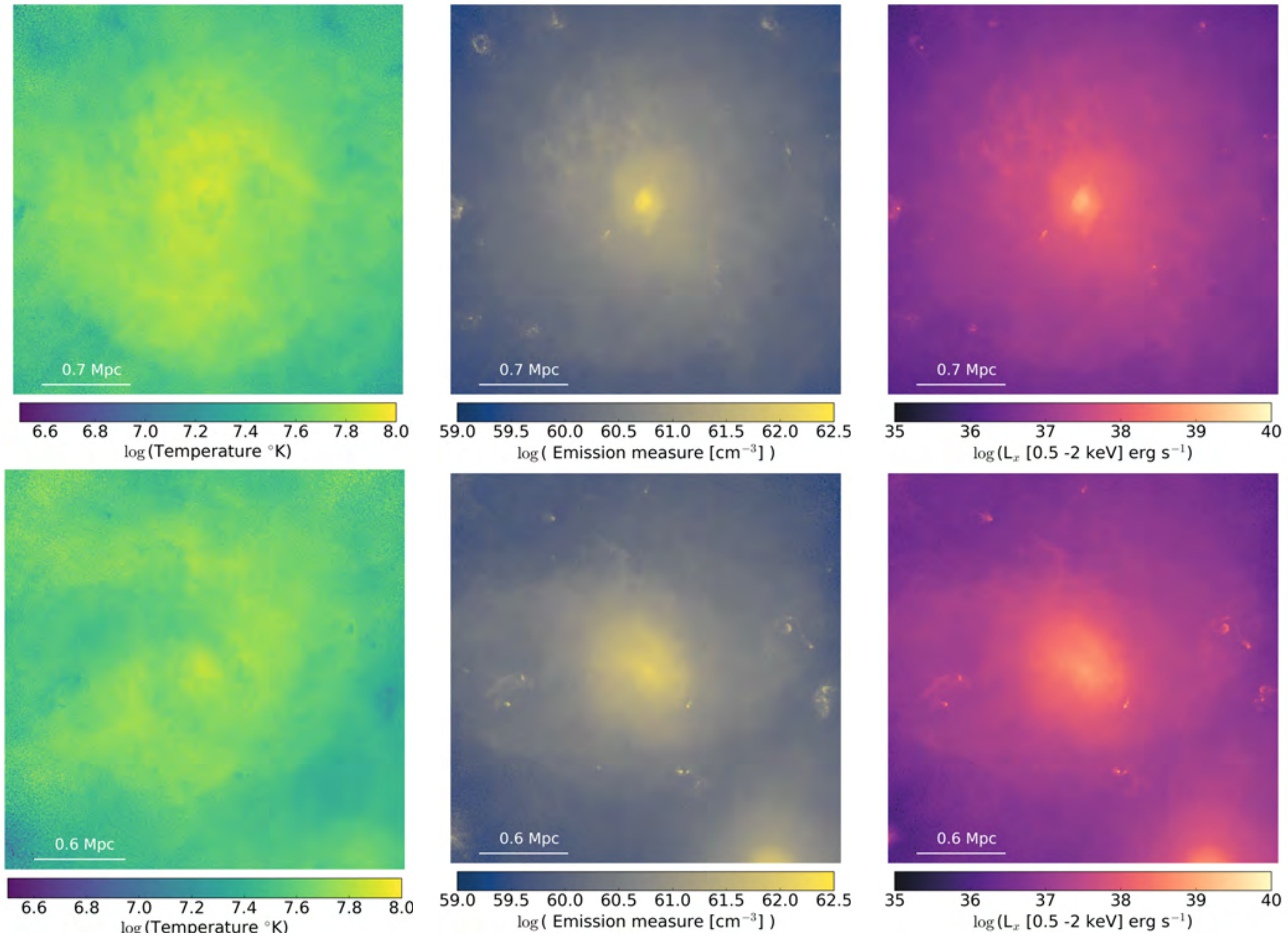

Figure 5.3.4: As in 5.3.3, a relaxed cluster in the top panel and disturbed cluster in the bottom panel from the MTNG simulation.

of these elemental spectra, weighted by their abundances, and using the set of spectra whose temperature is the closest to the gas cell's temperature.

The temperature of each gas cell is calculated using the internal energy μ and the electron abundance $(x_e = n_e/n_H)$, both characteristics provided in the simulation outputs, with the following equation:

$$T = (\gamma - 1)u/k_B \times \mu,$$

and,

$$\mu = \frac{4}{1 + 3X_H + 4X_H x_e} \times m_p,$$

where u is the internal energy of the particle, μ, is the mean molecular weight, k_B is the Boltzmann constant and m_p is the mass of the proton. Here, we used $\gamma = 5/3$, and $X_H = 0.76$ for the adiabatic index and the hydrogen mass fraction, respectively.

To illustrate the effectiveness of the spectrum generation method, we created two spectra: one at a temperature that directly matches a grid value, $\log(T) = 7.82$ (Figure 5.3.1), and another at a temperature halfway between two grid points, $\log(T) = 7.83$, which represents the maximum distance in temperature approximation (Figure 5.3.2). In each case, we compared the spectrum generated using this pipeline with the spectrum generated directly with pyatomdb. We can see that the spectrum generated with the exact temperature (Figure 5.3.1) matches that derived using pyatomdb, while the spectrum generated with the maximum possible temperature distance (Figure 5.3.2) shows minor differences in emission line intensities. Indeed, the overall shape of the spectra is very similar. The maximum error in the integrated value of the cooling function is less than 3%. The abundances used for those examples correspond to the solar abundances.

To obtain the cooling function, we also need to determine the element abundances for each gas cell. These abundances are expressed in units of solar abundances from Anders & Grevesse (1989, AG89) and are normalised to the number of hydrogen atoms in the cell. In TNG300, the abundances of the relevant elements are directly traced by the simulation, requiring only a conversion to the previously detailed scale. However, MTNG tracks only metallicity, not individual chemical elements. To estimate the abundance of each chemical element, we propose the following method: for each gas cell, metal abundances are approximated by multiplying the solar abundances from AG89 scaled by a factor given by $\theta = Z/Z_\odot$, where Z is the gas cell's metallicity, and $Z_\odot$ is the solar metallicity from AG89. The abundance of helium is assumed to remain approximately constant, with all gas cells having a helium abundance of 0.274 (Ball et al., 2016). The hydrogen abundance is then calculated by assuming that the remaining mass in the gas cell, after accounting for the traced metals and helium, is hydrogen. This method was validated with TNG300 by first computing galaxy cluster X-ray luminosities using the abundances of traced elements and then estimating them using only the metallicity available from the simulation outputs. The comparison revealed that the final luminosity values are closely aligned, with a mean error of just 1.33%.

ii) *The emission measure* (EM).- This quantity represents the number of gas particles that emit radiation in each gas cell. It is defined as $\mathrm{EM} = n_e n_H \mathrm{dV}$, where n_E and n_H are the electron and proton number densities, respectively, i.e. the EM is proportional to the square of the gas density. These ones are calculated as follows:

$$n_H = X_H \frac{\rho}{m_p}.$$

Here, ρ is the density of the gas cell, m_p is the proton mass ($m_p = 1.67 \times 10^{-25}\ g$), and X_H is the hydrogen mass fraction. The electron number density n_E is calculated as $n_E = \text{electron Abundance} \times n_H$. The electron abundance is also obtained from the simulation outputs.

iii) *Luminosity* (L_X).- Finally, to obtain the X-ray luminosity, we proceed as follows. Luminosity is the total energy emitted by an object per unit of time. As the medium is optically thin, the emitted luminosity can be computed as the product of the emission measure and the cooling function, integrated over the total volume and within a given energy range:

$$L_X = \int n_e n_H\ \Lambda(T,Z) dE dV$$

The luminosity is calculated using only gas cells that satisfy the following conditions: hot gas with temperatures $T > 10^5$ K and non-star-forming cells (i.e. $SFR = 0$). We remove star-forming and cooling gas cells because they can introduce uncertainties given the imprecise calculation of their thermal properties in the simulations. Only a few gas cells fail to meet those conditions, and they represent less than 2% of the total number of particles.

To illustrate the described pipeline to generate mock X-ray observations, Figure 5.3.3 shows two rows of images, each displaying three different properties of the galaxy clusters: temperature, emission measure, and the resulting X-ray luminosity. The first row presents a relaxed halo, while the second row represents a disturbed one. Each figure is centred on the cluster's most bound particle, and it extends to one R_{500}. The left panel shows the logarithmic temperature distribution of the ICM, with colours ranging from dark purple to yellow, which correspond to cooler and hotter regions, respectively. The relaxed halo displays a well-defined rounded temperature map dominated mainly by hot gas inside R_{500}, with the presence of cool spots corresponding to infalling small galaxies and a cool core in the very central region of the cluster, indicating a stable configuration (Fabian, 1994; McDonald et al., 2019). In contrast, the disturbed halo exhibits a much less clearly defined shape, where even the cluster core has been strongly perturbed by the major merger (Santos et al., 2008). The centre panel presents the logarithmic emission measure, which varies as the square of the ICM density, where brighter regions indicate a higher emission measure. The relaxed halo shows a strong central concentration, indicative of a settled and dense core, while the disturbed halo has a less centrally peaked emission measure, reflecting a more spread-out and less dense core. The right panel displays the resulting logarithmic X-ray luminosity, integrated within the 0.5 - 2 keV energy band, i.e. the soft X-ray emission.

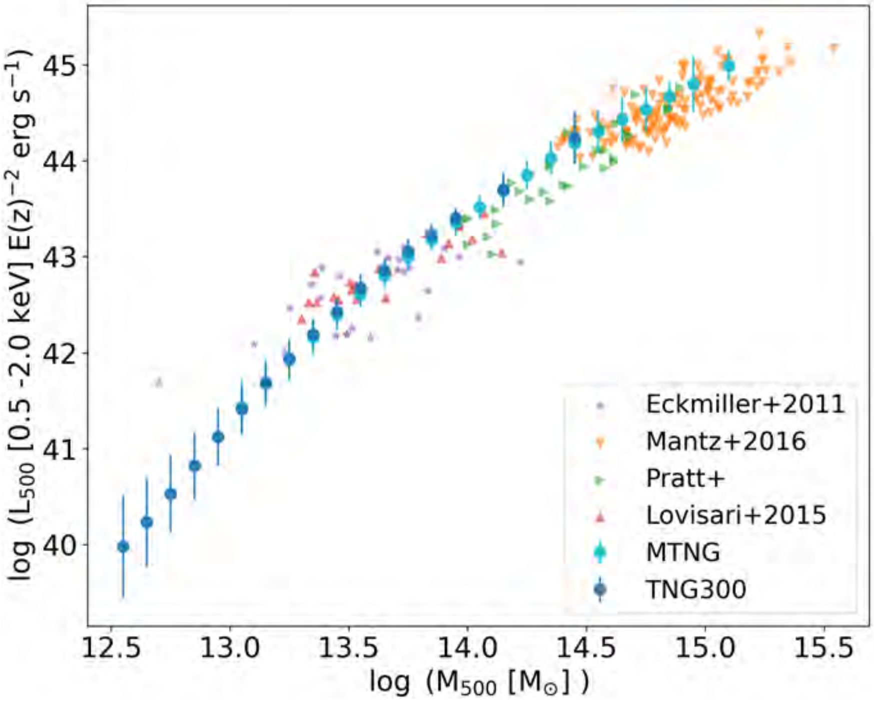

Figure 5.4.1: Scaling relation of the simulated luminosity in X-rays in the band between 0.5 - 2.0 keV as a function of M_{500} for MTNG and TNG300 compared with observational data. We can cover galaxy clusters with masses larger than $10^{14.5}$ $M_{\odot}$ with the MTNG simulations. The error bars represent the dispersion of the data measured using the geometric standard deviation.

The relaxed halo features a centrally bright region, signifying intense X-ray emission from the dense and well-defined core, which is characteristic of a stable cluster (Wang et al., 2023). In contrast, the disturbed cluster exhibits noticeable asymmetry and irregularities in the X-ray emission. These irregularities could be the result of recent or ongoing mergers, where the infall of subclusters or galaxies perturbs the ICM, leading to shock fronts, turbulence, and uneven heating of the gas.

Figure 5.3.4 presents similar plots to those presented in Figure 5.3.3, but for two halos from the MNTG simulation. As before, the top panels depict a relaxed cluster, while the bottom panels show a disturbed cluster. For the relaxed cluster, the emission measure and the X-ray emission remain strongly concentrated in the cluster core. However, the presence of a cool core is less pronounced compared to the cluster from the TNG300 simulation. This observation suggests that this cluster has probably undergone significant mergers in the early stages of their evolution, which disrupted the initial formation of a cool core (Burns et al., 2008). In the bottom row, the disturbed halo exhibits a gas that extends over a large portion of R_{500}. In the lower right corner of the X-ray emission map, a substructure can be observed falling into the main structure. We can also see smaller galaxies falling into the main cluster. These smaller galaxies display elongated shapes and tails, indicating that they are losing gas because of ram-pressure stripping.

5.4 Scaling Relations

Accurate cluster mass determination is crucial for various cosmological tests, including halo counts and clustering, baryon fraction analysis, and the determination of cluster distances (Allen et al., 2011). One common and straightforward method to estimate galaxy cluster mass is through scaling relations based on observable quantities such as the total X-ray luminosity, L_X (Lovisari et al., 2015; Pratt et al., 2009). Indeed, one of Cosmology's most significant scaling laws is the relationship between X-ray luminosity and M_{500}. For example, Mantz et al. (2010) used scaling laws to constrain the cosmological parameters such as matter density, $\omega_m = 0.23 \pm 0.04$, matter fluctuation amplitude $\sigma_8 = 0.82 \pm 0.05$, and the constant dark energy equation of state $\omega = -1.01 \pm 0.20$. Recent work by Truong et al. (2024) have presented the distribution of clusters in the L_X vs M_{500} plane for TNG300 together with the TNG-Clusters zoom-in simulation (Truong et al., 2024). However, using TNG300 and MTNG we were able to cover a large range of mass with good statistics. In this section, we construct three scaling relations for galaxy clusters using the TNG300 and MTNG simulations i) L_X - M_{500}, ii) $M_{gas,500}$ - M_{500}, and iii) k_BT - M_{500}. To construct those relations, we use the pipeline described in Section 5.3 to calculate the X-ray luminosity and mass-weighted temperature for galaxy clusters with masses $\mathrm{M}_{500} > 10^{12.5}$ $\mathrm{M}_\odot$ in TNG300 and clusters with masses $\mathrm{M}_{500} > 10^{13}$ $\mathrm{M}_\odot$ in MTNG. To enhance the visualisation of our results, we construct the L_{500} - M_{500} scaling relation by binning the clusters on a logarithmic mass scale, with each bin having a width of 0.1 dex with a minimum of 6 galaxy clusters. For each mass bin, we calculate the average luminosity using the geometric mean, as it is less sensitive to extreme values or outliers than the arithmetic mean, thereby providing a more reliable measure of central tendency (Mitchell, 2004):

$$\bar{L}_{500} = \exp\left(\frac{1}{n}\sum_{i=1}^{n} \ln \mathrm{L}_{500,i}\right)$$

Here, $\mathrm{L}_{500,i}$ denotes the luminosity of the $i-th$ cluster within a particular mass bin, and n represents the total number of clusters in that bin. Additionally, the data dispersion is calculated using the geometric standard deviation, which is defined as:

$$\sigma = \exp\sqrt{\frac{1}{n}\sum_{i=1}^{n}\left(\ln\frac{L_{500,i}}{\bar{L}_{500}}\right)}$$

In Figure 5.4.1, we present the scaling relation obtained from the TNG300 (blue) and MTNG (cyan) simulations. The data points represent mean values, while the error bars show their spread. For comparison, we also include observational data from different studies.The scaling relations obtained from the TNG300 and MTNG simulations agree well with the observed datasets, showing that these simulations can accurately reproduce the mass-luminosity relationship observed in galaxy clusters. The relatively small error bars, representing the geometrical standard deviation, are consistent with the spread in observational data. The overlap between the TNG300 and MTNG data points and the observational data indicates that the simulations capture the physical processes governing the mass-luminosity relationship in galaxy clusters across a broad range of masses, from $10^{13.5}$ to $10^{15.5}$ $\mathrm{M}_\odot$, and luminosities L_X, from 10^{42} to 10^{45} $\mathrm{erg} \cdot s^{-1}$. This ensures that the observed trend is not limited to a specific subset of clusters, but rather reflects a general characteristic of galaxy clusters.

Interestingly, we observe that the scaling relation derived from TNG300 and MTNG seems to align with a broken power law, with a pivot at $\mathrm{M}_{500} = 10^{14}$ $\mathrm{M}_\odot$. Following Brun et al. (2017), we fit the L_X versus M_{500} scaling relation using a broken power law function defined as:

$$L_X = \begin{cases} 10^{A_1}\left(\frac{\mathrm{M}_{500}}{10^{14}\mathrm{M}_\odot}\right)^{\alpha_1}, & \text{for } \mathrm{M}_{500} < 10^{14}\mathrm{M}_\odot \\ 10^{A_2}\left(\frac{\mathrm{M}_{500}}{10^{14}\mathrm{M}_\odot}\right)^{\alpha_2}, & \text{for } \mathrm{M}_{500} \geq 10^{14}\mathrm{M}_\odot \end{cases}$$

Since the fitted function must be continuous at $\mathrm{M} = 10^{14}\,\mathrm{M}_\odot$, we impose the additional constraint that $A_1 = A_2$. This allows us to fit the scaling relation with three free parameters: A_1, α_1, and α_2. Given that the MTNG and TNG300 simulations use the same physical model and yield similar X-ray luminosity values for clusters with equivalent mass, and to ensure robust statistics across the $10^{12.5} - 10^{15}$ mass range, we combined the samples from both simulations for the fitting process. The fitted parameters, along with their confidence intervals, are summarized in Table 5.4.1. Additionally, the scaling relations and the fitted model are presented in Figure 5.4.4.

For low-mass clusters ($M_{500} < 10^{14}\,\mathrm{M}_\odot$), the logarithmic slope derived from our simulations is $\alpha_1 = 2.35$. For high-mass clusters ($M_{500} \geq 10^{14}\,\mathrm{M}_\odot$) the logarithmic slope is $\alpha_2 = 1.27$. In terms of observationally derived values, Maughan (2007) found a slope of 1.96 using a sample of 115 galaxy clusters with masses between $10^{14}\mathrm{M}_\odot$ and $2\times10^{15}\mathrm{M}_\odot$. Similarly, Zhang et al. (2008), using a sample of 27 clusters with masses ranging from $2\times10^{14}\mathrm{M}_\odot$ to $10^{15}\mathrm{M}_\odot$, observed with XMM-Newton, obtained a logarithmic slope of 2.33. Furthermore, Reiprich & Bohringer (2002) reported a slope of 1.84 using a sample of 63 galaxy clusters with masses ranging from $3\times10^{13}\mathrm{M}_\odot$ to $3\times10^{15}\mathrm{M}_\odot$. Our derived values of slopes are close to the ones observationally reported.

In Figure 5.4.2, we show the scaling relation between the cluster's mass M_{500} and the gas mass $\mathrm{M}_{\mathrm{gas},500}$ in the TNG300 and MTNG simulations. This relation is generally consistent with observational data across a wide range of cluster masses. The

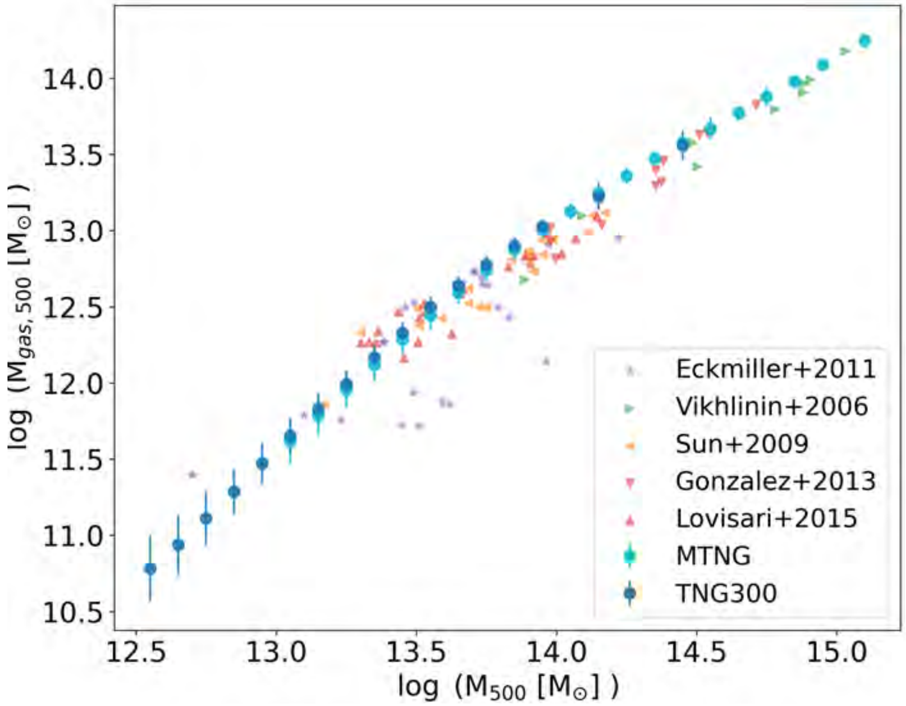

Figure 5.4.2: Scale relation of the gas mass as a function of M_{500} for MTNG and TNG300 compared with observational data. The scale relations derived observationally agree well with the values derived observationally.

spread, indicated by the bars, is narrower than that observed in the luminosity scaling relation. However, it should be noted that the data from Eckmiller et al. (2011) show a much larger dispersion than that of others observational studies and the one predicted by the simulations. We also fit this scaling relation using a broken power law, and the fitting parameters are presented in Table 5.4.1. The logarithmic slopes obtained for this scaling relation are 1.51 and 1.012 for low- and high-mass clusters, respectively. Observationally, Zhang et al. (2008) obtained a value of 0.9 for this slope, which is close to the one derived by our simulations for high-mass clusters.

Figure 5.4.3 presents the scaling relation between the mass-weighted temperature and the cluster mass M_{500}.When compared to observational data, there is a slight underprediction of the temperature of approximately 0.1 dex. We also fitted this scaling relation using a broken power law model, with the fitting parameters presented in the last row of Table 5.4.1. The logarithmic slopes found for this scaling relation are 0.6 for low-mass clusters and 0.56 for high-mass clusters. Those values are consistent with those derived observationallly: Ettori et al. (2004) and Hicks et al. (2008) obtained a value of 0.58, while Arnaud et al. (2005) derived a value of 0.56.

The coefficients obtained from fitting the mock scaling relations can also be compared to the slopes predicted by the assumption of self-similarity. Self-similarity assumes that galaxy clusters form through gravitational collapse, with their properties primarily governed by mass and redshift (Böhringer et al., 2012). Under the self-similar model, physical quantities such as temperature, luminosity, gas mass, and total mass scale with each other according to simple power laws as described below.

T-M scaling relation.- According to the virial theorem, the kinetic energy of the intracluster gas (related to its temperature) should be proportional to the gravitational potential energy of the cluster, which scales with mass. This relationship leads to the scaling relation $T \propto M^{2/3}$, resulting in a slope of approximately 0.66 in log-log space.

M_{gas}-M scaling relation.- In a self-similar model, it is assumed that the gas mass fraction (the ratio of gas mass to total

mass) is constant across clusters. This implies that the gas mass should scale directly with the total mass, leading to a linear relationship $M_{\text{gas}} \propto M$. Consequently, the slope in log-log space is expected to be 1.

L_X-M scaling relation.- To derive the slope of the L_X-M scaling relation, we start by recalling that the X-ray luminosity depends on the square of the gas density. Since X-ray emission is mainly due to the Bremsstrahlung process, it also scales with $T^{1/2}$. Assuming the gas density scales with the total mass and considering that the temperature scales as $T \propto M^{2/3}$, the X-ray luminosity is expected to scale as $L_X \propto M^{4/3}$. This results in a slope of approximately 1.33 in log-log space.

By comparing the slopes derived from the simulated scaling relations with those predicted by self-similarity theory, we find that, for high-mass clusters, the slopes align closely with the theoretical predictions. However, for low-mass clusters, the simulated slopes are steeper than those predicted by self-similarity. Non-gravitational processes, such as galactic winds, supernova feedback, cosmic rays, and active galactic nuclei (AGN), are expected to have a more significant impact on these smaller structures, increasing the intrinsic scatter in the scaling luminosity and altering the global properties of galaxy groups (Eckmiller et al., 2011). For example, Sijacki et al. (2007), McCarthy et al. (2010), and Short et al. (2010) demonstrated that incorporating AGN feedback into cosmological simulations disrupts self-similarity, lowering the luminosities. Meanwhile, Pratt et al. (2010) suggested that the observed deviations from the self-similarity of the cluster entropy profiles can be attributed to variations in the gas content of the clusters as a function of mass and radius. They proposed a mechanism in which the heating from AGN, combined with mixing from mergers, causes a redistribution of gas. This leads to the observed decrease of luminosity in low-mass systems. Another plausible mechanism for preheating is early star formation, which increases the entropy of the intergalactic medium before cluster formation, which along with the cooling and condensation of low-entropy material, increases the entropy of the remaining gas, (Borgani et al., 2004; Böhringer & Werner, 2010; Younger & Bryan, 2007).

In Figure 5.4.4, we present the results of the fitting of L_X -M_{500} (top left panel), $M_{gas,500}$ -M_{500} (in the top right panel) and the T_{500} - M_{500} (bottom panel) scaling relations derived from the combined TNG300 and MTNG sample. Each subplot displays the scaling relation as black dots, with error bars indicating the data scatter. The broken power-law fitting coefficients are shown in the bottom right corner of each subplot, and the fitted model is overlaid in red. In general, the model provides a good fit to the scaling relation, with the exception of a small region around $10^{14} M_\odot$ in the L_X -M_{200} scaling relation.

Table 5.4.1: Fitting coefficients of scaling relations using a broken power law with fix pivot in 10^{14} M$_\odot$.

Scaling Relation	α_1	α_2	A_1
L$_X$ - M$_{500}$	2.38 ± 0.08	1.27± 0.11	43.49± 0.07
M$_{\text{gas},500}$ - M$_{500}$	1.59 ± 0.02	1.01± 0.03	13.12± 0.02
k$_B$T - M$_{500}$	0.61 ± 0.02	0.57± 0.03	0.22± 0.02

In summary, this section demonstrates that we can successfully reproduce the observed scaling relations for galaxy clusters using the TNG300 and MTNG simulations. Specifically, the simulations closely match the scaling relations L$_X$ - M$_{500}$ and M$_{\text{gas},500}$ - M$_{500}$. However, the k_BT - M$_{500}$ relation slightly underpredicts the scaling relation derived observationally. The dependence of the X-ray luminosity on the square of the gas density and the square root of the gas temperature means that the emission is highly sensitive to the physical models implemented in the simulations. Variations in gas properties, such as cluster mergers or intense cooling, introduce variability in X-ray emission intensity, as evidenced by the increased scatter in Figure 5.4.1 compared to the scaling relation between M$_{\text{gas},500}$ and M$_{500}$. The agreement between the simulated and observed data suggests that the simulations incorporate key physical mechanisms affecting X-ray luminosity, including gas density, temperature, and cluster dynamics. Additionally, the MTNG simulation recovers the predicted slopes for high-mass clusters (M$_{500} > 10^{14}$ M$_\odot$) quite well, particularly for the luminosity and gas-mass scaling relations, and remains close in the case of temperature.

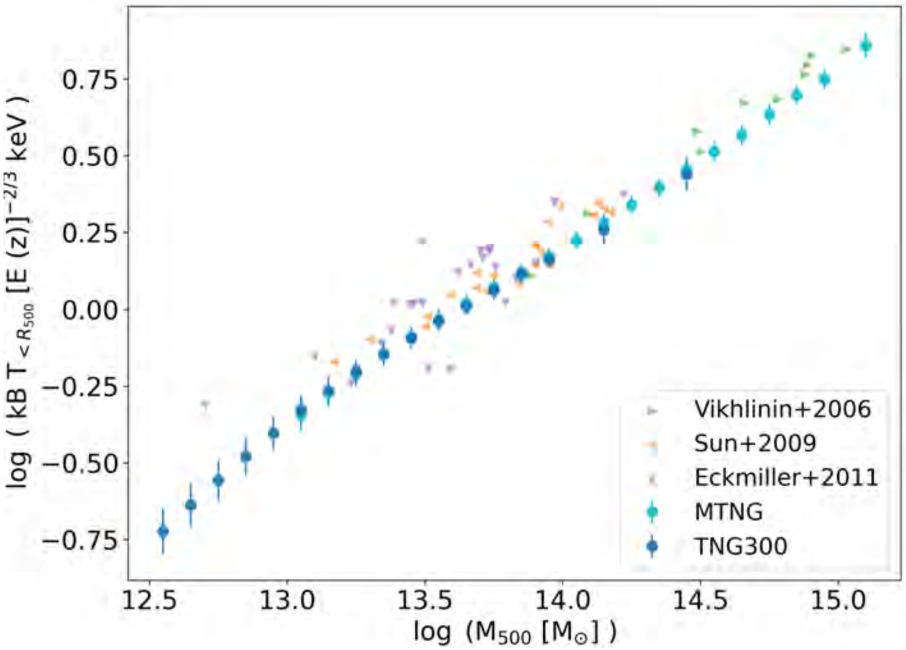

Figure 5.4.3: Scale relation of the gas temperature as a function of M_{500} for MTNG and TNG300 compared with observational data. Overall, the predicted temperature values show good agreement with observational data, though simulations tend to slightly underestimate the temperatures.

5.5 Separation between relaxed and disturbed clusters.

In the literature, several parameters derived from X-ray emission maps have been used to classify galaxy clusters as relaxed or disturbed. These parameters are typically based on projected X-ray images that focus on the central regions of clusters, as they are evaluated within R_{500}. However, during the early stages of mergers, the dynamical state of a cluster can be influenced by interactions in the outskirts, while the central region remaining largely unaffected. In this section we classify galaxy clusters as relaxed or disturbed using the criterion proposed by Aldás et al. (2024) (hereafter A24). Following this classification, we create 2D X-ray emission projections along the z-axis and compute commonly used proxies for determining the dynamical state of galaxy clusters, including the concentration index, centroid shift, power ratio, and kinetic-to-thermal energy ratio. We then compare their distributions and correlations in the simulated emission maps.

The criterion proposed in A24 to select relaxed and disturbed clusters uses the 3D positions of the gas cells to calculate the offset between the Brightest Cluster Galaxy (BCG) and the centre of mass of the gas from all particles within the FOF D_{BCG-CM}. Galaxy clusters are classified as disturbed if their D_{BCG-CM} exceeds $0.4 \times$ R200 (Zenteno et al., 2020, see). This approach provides a more global evaluation of the dynamical state of a cluster compared to parameters derived solely from X-ray emission within R_{500}. We identified 2,548 galaxy clusters with $M_{500} > 10^{12.5} M_{\odot}$ in TNG300 and 55,886 galaxy clusters with $M_{500} > 10^{13} M_{\odot}$ in MTNG, resulting in a final sample of 58,434 clusters. Within this sample, 2,658 were classified as disturbed. To create a comparable sample of relaxed clusters, we selected an equal number of clusters with the lowest D_{BCG-CM} values. This also allows us to highlight any difference between the dynamical proxies that may arise between both subsamples. Figure 5.5.1 shows the histogram of the D_{BCG-CM} distribution for the entire sample, with the selected relaxed and disturbed clusters highlighted in blue and red, respectively.

The details of each studied parameter are provided below:

1. *Concentration index (CI)*.- The concentration index is the ratio of the integrated luminosities measured at two different

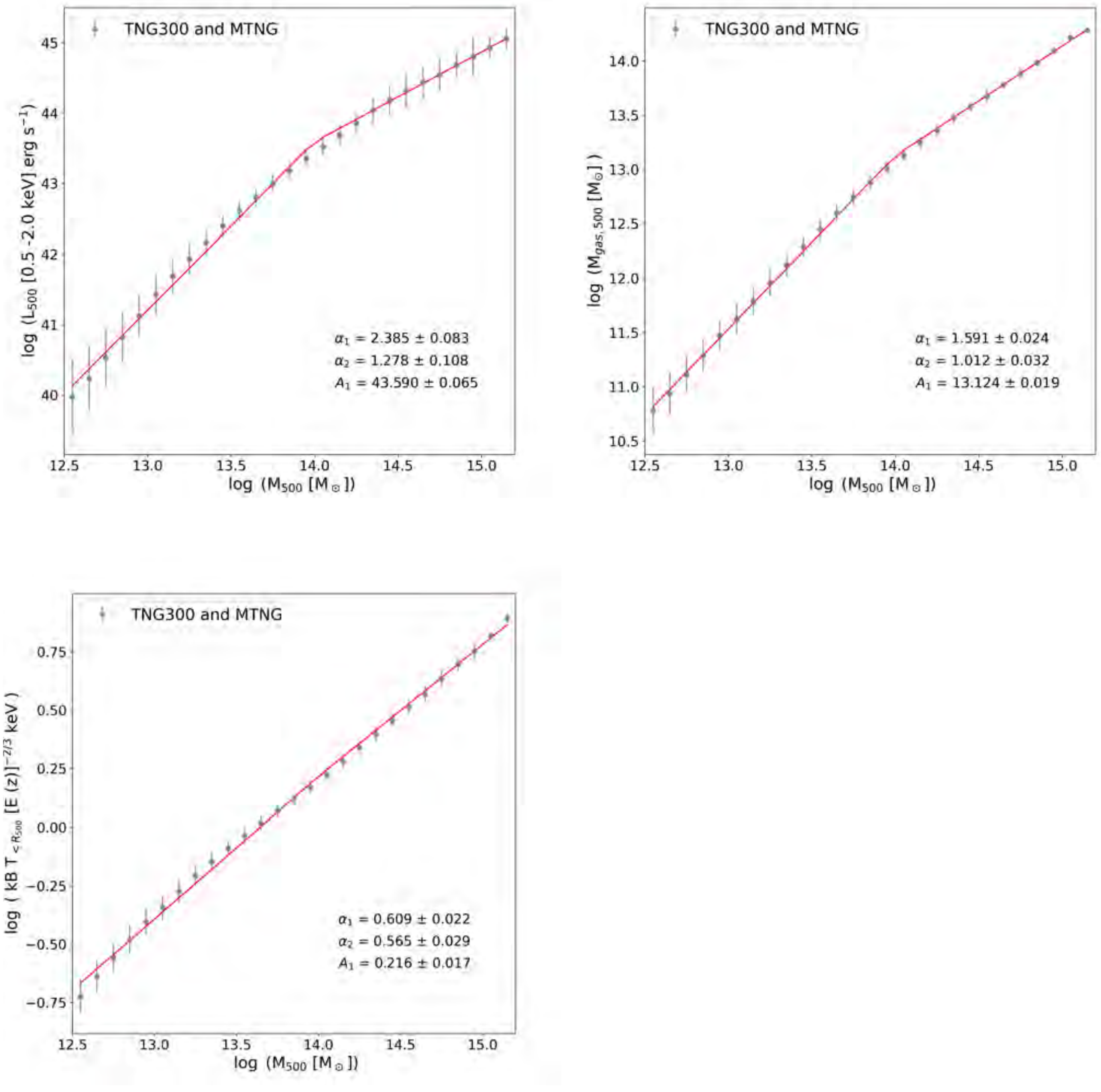

Figure 5.4.4: We present the scaling relations for the join sample of TNG300 and MTNG for the L_X -M_{500} (top left panel), $M_{gas,500}$ -M_{500} (in the top right panel), and the T_{500}- M_{500} (bottom panel) scaling relations. In each figure, we also have the bars representing the scatter of the data and in red the fitted model.

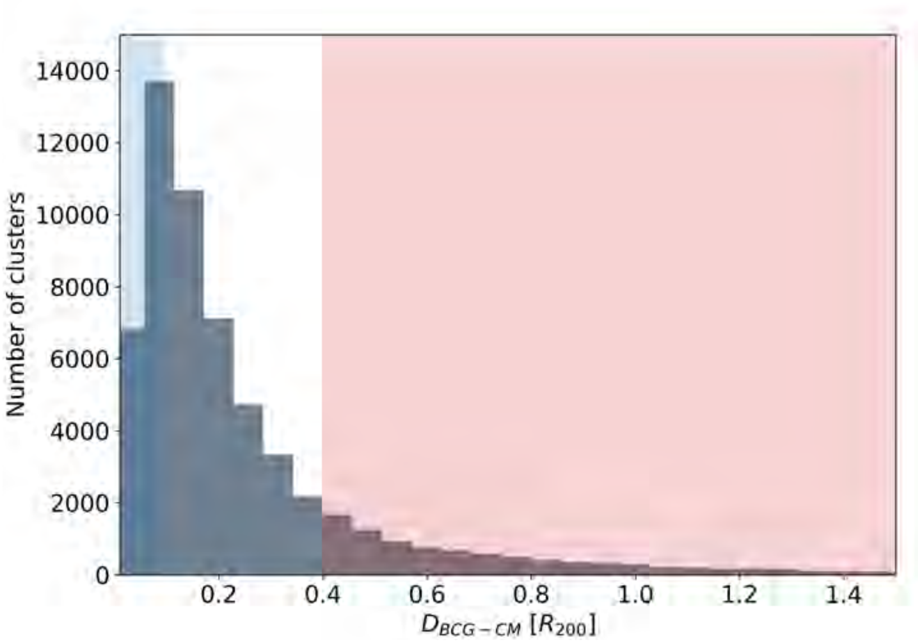

Figure 5.5.1: Histogram of the offset between the position of the BCG and the position of the centre of mass of the gas measured in units of R_{200}. The selected clusters are presented in the blue shadow region, and the disturbed clusters are presented in the red shadow region.

appertures (Santos et al., 2008):

$$c = \frac{S_{core}}{S_{R_{500}}} = \frac{\sum_{R<R_{core}} f(x_i, y_i)}{\sum_{R<R_{500}} f(x_i, y_i)} \tag{5.5.1}$$

Here, $R_{core} \sim 0.1 \times R_{500}$, and $f(x_i, y_i)$ is the luminosity of the $i-th$ pixel located at a position (x_i, y_i). Relaxed clusters are expected to have more luminous cores compared with disturbed ones (Fabian, 1994), causing their concentration index to approach 1. In contrast, for merging clusters with disturbed structures, the concentration index would tend to have significantly lower values.

2. *The centroid shift* (ω).- The centroid shift is defined as the standard deviation of the offset between the X-ray peak and the X-ray emission centroid (Poole et al., 2006). The centroid positions are calculated using multiple circular apertures, ranging from R_{200} down to $0.15 \times R_{200}$, with a decreasing step size of $0.05 \times R_{200}$. The centroid shift, ω, is then given by:

$$\omega = \left[\frac{1}{n-1}\sum_{i}^{n}(\Delta - \langle\Delta\rangle)^2\right]^{1/2}\frac{1}{R_{500}} \tag{5.5.2}$$

Here, $\Delta = \sqrt{(x_{MB} - \bar{x})^2 + (y_{MB} - \bar{y})^2}$, where x_{MB} and y_{MB} are the positions of the most bound particles in the x and y directions, respectively. $\bar{x}$ and $\bar{y}$ are the coordinates of the centroid, and $\langle\Delta\rangle$ represents the mean value of Δ. To compute the centroid of the X-ray emission map, we first compute the moments of the image as:

$$M_{kl} = \sum_i \sum_j x_i^k y_j^l L_X(x_i, y_j) \tag{5.5.3}$$

with k, and l the order of the moment. The centroid is defined as:

$$\bar{x} = \frac{M_{10}}{M_{00}} \tag{5.5.4}$$

$$\bar{y} = \frac{M_{01}}{M_{00}} \tag{5.5.5}$$

Clusters undergoing merging processes often exhibit significantly larger values of ω, while in relaxed clusters ω tends to zero (Poole et al., 2006).

3. *Power ratio* ($P3/P0$).- In merging clusters, usually, we can see the presence of substructures. Those can be detected using the power ratio between P_3 and P_0, which are the monopole and octupole moments corresponding to the decomposition of the X-ray surface brightness distribution into a series of multiples (Bauer et al., 2005; Buote & Tsai, 1995), P_m is calculated as:

$$\begin{aligned} P_0 &= [a_0 In(R_{ap})]^2, \\ P_m &= \frac{1}{2m^2} R_{ap}^2 (a_m^2 + b_m^2) \end{aligned}$$

The values of a_m, and b_m are given by:

$$\begin{aligned} a_m &= \int_{r \leq R_{ap}} L_X(x_i, y_i)(r)^m cos(m\phi) dx_i dy_i \\ b_m &= \int_{r \leq R_{ap}} L_X(x_i, y_i)(r)^m sin(m\phi) dx_i dy_i \end{aligned}$$

Here, r is the distance of the pixel located at (x_i, y_i) with respect to the cluster centre and ϕ is the position angle of the pixel (x_i, y_i) defined as $\phi = \arctan(\frac{y_i}{x_i})$. Relaxed clusters are expected to have lower values of $P3/P0$ compared to disturbed ones.

4. *Energy Ratio* (K/T).- Finally, although this proxy is not derived from the emission map, the energy ratio is among the most widely used indicators for determining the dynamical state of galaxy clusters in simulations. It is defined as the ratio of kinetic energy to thermal energy (K/T), with both energies measured for gas cells within the critical radius R_{500} (Barnes et al., 2017).

$$K/T = \frac{E_{kinetic}}{E_{thermal}} \tag{5.5.6}$$

When a cluster undergoes a merger, the gas cells have substantial kinetic energy that is transformed into thermal energy while the cluster relaxes (Kunz et al., 2011). As such, relaxed clusters are expected to have lower values relative to their disturbed counterparts.

The corner plot shown in Figure 5.5.2, illustrates the relationships between the most common indicators to measure the dynamical state of a galaxy cluster. Here, red and blue contours represent disturbed and relaxed clusters, respectively. The figure includes histograms along the diagonal positions, depicting the distribution of each variable, and contour plots in the off-diagonal, including the Spearman rank order, which measures the correlations between variable pairs. Values close to 1 and -1 represent a strong correlation and a strong anticorrelation, respectively. Histograms reveal that the distributions differ significantly between relaxed and disturbed clusters except for the ($P3/P0$) parameter, where both samples have very similar distributions. As expected, relaxed clusters tend to have higher CI values, and lower (K/T) and ω values compared to disturbed clusters. The trends found in this section are consistent with the findings of studies such as those by Pratt et al. (2009) and Maughan (2013), which have shown that relaxed clusters tend to have more concentrated and luminous cores compared to disturbed clusters, likely due to the more settled gas distribution in relaxed clusters.

The distributions of the proxies CI, K/T and ω differ significantly between relaxed and disturbed clusters. For each of these parameters, the distributions for relaxed clusters peak at different values compared to those for disturbed clusters, indicating that the maxima of these distributions vary depending on the dynamical state of the cluster. However, these distributions are not entirely distinct, leading to overlapping regions where a cluster could be classified as relaxed or disturbed. This result can be due to the criteria proposed by A24, which reflects a global state of galaxy clusters because it considers all particles in the FOF up to much further distances ($\geq R_{200}$ from the main BCG) in disturbed clusters. For example, in the disturbed cluster presented in Figure 5.3.4, there is a secondary substructure that interacts with the main cluster in the lower right corner, and thus the cluster is classified as disturbed in A24. However, this substructure is not close enough to significantly affect X-ray emission within R_{500}.

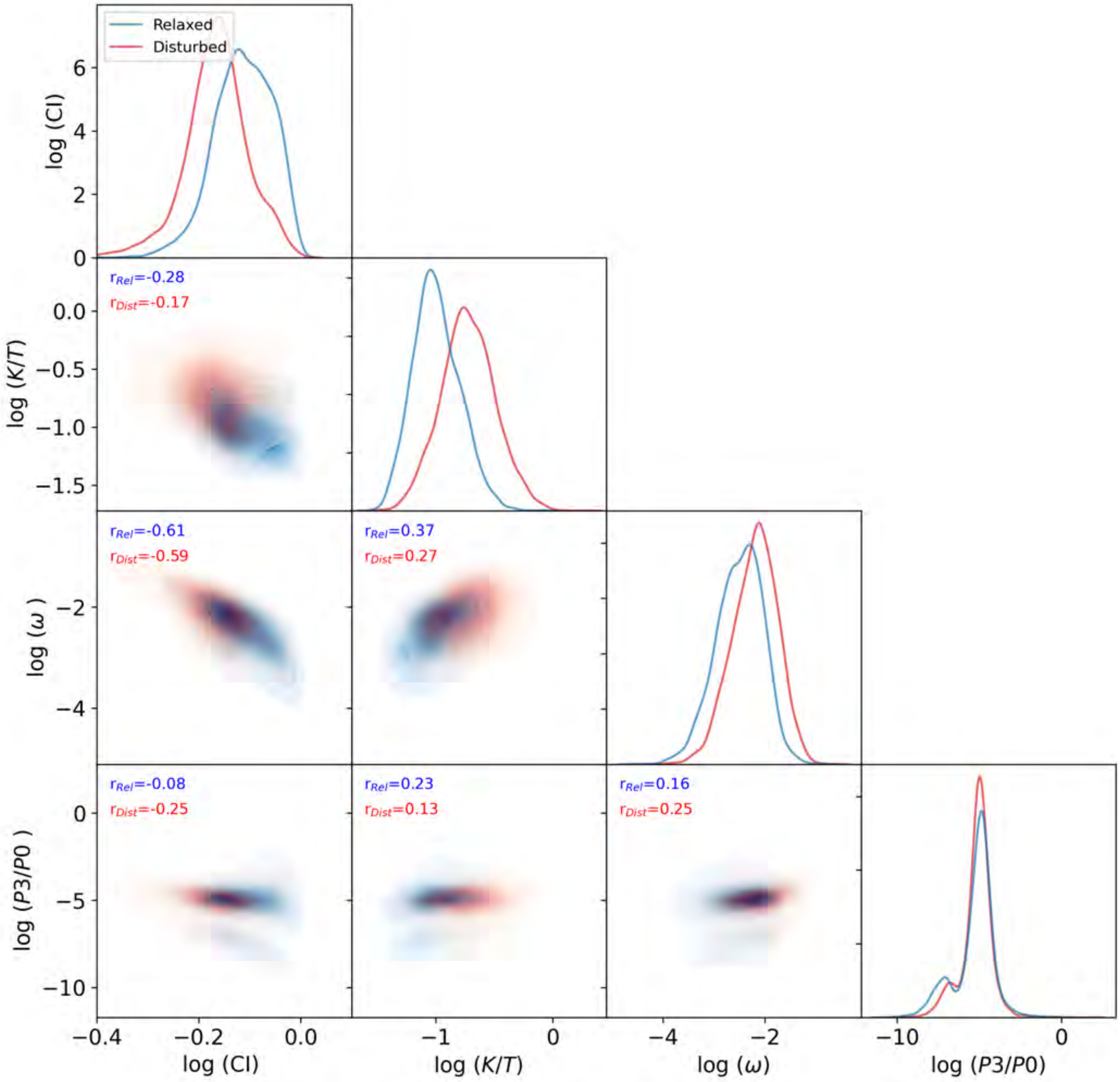

Figure 5.5.2: Indicators used in the literature to separate between relaxed and disturbed clusters.

With respect to the off-diagonal distributions, we can see that relaxed clusters generally exhibit more concentrated and elongated distributions, indicating stronger and more consistent correlations between the variables. In contrast, disturbed clusters (red contours) exhibit more dispersion and weaker correlations. The more dispersed and less elongated shapes of the red contours indicate that the relationships between proxies in disturbed clusters are less strong. This dispersion suggests that disturbed clusters have more unstable conditions, leading to less consistent relationships between the variables. Finally, Figure 5.5.2 suggests that the parameters with the highest linear correlation are the CI and ω, which also have a small scatter.

5.6 Scaling relations between relaxed and disturbed clusters.

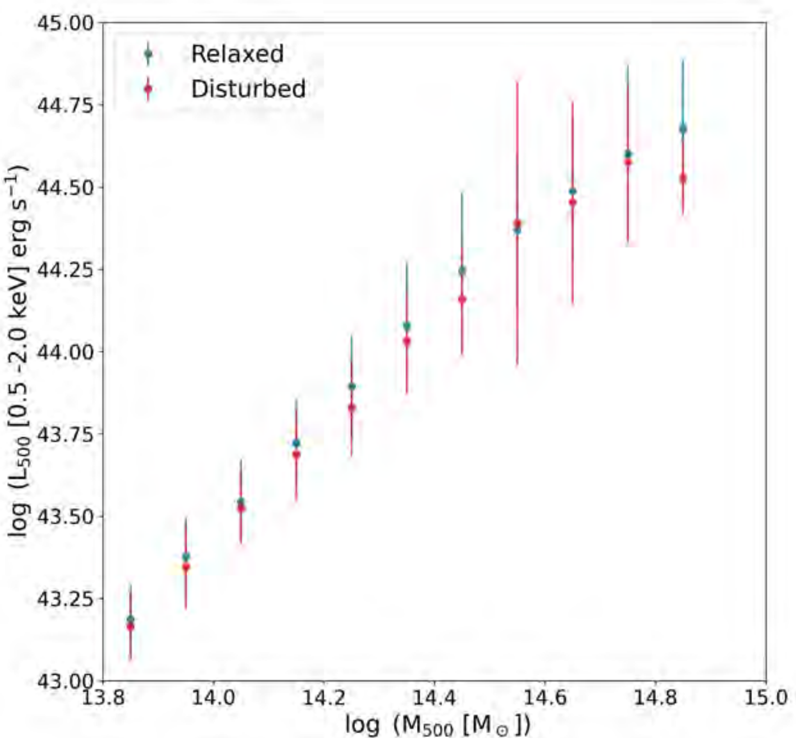

Figure 5.6.1: X-rays luminosity inside R_{500} as a function of M$_{500}$ for relaxed (blue) and disturbed (red) galaxy clusters. We can observe that the relaxed clusters exhibit a slightly higher luminosity at a given mass. However, the differences are below the data dispersion.

The final section of this Chapter focuses on studying the dependence of the scaling relations on the dynamical state of galaxy clusters. In Figure 5.6.1, we present the scaling relations L$_{500}$ - M$_{500}$ for relaxed and disturbed clusters. At lower masses, the luminosities of relaxed and disturbed clusters are less than one sigma of difference, with overlapping data dispersion. At higher masses, the relaxed clusters (blue points) seem to have slightly higher luminosities than the disturbed clusters (red points). However, the difference is subtle and within the range of one σ dispersion. We also performed the ANCOVA statiscal test in order to see if the difference in the X-ray luminosity between relaxed and disturbed galaxy clusters is significative but it concluded that this difference is not signifive.

Our result cannot correctly reproduce the differences in the X-ray luminosity-to-mass scaling relation as reported by Mantz et al. (2016b), who highlighted that the dynamical state of the clusters impacts their scaling relations, with relaxed clusters generally showing tighter correlations and higher normalisation in the $L_X - M$ plane. Also, Lovisari et al. (2020) using 120 galaxy clusters observed with XMM-Newton found that at a given mass, relaxed clusters have a luminosity 30% higher and

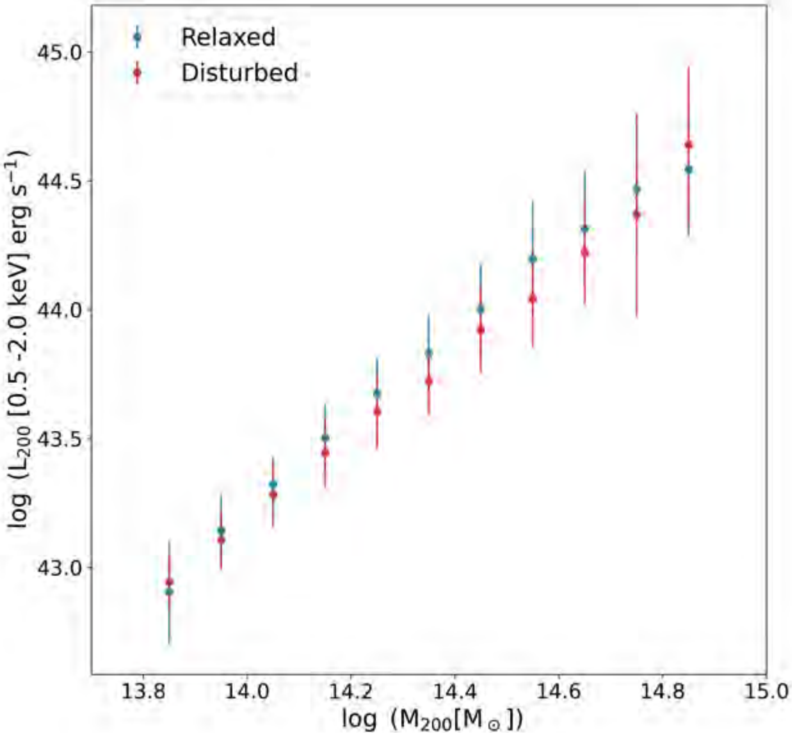

Figure 5.6.2: X-rays luminosity inside R_{200} as a function of the mass M_{200} for relaxed (blue) and disturbed (red) galaxy clusters. In this case, we can observe a significant difference than in the case of Figure 5.6.1 between the estimated luminosity of relaxed and disturbed clusters' luminosity at a given mass.

a lower scatter than disturbed clusters. However, the slopes between these samples are identical. The inability of our simulations to replicate the separation between relaxed and disturbed clusters in the luminosity-to-mass scaling relation observed by Mantz et al. (2016b) is likely due to the different criteria used to select disturbed clusters. The selection method by A24 tends to prioritise clusters at an earlier stage of interaction, whereas Mantz's method identifies clusters at a more advanced evolutionary stage. Consequently, it is probable that the disturbed clusters in Mantz et al. (2016b) have already experienced significant perturbations within R_{500}.

In Figure 5.6.2, we now present the scaling relation for relaxed and disturbed clusters but integrated inside R_{200} as a function of the mass M_{200}. At a given total mass, relaxed clusters have higher luminosities compared to disturbed clusters. We can see that this difference is more noticeable for the high-mass clusters than for the low-mass ones. In fact, the ANCOVA statistical test concluded that the differences in X-ray luminosity between relaxed and disturbed clusters inside R_{200} are significant with a p-value of 0.001. Although outside R_{500} the X-ray surface brightness decreases quickly, making it difficult to study observationally, this result highlights the importance of studying the properties of galaxy clusters at distances greater than R_{500}, especially when studying disturbed galaxy clusters.

5.7 Conclusions and Discussion

This Chapter presents an optimised pipeline to generate X-ray mocks for galaxy clusters in the TNG300 and MTNG simulations. This pipeline allows us to compute the luminosity distribution of the galaxy clusters using the "APEC" code developed to estimate the emission spectrum. This code can process large volumes of data in a relatively short time. The combination of TNG300 and MTNG allowed us to compute the $L_{X,500}$ -M_{500} scaling relation in a wide mass range, from $10^{12.5}$ M_{500} to $10^{15.2}$ M_{500} and to have good statistics in the whole mass range. We validate the pipeline used to create the X-ray mocks by comparing the simulated scaling relation with the observational data from multiple observations, especially in the range of high-mass clusters, $M_{500} > 10^{14} M_{\odot}$ (Eckmiller et al., 2011; Mantz et al., 2016a; Lovisari et al., 2015). The low-mass cluster samples are limited. We hope that the new X-ray surveys, such as eROSITAS, can cover this mass range, helping us to understand the physical processes in the presence of a broken power law.

The comparison of theoretical logarithmic slopes with those derived from the simulations reveals that, for high-mass clusters, the slopes align well with self-similarity predictions. In contrast, for low-mass clusters, the slopes are steeper than those expected from self-similarity. This difference can be attributed to non-gravitational effects, such as AGN and supernova feedback, which have a more pronounced impact on low-mass structures, such as galaxy groups and small clusters (Eckmiller et al., 2011).

We separated our galaxy cluster sample into relaxed and disturbed systems, following A24, to study the most commonly used proxies used to estimate the dynamic state of the clusters. Our results reveal significant differences in the distributions of dynamical state indicators between relaxed and disturbed galaxy clusters. Relaxed clusters show more consistent and predictable relationships between parameters like energy ratio and ω, while disturbed clusters exhibit greater variability and weaker correlations.

In the $L_{X,500}$ - M_{500} relation, we observed that relaxed clusters exhibit slightly higher luminosities compared to disturbed clusters, with a variation that falls within the data scatter. However, we identify a more significant difference in the scaling relation between luminosity $L_{X,200}$ and M_{200}. The reason why simulations are unable to accurately reproduce the observational differences found in the L_X - M_{500} scaling relation for relaxed and disturbed clusters reported by Mantz et al. (2016b) and Lovisari et al. (2020) should be analysed in more detail. This analysis is necessary to determine whether the discrepancies are due to issues with the model used to generate the X-ray mocks, the simulation model itself, or the selection criteria used to classify clusters as relaxed or disturbed.

Chapter 6

Concluding Remarks

This thesis addresses the impact of the dynamical state of galaxy clusters on their satellite population, focussing on the differences between relaxed and disturbed clusters. In this analysis, we used a combination of observational data obtained using Dark Energy Camera (DeCAM) and two full-physics cosmological simulations, the IllustrisTNG and MilleniumTNG, to explore the differences in the physical properties of galaxy populations in these two different clusters' dynamical states. We focus on different galaxy properties, including the red sequence morphology, colour distribution, quenched fraction, and gas availability. We also generated and analysed mock images of the X-ray emission for our simulated galaxy clusters to study the impact of the dynamical state in their scaling relations.

In chapter 3 of this thesis, we examined a sample of 84 galaxy clusters identified by the South Pole Telescope and observed with the DECam during two surveys. Of these, 65 clusters were observed during the Dark Energy Survey (DES), as listed in Table 3.7.2, covering the redshift range $0.1 < z < 0.65$. The remaining 19 clusters were part of the DeROSITAS survey, an optical survey using DECam that planned to collect optical data for the same sky region that eROSITA is mapping in X-rays. The clusters observed in DeROSITAS, listed in Table 3.7.1, have longer exposure times, as they span a redshift range between $0.11 \leq z \leq 0.88$. We analysed the galaxy clusters' Red Sequence (RS) using colour-magnitude diagrams (CMDs). The RS represents a population of predominantly red galaxies, typically elliptical or lenticular in morphology, that have little to nothing of ongoing star formation. These galaxies appear red because of the dominance of older, cooler stars (like red giants) and the absence of younger, blue stellar populations. To investigate the impact of cluster mergers on the properties of their galaxy member as a function of cosmic time, the sample of galaxy clusters was divided into low ($0.1 \leq z < 0.55$) and high redshift $0.55 \leq z \leq 0.9$ bins. Additionally, we subdivide our cluster samples according to their dynamic state. As a result, we have four subgroups of clusters: disturbed and relaxed clusters at both low and high redshifts. The dynamical states of these galaxy clusters were previously estimated by Zenteno et al. (2020). The classification was carried out using four proxies: the offset between the position of the BCG and the SZ centroid (D_{BCG-SZ}), the core temperature, the morphological parameter, A_{Phot}, which measures the asymmetry of the X-ray emission, and the offset between the BCG and the peak of the X-ray emission.

We constructed background-subtracted CMDs for each galaxy cluster to isolate only the galaxies gravitationally bound to the cluster. After that, we applied stellar population-synthesis models, using exponential starburst decay and a Chabrier Initial Mass Function (IMF), to calculate the expected slope of the red sequence (RS) at the cluster's redshift and subtract it from the observed slope, flattening the RS's colour slope to zero (Bruzual & Charlot, 2003; Song et al., 2012; Zenteno et al., 2016). Then, we stacked the cluster CMDs in each subgroup to obtain the average RS for each studied subgroup. The results show that disturbed clusters at high redshift exhibit a larger scatter in the RS, which is associated with a more mixed galaxy population. In contrast, the CMDs of relaxed and disturbed clusters are similar at lower redshift. After that, we explored the relationship between the dynamical state of clusters and the colour distribution of their galaxies using a colour density diagram. At $0.55 \leq z \leq 0.9$, disturbed clusters exhibit a higher fraction of blue galaxies than relaxed clusters. In contrast, at $z < 0.55$, the RS follows very similar trends in disturbed and relaxed clusters, with no significant differences between these subsamples. This shows that, at least for high redshift clusters, the galaxy population of disturbed clusters is bluer and likely less quenched than that in relaxed clusters. This observation can be explained by two possible scenarios: an enhancement in the star formation rate in merging clusters or the possibility that disturbed clusters correspond to a less-evolved state than relaxed clusters.

In chapter 4, we study how the physical properties, such as colour, star formation rate, and gas content of galaxy populations in groups and clusters, are affected by major mergers. To do so, we used a full-physics cosmological simulation from the Illustris-TNG project, specifically the TNG100 simulation, which provides us with a good sample of galaxy groups and clusters with masses $M_{200} > 10^{13}$ M$_\odot$ and a good mass resolution, leading us to resolve satellite galaxies of $M_* = 10^9$ M$_\odot$ with around 800 stellar particles. The sample was divided into relaxed and disturbed clusters based on the offset between the BCG and the centre of mass of the gas distribution, using a threshold of $0.4 \times R_{200}$ to define disturbed clusters. This produced 153 disturbed groups and clusters in six snapshots between $0.1 < z < 1$. For a fair comparison, an equal number of the most relaxed clusters were selected, using halos with the smallest offset between the BCG's position and the gas distribution's centre of mass. Galaxies were further classified into red and blue populations using a colour threshold derived from a double Gaussian fit to the galaxy colour distribution and into quenched and star-forming populations based on the fitted main sequence in the star formation rate versus stellar mass diagram (Donnari et al., 2019). The results of this analysis reveal that there is a larger fraction of red galaxies in relaxed clusters compared to disturbed ones. This trend is observed outside and inside R_{200} but is stronger in the outskirts of the galaxy groups and clusters where the environmental effects are less intense than inside R_{200}.

As shown in chapter 3, and also by Zenteno et al. (2020), the differences between relaxed and disturbed clusters are more relevant for $z \sim 0.5$. For this reason, we also subdivide the sample into low $(0.1 < 0.5)$ and high $(0.5 \leq < z \leq 1)$ redshift bins. We showed that quenched fractions decrease with increasing distance from the cluster centre in both relaxed and disturbed clusters, with relaxed clusters consistently exhibiting higher quenched fractions than disturbed ones. This trend is more pronounced at low redshifts, indicating that environmental quenching processes are more effective or have had more time to act at these redshifts. This is supported by the fact that galaxies bound to disturbed groups and clusters consistently have more gas in all the different phases defined by Torrey et al. (2012), hot, diffuse, and condensed gas, compared to those in relaxed clusters; showing a larger difference at high redshift bins. Finally, we also found that during the initial phases of cluster mergers, the specific star formation rate (sSFR) rises during a short period, likely because of gas compression resulting from the shocks generated during the cluster merging process. As the galaxy cluster becomes more relaxed, star formation slows down, and galaxies become less active in forming new stars.

X-ray emission maps are essential for studying the dynamical state of galaxy clusters, as they effectively trace the properties of the intra-cluster medium (ICM) highly affected by cluster mergers. For this reason, chapter 5 of this thesis is dedicated to generating and analysing X-ray emission mocks for galaxy groups and clusters using the Illustris TNG300 and Millennium TNG-740 cosmological simulations. The pipeline to generate the X-ray mocks involves calculating the cooling function, representing the rate at which the ICM radiates energy. To model the cooling function, we used the APEC code to generate the emission spectrum. This model depends on the temperature and chemical abundances of each gas cell. In order to speed up the calculation of the emission spectra, we used pre-computed individual spectra for each traced element in a predefined temperature grid. Then, the final spectrum is computed by a linear combination of the elemental spectra weighted by their element abundances. After that, we calculated the emission measure, which is proportional to the square of the gas density and proportional to the square root of the gas cell temperature. Finally, the X-ray luminosity was obtained by multiplying the emission measure by the cooling function and integrating it over the entire cluster volume. This method enables the computationally efficient generation of X-ray emission maps for simulated galaxy groups and clusters, which can process a full simulation snapshot in around 4 hours, using parallelisation across 15 cores. To validate this pipeline, we used three main scaling relations, typically used in observational studies: L_X–M_{500}, $M_{\rm gas}$–M_{500}, and temperature–M_{500}. The results show good agreement with the observational data in a mass range between $10^{12.5}$ to $10^{15.5} M_\odot$. The scaling relations are fit using a broken power law, revealing that the slope of the relation changes around $M_{500} = 10^{14} M_\odot$. For high-mass clusters, the slopes are consistent with self-similarity predictions. In contrast, low-mass clusters exhibit steeper slopes, likely due to non-gravitational processes such as feedback from supernovae and active galactic nuclei (AGN). The results obtained from the TNG300 and Millennium TNG simulations demonstrate that the simulations can accurately reproduce the scaling relations observed in galaxy clusters, particularly in the high-mass range. The consistency between simulated and observed scaling relations suggests that the physical models implemented in the simulations, including gas dynamics and feedback mechanisms, capture the key processes driving X-ray luminosity and gas content in clusters. We also studied the differences in the L_X - M_{200} scaling relation depending on the dynamical state of galaxy clusters at different apertures. First, we measure the emitted luminosity and mass inside R_{500}, showing that relaxed clusters show slightly higher luminosity at a given cluster mass compared to disturbed clusters. However, this difference is greater when we measure the X-ray emission and mass in larger apertures such as R_{200}.

The findings presented in this thesis contribute to the understanding of how the dynamical state of galaxy clusters influences the evolution of galaxies within them. The differences observed in the physical properties of galaxy populations bound to relaxed and disturbed clusters, such as colour, star-formation activity, gas availability, and scaling relations, suggest that the processes occurring during cluster mergers play a critical role in shaping the properties of galaxies and their environments.

Future Prospectives

Based on the results of this thesis, there are still many open questions to dive deeper into the understanding of the influence of the dynamical state on the global properties of galaxy clusters and their satellite populations. One unaddressed topic relates to galaxy quenching in post-merging clusters. In chapter 3 of this thesis, we found that disturbed halos with redshift between $0.55 \leq z < 1$ have a higher fraction of blue galaxies than relaxed galaxy clusters. Following this, in chapter 4, we show that the Illustris TNG100 simulation is able to reproduce this excess of blue galaxies in disturbed clusters compared to relaxed ones. We also show that galaxies bound to pre-merger clusters suffer an enhancement in star formation activity. However, the SFR rate decreases rapidly when the structure relaxes, implying a fast quenching of their satellite galaxies.

To characterise the physical process driving these differences, it is necessary to quantify the individual contribution of each physical mechanism. These mechanisms include disc instability, gas stripping, strangulation, harassment, and depletion of the gas reservoir. This project will be based on cosmological simulations and its results will reveal the physical reasons for the excess of blue galaxies observed in disturbed clusters and also will provide an understanding of the physical processes driving the galaxy evolution in galaxy clusters. Given its large volume, the most appropriate simulation for carrying out this project is the Millenium TNG simulation, where we can detect around 1500 galaxy clusters with masses $M_{500} > 10^{14}\ M_{\odot}$, also having enough mass resolution to resolve intermediate and massive satellite galaxies. Millenium TNG is a new and powerful tool that was previously unavailable, enabling the study of galaxy clusters in more extreme environments.

The generated emission map mocks in X-rays also open new unexplored questions, for example, the study of the projection effects on dynamical studies of clusters. X-rays have been established as one of the best wavelengths to study galaxy clusters given that the emission depends on the square of the density, reducing the susceptibility to line-of-sight projection effects (Ramos-Ceja et al., 2019). In this sense, these projection effects can introduce deviations of up to 20% in estimated luminosity (Zuhone et al., 2023). However, the influence of projection effects is expected to be more pronounced when estimating the parameters employed for quantifying the dynamic state of galaxy clusters. The parameters used to classify them are based on their morphology, which is significantly influenced by the presence of foreground and background structures. These parameters include concentration index, centroid shift, and power ratio. More importantly, misclassification between relaxed and disturbed clusters can introduce biases in the estimation of galaxy cluster physical properties. A merging halo may falsely exhibit characteristics of a relaxed cluster if the merger axis aligns with the line of sight, hiding the presence of a secondary structure behind the primary halo. Also, a relaxed halo could be erroneously classified as disturbed if there exists a foreground or background structure that introduces contamination in the generated mock dataset. In this sense, it will be necessary to develop a methodology for quantifying the deviation in dynamical parameters resulting from projection effects when compared with the 3D equivalent parameter derived directly from the simulation's output. A great result of this project could be the identification of the most suitable parameter or combination of parameters to describe the dynamic state of galaxy clusters in a manner that minimises the impact of projection effects. The results of this project can play a fundamental role in comprehending the systematic errors introduced by projection in the current and forthcoming X-ray galaxy cluster surveys, including eROSITA. This survey will soon release data of unprecedented quality, which calls for advances in modelling and understanding the possible systematic bias affecting the observations.

Another interesting topic to explore using cosmological simulations is the scaling relations beyond relaxed clusters. X-ray observations of the (ICM) yield maps that offer insights into the spatial distribution of the cluster gas density, temperature, and metallicities. Connecting X-ray observations to cluster physical properties usually relies on the assumption of hydrostatic equilibrium and spherical symmetry. However, clusters undergoing merging process are expected to produce collisionless shocks, resulting in gas heating that induce non-equilibrium effects. Those effects can modify the X-ray emission and breaking the spherical symmetry, which are the basic assumptions for the estimation of observables from galaxy cluster emission maps (Sarazin, 2001). As a consequence of these assumptions, the mass derived using the X-ray emission tends to be systematically underestimated by around 20%for galaxy clusters. In particular, the error and the associated uncertainties are more pronounced for disturbed clusters compared to their relaxed counterparts (Pop et al., 2022; Biffi et al., 2016). Therefore, it is necessary to introduce a correction for X-ray emission that accounts for the non-equilibrium effects occurring during cluster mergers. Additionally, it is also necessary to relax the spherical-symmetry assumption by incorporating an angular dependence to the thermodynamic profiles. This project has great potential to impact the method of estimating the physical properties of galaxy clusters with X-ray observations.

Bibliography

Aarseth S. J., Turner E. L., Gott J. R. I., 1979, ApJ, 228, 664

Abbott T. M. C., et al., 2021, ApJS, 255, 20

Abell G. O., 1958, ApJS, 3, 211

Abell G. O., Corwin Harold G. J., Olowin R. P., 1989, ApJS, 70, 1

Alam S., et al., 2015, ApJS, 219, 12

Albrecht A., Steinhardt P. J., 1982, Physical Review Letters, 48, 1220

Aldás F., Zenteno A., Gómez F. A., Hernandez-Lang D., Carrasco E. R., Vega-Martínez C. A., Nilo Castellón J. L., 2023, MNRAS, 525, 1769

Aldás F., Gómez F. A., Vega-Martínez C., 2024, in press

Allen S. W., Evrard A. E., Mantz A. B., 2011, ARA&A, 49, 409

Alpher R., Herman R., 1948, Nature, 162, 774

Alpher R. A., Bethe H., Gamow G., 1948, Physical Review, 73, 803

Anders E., Grevesse N., 1989, GCACAK, 53, 197

Andrade-Santos F., et al., 2017, ApJ, 843, 76

Arendt A. R., Perrott Y. C., Contreras-Santos A., de Andres D., Cui W., Rennehan D., 2024, Monthly Notices of the Royal Astronomical Society, 530, 20

Arnaud M., Pointecouteau E., Pratt G. W., 2005, A&A, 441, 893

Artale M. C., et al., 2017, MNRAS, 470, 1771

Ayromlou M., Nelson D., Yates R. M., Kauffmann G., White S. D. M., 2019, MNRAS, 487, 4313

Bagla J. S., 2002, JA&A, 23, 185

Bahé Y. M., McCarthy I. G., Balogh M. L., Font A. S., 2013, MNRAS, 430, 3017

Bahé Y. M., et al., 2019, MNRAS, 485, 2287

Baldry I. K., Glazebrook K., Brinkmann J., Ivezić , Lupton R. H., Nichol R. C., Szalay A. S., 2004, ApJ, 600, 681

Ball W. H., Beeck B., Cameron R. H., Gizon L., 2016, A&A, 592

Balogh M. L., Morris S. L., 2000, MNRAS, 318, 703

Barnes J., Hut P., 1986, Nat, 324, 446

Barnes D. J., Kay S. T., Henson M. A., McCarthy I. G., Schaye J., Jenkins A., 2017, MNRAS, 465, 213

Barnes D. J., Vogelsberger M., Pearce F. A., Pop A. R., Kannan R., Cao K., Kay S. T., Hernquist L., 2021, MNRAS, 506, 2533

Battaglia N., Bond J. R., Pfrommer C., Sievers J. L., 2012, ApJ, 758, 74

Bauer F. E., Fabian A. C., Sanders J. S., Allen S. W., Johnstone R. M., 2005, MNRAS, 359, 1481

Bertin E., 2011, Analysis, 442, 435

Bertin E., Arnouts S., 1996, A&AS, 117, 393

Bertschinger E., 1985, ApJS, 58, 39

Bett P., Eke V., Frenk C. S., Jenkins A., Helly J., Navarro J., 2007, MNRAS, 376, 215

Biffi V., et al., 2016, ApJ, 827, 112

Binggeli B., Sandage A., Tammann G. A., 1988, ARA&A, 26, 509

Binney J., Tremaine S., 2008,] 10.1515/9781400828722

Blanton M. R., Moustakas J., 2009, ARA&A, 47, 159

Bleem L. E., et al., 2015, ApJS, 216

Bleem L. E., et al., 2020, ApJS, 247, 25

Blumenthal G. R., Faber S. M., Primack J. R., Rees M. J., 1984, Nat, 311, 517

Böhringer H., Werner N., 2010, The Astronomy and Astrophysics Review, 18, 127

Böhringer H., Dolag K., Chon G., 2012, A&A, 539

Borgani S., et al., 2004, X-ray properties of galaxy clusters and groups from a cosmological hydrodynamical simulation, doi:10.1111/j.1365-2966.2004.07431.x

Bose S., et al., 2023, MNRAS, 524, 2579

Boselli A., Gavazzi G., 2006, PASP, 118, 517

Boselli A., Cortese L., Boquien M., Boissier S., Catinella B., Gavazzi G., Lagos C., Saintonge A., 2014, A&A, 564

Bouchet F. R., Hernquist L., 1988, ApJS, 68, 521

Bower R. G., Lucey J. R., Ellis R. S., 1992, MNRAS, 254, 601

Brickhouse N. S., Desai P., Hoogerwerf R., Liedahl D. A., Smith R. K., 2005, AIP Conference Proceedings, pp 405–407

Brodwin M., et al., 2013, ApJ, 779

Brun A. M., McCarthy I. G., Schaye J., Ponman T. J., 2017, MNRAS, 466, 4442

Brunetti G., Venturi T., Dallacasa D., Cassano R., Dolag K., Giacintucci S., Setti G., 2007, ApJ, 670, L5

Brunetti G., et al., 2008, Nature, 455, 944

Brunetti G., Cassano R., Dolag K., Setti G., 2009, A&A, 507, 661

Bruzual G., Charlot S., 2003, MNRAS, 344, 1000

Buote D. A., Tsai J. C., 1995, ApJ, 452, 522

Burns J. O., Hallman E. J., Gantner B., Motl P. M., Norman M. L., 2008, ApJ, 675, 1125

Butcher H., Oemler A. J., 1984, ApJ, 285, 426

Caldwell N., Rose J. A., 1997, AJ, 113, 492

Campitiello M. G., et al., 2022, A&A, 665

Carlstrom J. E., Holder G. P., Reese E. D., 2002, ARA&A, 40, 643

Cassano R., Brunetti G., Röttgering H. J., Brüggen M., 2010, A&A, 509

Cavaliere A. G., Gursky H., Tucker W. H., 1971, Nat, 231, 437

Chabrier G., 2003, PASP, 115, 763

Cohen S. A., Hickox R. C., Wegner G. A., 2015, ApJ, 806

Cole S., Lacey C. G., Baugh C. M., Frenk C. S., 2000, MNRAS, 319, 168

Connor T., Kelson D. D., Donahue M., Moustakas J., 2019, ApJ, 875, 16

Conroy C., 2013, ARA&A, 51, 393

Contreras-Santos A., et al., 2022, MNRAS, 511, 2897

Covey K. R., et al., 2007, AJ, 134, 2398

Cui W., Power C., Borgani S., Knebe A., Lewis G. F., Murante G., Poole G. B., 2017, MNRAS, 464, 2502

DES-Collaboration et al., 2021, ApJS, 255, 20

De Luca F., De Petris M., Yepes G., Cui W., Knebe A., Rasia E., 2021, MNRAS, 504, 5383

De Lucia G., et al., 2007, MNRAS, 374, 809

De Propris R., Bremer M. N., Phillipps S., 2016, MNRAS

Delgado A. M., et al., 2023, MNRAS, 523, 5899

Desai S., et al., 2012, ApJ, 757, 83

Dicke R. H., 1946, Review of Scientific Instruments, 17, 268

Dicke R. H., Peebles P. J. E., Roll P. G., Wilkinson D. T., 1965, ApJ, 142, 414

Diemer B., et al., 2019, MNRAS, 487, 1529

Dolag K., Borgani S., Murante G., Springel V., 2009, MNRAS, 399, 497

Donnari M., et al., 2019, MNRAS, 485, 4817

Donnari M., et al., 2020, MNRAS, 500, 4004

Donnari M., Pillepich A., Nelson D., Marinacci F., Vogelsberger M., Hernquist L., 2021, MNRAS, 506, 4760

Dressler A., 1980, ApJ, 236, 351

Dressler A., Shectman S. A., 1988, ApJ, 95, 985

Drlica-Wagner A., et al., 2021, ApJS, 256, 2

Duffy A. R., Schaye J., Kay S. T., Vecchia C. D., 2008, MNRAS: Letters, 390, 64

Eckmiller H. J., Hudson D. S., Reiprich T. H., 2011, A&A, 535

Ettori S., Tozzi P., Borgani S., Rosati P., 2004, A&A, 417, 13

Evans D. W., et al., 2018, A&A, 616

Evrard A. E., 1988, MNRAS, 235, 911

Fabian A. C., 1994, ARA&A, 32, 277

Feretti L., Giovannini G., Govoni F., Murgia M., 2012, A&AR, 20, 54

Ferrari C., Maurogordato S., Cappi A., Benoist C., 2003, A&A, 399, 813

Fields B. D., 2011, Annual Review of Nuclear and Particle Science, 61, 47

Fixsen D. J., 2009, Astrophysical Journal, 707, 916

Flaugher B., et al., 2015, AJ, 150

Forman W., Kellogg E., Gursky H., Tananbaum H., Giacconi R., 1972, ApJ, 178, 309

Fortuna M. C., et al., 2021, A&A, 654

Fossati M., et al., 2017, ApJ, 835, 153

Freedman W. L., et al., 2001, ApJ, 553, 47

Fujita Y., Nagashima M., 1999, ApJ, 516, 619

Gamow G., 1948, Nature, 162, 680

Garling C. T., Peter A. H., Spekkens K., Sand D. J., Hargis J., Crnojević D., Carlin J. L., 2024, MNRAS, 528, 365

Gaspari M., Churazov E., Nagai D., Lau E. T., Zhuravleva I., 2014, A&A, 569

Gene S., et al., 2014, MNRAS, 445, 175

George K., Vassallo T., Mohr J., Mirkazemi M., Israel H., De Jong J. T. A., Kleijn G. A. V., 2020, 527

Gilfanov M. R., Syunyaev R. A., Churazov E. M., 1987, Soviet Astronomy Letters, 13

Gingold R. A., Monaghan J. J., 1977, MNRAS, 181, 375

Gladders M. D., Yee H. K. C., 2000, AJ, 120, 2148

Gladders M. D., Yee H. K. C., 2005, ApJS, 157, 1

Gladders M. D., Yee H. K. C., Majumdar S., Barrientos L. F., Hoekstra H., Hall P. B., Infante L., 2007, ApJ, 655, 128

Gnedin O. Y., 2003, ApJ, 582, 141

Guglielmo V., et al., 2019, A&A, 625, A112

Gunn J. E., Gott J. Richard I., 1972, ApJ, 176, 1

Guo Q., White S., Li C., Boylan-Kolchin M., 2010, MNRAS, 404, 1111

Guo Q., et al., 2011, MNRAS, 413, 101

Guth A. H., 1981, Physical Review D, 23, 347

H. Neilsen, Jr. Bernstein G., Gruendl R., Kent S., 2016,] 10.2172/1250877

Haggar R., Gray M. E., Pearce F. R., Knebe A., Cui W., Mostoghiu R., Yepes G., 2020, MNRAS, 492, 6074

Haggerty M. J., Janin G., 1974, 36, 415

Hennig C., et al., 2017, MNRAS, 467, 4015

Hernández-Aguayo C., et al., 2023, MNRAS, 524, 2556

Hernquist L., 1987, ApJS, 64, 715

Hicks A. K., et al., 2008, ApJ, 680, 1022

High F. W., Stubbs C. W., Rest A., Stalder B., Challis P., 2009, AJ, 138, 110

Hilton M., et al., 2009, ApJ, 697, 436

Hou A., et al., 2012, MNRAS, 421, 3594

Hubble E., 1929, Proceedings of the National Academy of Sciences, 15, 168

Hubble E. P., 1936, Yale University Press

Hubble E., Humason M. L., 1931, ApJ, 74, 43

Iovino A., et al., 2010, A&A, 509

Ivezić , et al., 2007, AJ, 134, 973

Jaffé Y. L., Aragón-Salamanca A., De Lucia G., Jablonka P., Rudnick G., Saglia R., Zaritsky D., 2011, MNRAS, 410, 280

Jian H. Y., et al., 2018, PASJ, 70

Jung S. L., Choi H., Wong O. I., Kimm T., Chung A., Yi S. K., 2018, ApJ, 865, 156

Kaiser N., 1986, MNRAS, 222, 323

Kannan R., et al., 2023, MNRAS, 524, 2594

Klein M., et al., 2018, MNRAS, 474, 3324

Klein M., et al., 2019, MNRAS, 488, 739

Kleiner D., Pimbblet K. A., Owers M. S., Jones D. H., Stephenson A. P., 2014, MNRAS, 439, 2755

Klypin A. A., Shandarin S. F., 1983, MNRAS, 204, 891

Kodama T., Arimoto N., 1996, A&A, 320, 41

Kolokotronis V., Basilakos S., Plionis M., Georgantopoulos I., 2001, MNRAS, 320, 49

Komatsu E., et al., 2011, ApJS, 192, 18

Kravtsov A. V., Borgani S., 2012, ARA&A, 50, 353

Kravtsov A. V., Vikhlinin A., Nagai D., 2006, ApJ, 650, 128

Kron R. G., 1980, ApJS, 43, 305

Kunz M. W., Schekochihin A. A., Cowley S. C., Binney J. J., Sanders J. S., 2011, MNRAS, 410, 2446

Lin H. W., et al., 2014, AJ, 147

Lindblad P. O., 1960, Stockholms Observatoriums Annaler

Linde A., 1982, Physics Letters B, 108, 389

Łokas E. L., 2020, A&A, 638

Łokas E. L., Mamon G. A., 2003, MNRAS, 343, 401

Lopes P. A. A., Ribeiro A. L. B., Brambila D., 2023, Monthly Notices of the Royal Astronomical Society: Letters, 527, L19

Lovisari L., Reiprich T. H., Schellenberger G., 2015, A&A, 573

Lovisari L., et al., 2020, ApJ, 892, 102

Lucy L. B., 1977, AJ, 82, 1013

Maier C., Hayashi M., Ziegler B. L., Kodama T., 2019, A&A, 626, A14

Maier C., Haines C. P., Ziegler B. L., 2022, A&A, 658, A190

Mancone C. L., Gonzalez A. H., Brodwin M., Stanford S. A., Eisenhardt P. R. M., Stern D., Jones C., 2010, ApJ, 720, 284

Mann A. W., Ebeling H., 2012, MNRAS, 420, 2120

Mantz A., Allen S. W., Rapetti D., Ebeling H., 2010, MNRAS, 406, 1759

Mantz A. B., Allen S. W., Morris R. G., Schmidt R. W., 2016a, MNRAS, 456, 4020

Mantz A. B., et al., 2016b, MNRAS, 463, 3582

Marinacci F., et al., 2018, MNRAS, 480, 5113

Mastropietro C., Moore B., Mayer L., Debattista V. P., Piffaretti R., Stadel J., 2005, MNRAS, 364, 607

Maughan B. J., 2007, ApJ, 668, 772

Maughan B. J., 2013, MNRAS, 437, 1171

McCarthy I. G., et al., 2010, Monthly Notices of the Royal Astronomical Society, pp no–no

McDonald M., et al., 2012, Nat, 488, 349

McDonald M., et al., 2013, ApJ, 774

McDonald M., et al., 2019, ApJ, 870, 85

McGee S. L., Balogh M. L., Bower R. G., Font A. S., McCarthy I. G., 2009, MNRAS, 400, 937

McNamara B., Nulsen P., 2007, ARA&A, 45, 117

Mcgee S. L., Balogh M. L., Wilman D. J., Bower R. G., Mulchaey J. S., Parker L. C., Oemler A., 2011, MNRAS, 413, 996

Merloni A., et al., 2012, Technical report, eROSITA Science Book: Mapping the Structure of the Energetic Universe, doi:https://doi.org/10.48550/arXiv.1209.3114.

Mewe R., 1998, Physica Scripta, T77, 97

Mihalas D., 1967a, ApJ, 149, 169

Mihalas D., 1967b, ApJ, 150, 1168

Mitchell D. W., 2004, Math. Gaz., 88, 142

Miyoshi K., Kihara T., 1975, PASJ, 27, 333

Mo H., van den Bosch F., White S., 2010, Galaxy Formation and Evolution, pp 1–24

Mohr J. J., Fabricant D. G., Geller M. J., 1993, ApJ, 413, 492

Molnar S. M., 2016, Cluster Physics with Merging Galaxy Clusters. Vol. 2, Frontiers Media S.A.

Moore B., Lake G., Quinn T., Stadel J., 1999, MNRAS, 304, 465

Morganson E., et al., 2018, PASP, 130, 1

Munari E., Biviano A., Borgani S., Murante G., Fabjan D., 2013, MNRAS, 430, 2638

Murphy D. N., Geach J. E., Bower R. G., 2012, MNRAS, 420, 1861

Muzzin A., et al., 2012, ApJ, 746

Nagai D., 2006, ApJ, 650, 538

Nagao T., Maiolino R., Marconi A., 2006, A&A, 459, 85

Naiman J. P., et al., 2018, MNRAS, 477, 1206

Nelson D., et al., 2018, MNRAS, 475, 624

Nelson D., et al., 2019, MNRAS, 490, 3234

Neto A. F., et al., 2007, MNRAS, 381, 1450

Nurgaliev D., McDonald M., Benson B. A., Miller E. D., Stubbs C. W., Vikhlinin A., 2013, ApJ, 779

Nurgaliev D., et al., 2017, ApJ, 841, 5

Oemler A., Hale Observatories J., 1974, ApJ, 194, 1

Owers M. S., Couch W. J., Nulsen P. E. J., Randall S. W., 2012, ApJ, 750, L23

Pakmor R., Springel V., 2013, MNRAS, 432, 176

Pakmor R., et al., 2023, MNRAS, 524, 2539

Pallero D., Gómez F. A., Padilla N. D., Torres-Flores S., Demarco R., Cerulo P., Olave-Rojas D., 2019, MNRAS, pp 847–858

Pallero D., Gómez F. A., Padilla N. D., Bahé Y. M., Vega-Martínez C. A., Torres-Flores S., 2022, MNRAS, 511, 3210

Papovich C., et al., 2010, ApJ, 716, 1503

Peebles P. J. E., Yu J. T., 1970, ApJ, 162, 815

Peluso G., et al., 2022, ApJ, 927, 130

Peng C. Y., Ho L. C., Impey C. D., Rix H. W., 2010, AJ, 139, 2097

Penzias A. A., Wilson R. W., 1965, ApJ, 142, 419

Pillepich A., et al., 2018a, MNRAS, 473, 4077

Pillepich A., et al., 2018b, MNRAS, 475, 648

Pillepich A., et al., 2019, MNRAS, 490, 3196

Planck Collaboration 2016, A&A, 594, A24

Planck Collaboration 2020, A&A, 641, A6

Poggianti B. M., Barbaro G., 1997, A&A, 325, 1025

Poggianti B. M., et al., 2017, Nature, 548, 304

Poole G. B., Fardal M. A., Babul A., McCarthy I. G., Quinn T., Wadsley J., 2006, MNRAS, 373, 881

Pop A.-R., et al., 2022

Pranger F., et al., 2014, A&A, 567, C1

Pratt G. W., Croston J. H., Arnaud M., Böhringer H., 2009, A&A, 498, 361

Pratt G. W., et al., 2010, Astronomy and Astrophysics, 511, A85

Press W. H., Schechter P., 1974, ApJ, 187, 425

Ramos-Ceja M. E., Pacaud F., Reiprich T. H., Migkas K., Lovisari L., Schellenberger G., 2019, A&A, 626

Rasia E., Tormen G., Moscardini L., 2004, MNRAS, 351, 237

Reiprich T. H., Bohringer H., 2002, ApJ, 567, 716

Rhee J., Lah P., Briggs F. H., Chengalur J. N., Colless M., Willner S. P., Ashby M. L., Fèvre O. L., 2018, MNRAS, 473, 1879

Riess A. G., Casertano S., Yuan W., Macri L. M., Scolnic D., 2019, The Astrophysical Journal, 876, 85

Rindler W., 1977, Essential Relativity

Roberts I. D., Parker L. C., Brown T., Joshi G. D., Hlavacek-Larrondo J., Wadsley J., 2019, ApJ, 873, 42

Roberts I. D., et al., 2022, ApJ, 941, 77

Rodriguez-Gomez V., et al., 2019, MNRAS, 483, 4140

Rohr E., Pillepich A., Nelson D., Zinger E., Joshi G. D., Ayromlou M., 2023, MNRAS, 524, 3502

Rykoff E. S., et al., 2016, ApJS, 224, 1

Safarzadeh M., Loeb A., 2019, MNRAS: Letters, 486, L26

Santos J. S., Rosati P., Tozzi P., Böhringer H., Ettori S., Bignamini A., 2008, A&A, 483, 35

Sarazin C. L., 1986, RMP, 58, 1

Sarazin C. L., 2001, 1 edn

Sarazin C. L., 2004, JKAS, 37, 433

Saro A., Borgani S., Tornatore L., Dolag K., Murante G., Biviano A., Calura F., Charlot S., 2006, MNRAS, 373, 397

Schaye J., et al., 2015, MNRAS, 446, 521

Schechter P., 1976, ApJ, 203, 297

Schlafly E. F., Finkbeiner D. P., 2011, ApJ, 737

Schlegel D. J., Finkbeiner D. P., Davis M., 1998, ApJ, 500, 525

Searle L., Sargent W. L. W., 1972, ApJ, 173, 25

Shim H., et al., 2011, ApJ, 727

Shimizu M., Kitayama T., Sasaki S., Suto Y., 2003, ApJ, 590, 197

Short C. J., Thomas P. A., Young O. E., Pearce F. R., Jenkins A., Muanwong O., 2010, Monthly Notices of the Royal Astronomical Society, 408, 2213

Sijacki D., Springel V., Di Matteo T., Hernquist L., 2007, Monthly Notices of the Royal Astronomical Society, 380, 877

Sijacki D., Vogelsberger M., Genel S., Springel V., Torrey P., Snyder G. F., Nelson D., Hernquist L., 2015, MNRAS, 452, 575

Singh S., Mandelbaum R., More S., 2015, MNRAS, 450, 2195

Snyder G. F., et al., 2012, ApJ, 756

Soares N. R., Rembold S. B., 2019, MNRAS, 483, 4354

Sobral D., Stroe A., Dawson W. A., Wittman D., James Jee M., Röttgering H., van Weeren R. J., Brüggen M., 2015, MNRAS, 450, 630

Somerville R. S., Hopkins P. F., Cox T. J., Robertson B. E., Hernquist L., 2008, MNRAS, 391, 481

Song J., et al., 2012, ApJ, 761

Springel V., 2005, MNRAS, 364, 1105

Springel V., 2010, MNRAS, 401, 791

Springel V., Hernquist L., 2003, MNRAS, 339, 289

Springel V., White S. D., Tormen G., Kauffmann G., 2001, MNRAS, 328, 726

Springel V., et al., 2018, MNRAS, 475, 676

Stanford S. A., Eisenhardt P. R., Dickinson M., 1998, ApJ, 492, 461

Steigman G., 2007, Annual Review of Nuclear and Particle Science, 57, 463

Stott J. P., Smail I., Edge A. C., Ebeling H., Smith G. P., Kneib J., Pimbblet K. A., 2007, ApJ, 661, 95

Strazzullo V., et al., 2010, Astronomy & Astrophysics, 524, A17

Stroe A., Sobral D., 2021, ApJ, 912, 55

Stroe A., Sobral D., Röttgering H. J., van Weeren R. J., 2014, MNRAS, 438, 1377

Stroe A., Sobral D., Paulino-Afonso A., Alegre L., Calhau J., Santos S., van Weeren R., 2017, MNRAS, 465, 2916

Sunyaev R. A., Zeldovich Y. B., 1972, Comments on Astrophysics and Space Physics

Tasker E. J., Brunino R., Mitchell N. L., Michielsen D., Hopton S., Pearce F. R., Bryan G. L., Theuns T., 2008, MNRAS, 390, 1267

Torrey P., Vogelsberger M., Sijacki D., Springel V., Hernquist L., 2012, MNRAS, 427, 2224

Torrey P., et al., 2019, MNRAS, 484, 5587

Tremaine S., 1990

Troncoso-Iribarren P., Padilla N., Santander C., Lagos C. D., García-Lambas D., Rodríguez S., Contreras S., 2020, MNRAS, 497, 4145

Truong N., Pillepich A., Nelson D., Zhuravleva I., Lee W., Ayromlou M., Lehle K., 2024, A&A, 686

Visvanathan N., Sandage A., 1977, ApJ, 216, 214

Vogelsberger M., et al., 2014, MNRAS, 444, 1518

Vogelsberger M., et al., 2018, MNRAS, 474, 2073

Vogelsberger M., Marinacci F., Torrey P., Puchwein E., 2020, Nat. Rev. Phys., 2, 42

Voit G. M., 2005, RMP, 77, 207

Vulcani B., et al., 2018, ApJ Letters, 866, L25

Vulcani B., et al., 2020, ApJ, 892, 146

Wadsley J. W., Veeravalli G., Couchman H. M. P., 2008, MNRAS, 387, 427

Wang L., Tozzi P., Yu H., Gaspari M., Ettori S., 2023, A&A, 674

Weinberg S., 1972, Gravitation and Cosmology: Principles and Applications of the General Theory of Relativity

Weinberger R., et al., 2017, MNRAS, 465, 3291

Weinberger R., Springel V., Pakmor R., 2020, ApJS, 248, 32

Wetzel A. R., Tinker J. L., Conroy C., 2012, MNRAS, 424, 232

Wetzel A. R., Tinker J. L., Conroy C., van den Bosch F. C., 2013, MNRAS, 432, 336

Wetzel A. R., Tinker J. L., Conroy C., van den Bosch F. C., 2014, MNRAS, 439, 2687

White S. D. M., 1976, Monthly Notices of the Royal Astronomical Society, 177, 717

White S. D. M., Frenk C. S., 1991, ApJ, 379, 52

White S. D. M., Rees M. J., 1978, MNRAS, 183, 341

White S. D. M., Frenk C. S., Davis M., 1983, ApJ, 274, L1

Wilson G., et al., 2009, The Astrophysical Journal, 698, 1943

Worthey G., 1994, ApJS, 95, 107

Yoon Y., Im M., 2020, ApJ, 893, 117

Yoshikawa K., Yoshida N., Umemura M., 2013, ApJ, 762, 116

Younger J. D., Bryan G. L., 2007, The Astrophysical Journal, 666, 647

Yuan Z. S., Han J. L., 2020, MNRAS, 497, 5485

Yuan Z. S., Han J. L., Wen Z. L., 2022, MNRAS, 513, 3013

Zabludoff A. I., Zaritsky D., Lin H., Tucker D., Hashimoto Y., Shectman S. A., Oemler A., Kirshner R. P., 1996, ApJ, 466, 104

Zenteno A., et al., 2016, MNRAS, 462, 830

Zenteno A., et al., 2020, MNRAS, 495, 705

Zhang Y. Y., Finoguenov A., Böhringer H., Kneib J. P., Smith G. P., Kneissl R., Okabe N., Dahle H., 2008, A&A, 482, 451

Zhang Y. Y., Reiprich T. H., Finoguenov A., Hudson D. S., Sarazin C. L., 2009, ApJ, 699, 1178

Zhang C., Yu Q., Lu Y., 2016, ApJ, 820, 85

Zhang B., Cui W., Wang Y., Dave R., De Petris M., 2022, MNRAS, 516, 26

Zuhone J., et al., 2023, A&A, 675

Zwicky F., 1933, Helvetica Physica Acta

Zwicky F., 1937, ApJ, 86, 217

van Albada G. B., 1961, ApJ, 66, 590

van der Burg R. F. J., et al., 2017, Astronomy & Astrophysics, 607, A79

Acknowledgments

Quiero expresar mi más profundo agradecimiento a mi familia, quienes han sido mi pilar fundamental durante esta etapa tan importante de mi vida. A mis padres, Bolívar y Dora, por su amor incondicional, su apoyo y el ejemplo de perseverancia y esfuerzo que me han dado desde siempre; y a mi hermana Carola, por su compañía y por creer en mí en cada paso del camino.

Un agradecimiento muy especial para Patty, quien estuvo a mi lado durante todo el doctorado. Su apoyo constante y su presencia me ayudaron a superar los momentos difíciles y a disfrutar de los logros, y sin ella este proceso no habría sido el mismo.

También quiero agradecer a mis profesores guías, Facundo y Cristian, por su orientación y por compartir su conocimiento y su amitad, así como a todos los profesores del claustro del departamento de Astronomía, cuya dedicación y pasión por la enseñanza me han inspirado.

Agradezco a todos los estudiantes y el personal del Doctorado en Astronomía de la Universidad de La Serena, en especial a Gissel y Camila, que fueron mis compañeras de oficina. Su amistad y apoyo hicieron que cada día fuera más llevadero y enriquecedor.

Gracias, por estar conmigo en cada momento de este recorrido.

This thesis received support from the following scholarships: the Beca Interna from Universidad de La Serena (2020) and the Agencia Nacional de Investigación y Desarrollo (ANID)-Chile, grant number 21211648 (2021-2024). Additionally, this research was supported by the Max Planck Society through a “Partner Group” grant. Powered @NLHPC: This research was partially supported by the supercomputing infrastructure of the NLHPC (CCSS210001).